

Tracing the Farallon plate through seismic imaging with USArray

by

Robert William Porritt

A dissertation submitted in partial satisfaction of the
requirements for the degree of
Doctor of Philosophy

in

Earth and Planetary Science

in the

Graduate Division

of the

University of California, Berkeley

Committee in charge:

Professor Richard Allen, Chair
Professor Barbara Romanowicz
Professor John Rice

Spring 2013

Tracing the Farallon plate through seismic imaging with USArray

Copyright 2013
by
Robert William Porritt

Abstract

Tracing the Farallon plate through seismic imaging with USArray

by

Robert William Porritt

Doctor of Philosophy in Earth and Planetary Science

University of California, Berkeley

Professor Richard Allen, Chair

The Farallon plate system has been subducting off the western United States since at least the middle Mesozoic. This plate has undergone virtually every subduction process during this time including a long episode of flat-slab subduction, generation of microplates, and formation of oceanic plateaus. The shallow remains of this plate are two small microplates, the Gorda and Juan de Fuca, in the Pacific Northwest. The anomalous nature of these two small plates and the missing deeper evidence of subduction has motivated this study.

The USArray seismic experiment has provided unprecedented spatial sampling of the seismic wavefield in the continuous United States. Utilizing this dataset, new imaging methods have been implemented and older imaging methods have been revitalized. This study first uses ambient seismic noise in the Pacific Northwest to extract short period Rayleigh waves which are sensitive to lithospheric scale structure. Phase velocities from this model are then combined with teleseismic delay times of body waves and surface waves to image the structure of the continuous United States from the surface through the mantle transition zone. The resolving power of this model allows tracing of the Farallon plate from the trench to the lower mantle.

The seismic velocity structure of the continuous United States is broadly composed of a slow western half and fast eastern half separated by the Rocky Mountain Front. The low velocity of the western U.S. contains several high velocity anomalies. While previous work has focused on individual anomalies and suggested they represent lithospheric instabilities, a larger regional view indicates that these are the western remnants of the Farallon plate. Below the thick cratonic lithosphere of the eastern U.S., the Farallon plate contains significant topography due to a subducted heterogeneity of the oceanic plate and a viscosity contrast through the mantle transition zone. The velocity models presented herein provide a cohesive picture of Farallon subduction for the past 150 Ma.

“It’s the disagreements between friends shared over libations that pushes science forward”

For my family, friends, and teachers past and present.

Contents

List of Figures	iv
List of Tables	vi
1 Introduction	1
2 Investigation of Cascadia segmentation with ambient noise tomography	8
2.1 Introduction	8
2.2 Cascadia segmentation	9
2.3 Data and methodology	11
2.4 Noise source distribution	13
2.5 Resolution	19
2.6 Results	20
2.7 Discussion	23
2.7.1 Implications for tremor	26
2.7.2 Implications for volcanic activity	28
2.8 Summary	29
2.9 Chapter Acknowledgements	31
3 Imaging east of the Rocky Mountains with USArray: DNA13 model update and validation	32
3.1 Introduction	32
3.2 Method	33
3.3 Resolution	37
3.4 Validation	40
3.5 Results	46
3.5.1 Upper 200 km structures	46
3.5.2 Deeper structures	48
3.6 Discussion	52
3.6.1 Wyoming Province	52
3.6.2 Llano Province	53
3.6.3 Comparison of craton constituents	56
3.6.4 Deep Farallon Structure	56
3.7 Summary	57

3.8	Chapter Acknowledgements	57
4	Seismic evidence of remnant slabs beneath the western U.S.	60
4.1	Introduction	60
4.2	Results	61
4.3	Discussion	64
4.4	Conclusions	70
4.5	Chapter Acknowledgements	71
5	Conclusions	72

List of Figures

1.1	Earthquake occurrence maps	2
1.2	Global model images of Farallon plate	3
1.3	Pre-USArray Subduction Cartoon	4
1.4	Map of USArray-Transportable Array	5
2.1	Pacific Northwest tectonic and station location map.	10
2.2	Average phase velocity curve from several 1D models	14
2.3	Pacific Northwest phase velocity maps	15
2.4	Crustal thickness of Pacific Northwest	16
2.5	Seasonal noise source distribution	18
2.6	PNW10-S checkerboard test	20
2.7	PNW10-S spatial resolution	21
2.8	PNW10-S starting model recovery	22
2.9	Shallow Cascades structure	24
2.10	PNW10-S Cross section across Gorda slab	25
2.11	PNW10-S forearc fence diagram	27
2.12	PNW10-S arc fence diagram	30
3.1	Physiographic map of the contiguous US	34
3.2	Illustration of P-SV-SH rotation	36
3.3	DNA13 station and event coverage maps	38
3.4	Mean phase velocity curve and weighting function	39
3.5	DNA13 ambient noise resolution	41
3.6	DNA13 body-wave resolution	42
3.7	DNA13 SV-Joint resolution	43
3.8	DNA13 Resolution East-West cross-sections	44
3.9	DNA13 Resolution North-South cross-sections	45
3.10	DNA13 model validation test	47
3.11	DNA13 upper 200 km	49
3.12	DNA13 deeper structure	50
3.13	DNA13 comparison to larger regional/global models	51
3.14	Structure of the Wyoming Province	54
3.15	Structure of the Llano Province	55
3.16	DNA13 Deep Farallon plate structure	58

4.1	DNA13-P Farallon plane	62
4.2	DNA13-P Survey figures	63
4.3	Lithospheric instability source regions	65
4.4	Topography and crustal thickness profiles	67
4.5	Western U.S. shear wave splitting	68
4.6	Scenarios of creating remnant slabs	70
5.1	Interpretation of Pacific Northwest subduction	73
5.2	Interpretation of deep Farallon structure	74
5.3	Interpretation of remnant slabs in the western U.S.	76

List of Tables

2.1 Ambient noise selection criteria	17
--	----

Acknowledgments

I want to start with a special thank you to my advisor, Richard Allen. Richard and I have been working together for the past 7 years in the lab, the field, and various pubs. Richard has spurred me to grow as a scientist by constantly challenging me with new questions and has provided opportunities for me to travel abroad to collaborate in field and lab work. I look forward to continuing to work together as I forge my young academic career.

I first came to Berkeley as an intern through the IRIS Education and Outreach program. Little did I expect it would soon become my home for six great years. That summer was the first time I really worked independently and applied my fledgling earth science education to a real scientific question. This opportunity also awakened in me the joy of crafting computer programs to extract information from raw data. After finishing my undergraduate education at Michigan Technological University, I was excited to be able to continue working with Richard Allen at Berkeley to pursue my PhD. Within a few years of starting here at Berkeley, I had the opportunity to take over as the IRIS Internship Alumni Mentor. I'm grateful to Michael Hubenthal, John Taber, and Andy Frassetto at IRIS for providing me with the chance to share my love of seismology and programming with future seismologists.

My family has been very supportive through this entire endeavor. It has been a real challenge being separated from my parents in Michigan and my brother in Georgia, but they helped me grow to be an independent person and that strength has sustained me through the years. I look forward to the day I can return home and take my parents out to a weekly Sunday brunch.

I want to thank the faculty here at Berkeley for the outstanding high quality and challenging classes provided here. Taking and sometimes teaching these classes taught me not just specific material, but also gave me a glimpse of how much I still need to learn. Additionally, the full schedule of seminars has given me insights to areas of research I may never have considered before and opportunities to chat with a wide variety of young and old researchers from across the earth sciences. I would also like to thank the BSL and EPS staff who have helped me overcome several challenges in both research and academics.

None of this would be possible without the help and support of a troop of students, visitors, and postdocs here at Berkeley. So a big thank you to: Ved, Sanne, Aurelie, Mei, Mathias, Amanda, Holly, Cheng, Leif, Shan, Max, Qingkai, William, Mong-Han, Scott, Allen, Pascal, Caroline, Jenny, and Liang.

I would like to thank my undergraduate institution, Michigan Technological University, for providing me with an excellent fundamental education and an introduction to research. The general engineering programs provided me with a feel for basic programming and sci-

entific visualization. The Research Scholar's Program encouraged me to seek experience with research which led me to work on volcanology with Bill Rose and later hydrogeophysics with John Gierke and the Aqua Terra Tech enterprise. Small classes (down to the size of 1 student) with Wayne Pennington encouraged me to apply for the fateful IRIS Internship which has led me to this dissertation.

Finally, I want to thank the seismology community at large. At meetings sponsored by such organizations as AGU, SSA, and GSA I've interacted with researchers from across the globe and many ideas have been spurred through these interactions. I've also gained valuable experience as a field seismologist working with Alan Levander in Morocco and Joann Stock and John Hole in southern California. The staff at the IRIS PASSCAL Instrument Center have been amazingly helpful for all concerns of data and field work: thank you Eliana, Pnina, Mouse, Derry, and Lloyd.

Chapter 1

Introduction

Since the plate tectonic revolution, seismology has become the primary tool for directly determining the configuration and structure of the Earth's plates. The plate boundaries are often well defined by the occurrence of earthquakes (Fig. 1.1) and the internal earth structure is illuminated by the propagation of seismic waves. Until recently, most seismic arrays for plate tectonic questions have been generally limited in extent to investigate anomalous structures or regions of high seismic activity. Global arrays such as GEOSCOPE [Romanowicz et al., 1984] and the IRIS GSN [Lay et al., 2002] provide a broad distribution of high-quality stations and have proven useful for the computation of global-scale seismic velocity models [Kustowski et al., 2008; Lebedev and Van Der Hilst, 2008; Lekic et al., 2012; Li et al., 2008; Panning and Romanowicz, 2006; Simmons et al., 2010]. These models have produced a broad view of the upper mantle consisting primarily of subducting oceanic plates and the roots of thick cratonic lithosphere.

Images from global seismic models have shown a high velocity body under the continuous United States. This body, illustrated in figure 1.2 at 800 km depth, is generally thought to be the Farallon plate [Humphreys et al., 2003], which began subduction off the western U.S. over 150 million years ago. Since the Farallon ridge subducted at ~ 30 Ma the Mendocino Triple Junction has been migrating northward and the last remnants of the Farallon plate are now evidenced off the coast of Oregon and Washington as the Juan de Fuca/Gorda plate system [Atwater and Stock, 1998]. This subduction zone has been seismically quiet for the modern record, but paleoseismic evidence shows it has the capability to produce M9+ earthquakes [Goldfinger et al., 2012]. However the linkage between the Juan de Fuca observed near the surface and Farallon plate within the mantle has proven elusive to seismic imaging and thus the view of the western US mantle has been unclear (Fig. 1.3). Defining this connection, if it exists, is among the most fundamental goals of the Earthscope USArray (Fig. 1.4).

Geodynamic models suggest the flat slab subduction of the Farallon plate has been a primary control on the deformation of the western U.S. [Humphreys et al., 2003; Humphreys and Coblenz, 2007; Schellart et al., 2010]. However, the western U.S. mosaic contains evidence of other significant processes including the 17 Ma Columbia River Basalt large igneous province,

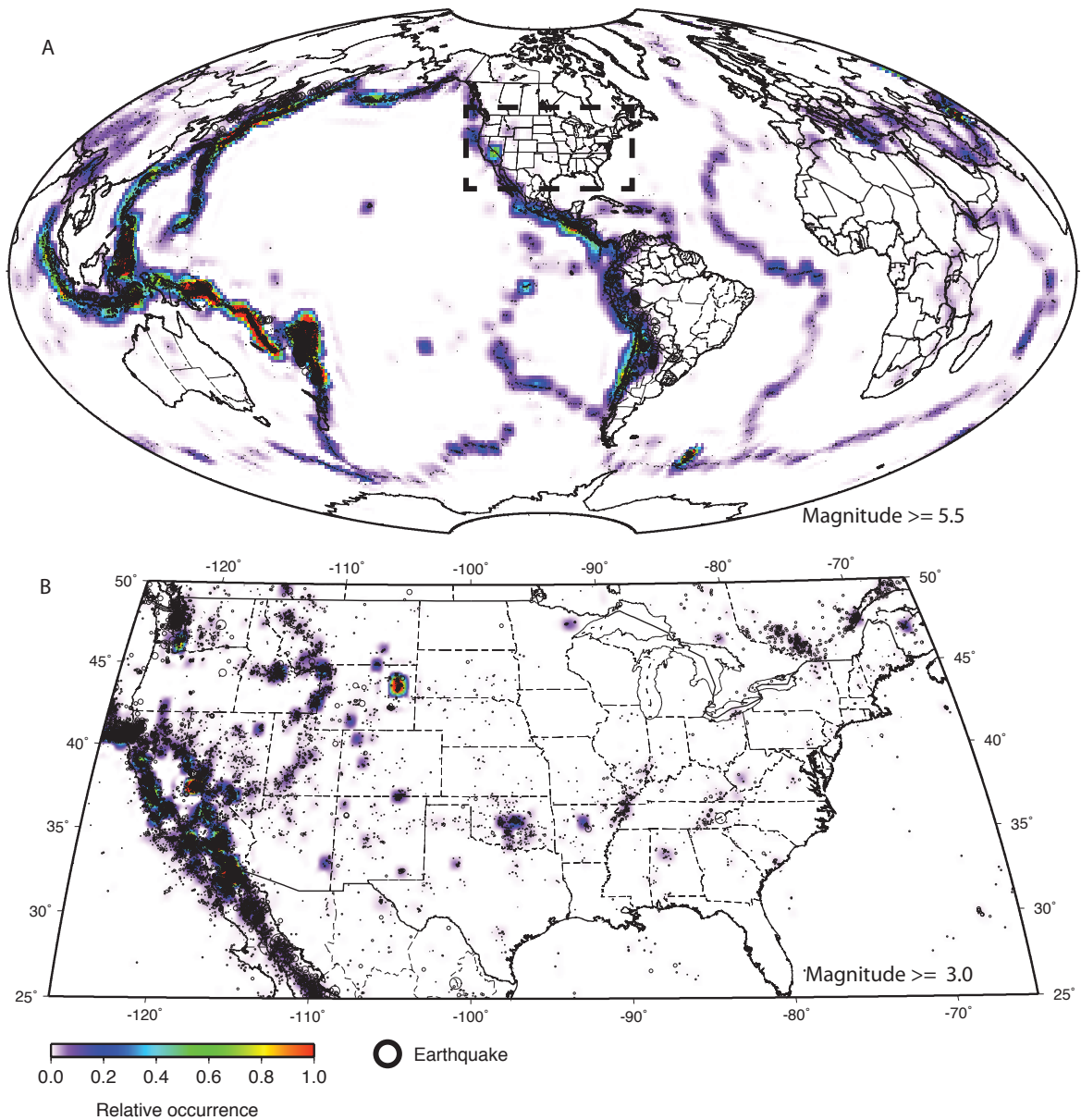


Figure 1.1: (A) Global earthquake distribution of magnitude ≥ 5.5 since 1971. Black dots indicate individual dots and color background gives relative occurrence. (B) Continuous United States seismicity map. Circles are for earthquakes magnitude ≥ 3.0 and color scale is same as A.

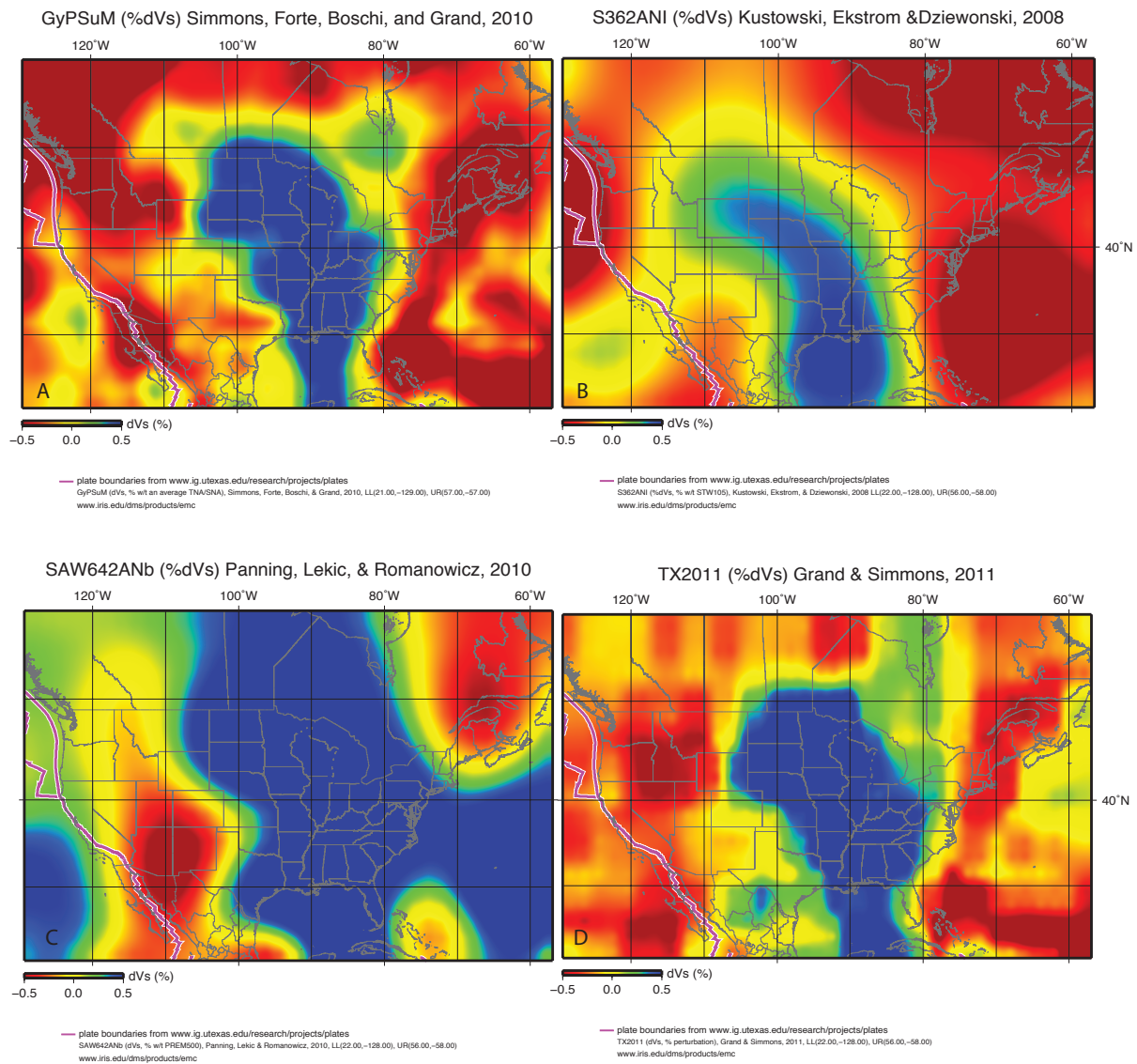


Figure 1.2: Horizontal slices at 800km depth of (A) GyPSuM [Simmons et al., 2010] (B) S362ANI [Kustowski et al., 2008] (C) SAW642b [Panning et al., 2010] and (D) TX2011 [Trabant et al., 2012] plotted from the IRIS Earth Model Collaboration page [Trabant et al., 2012].

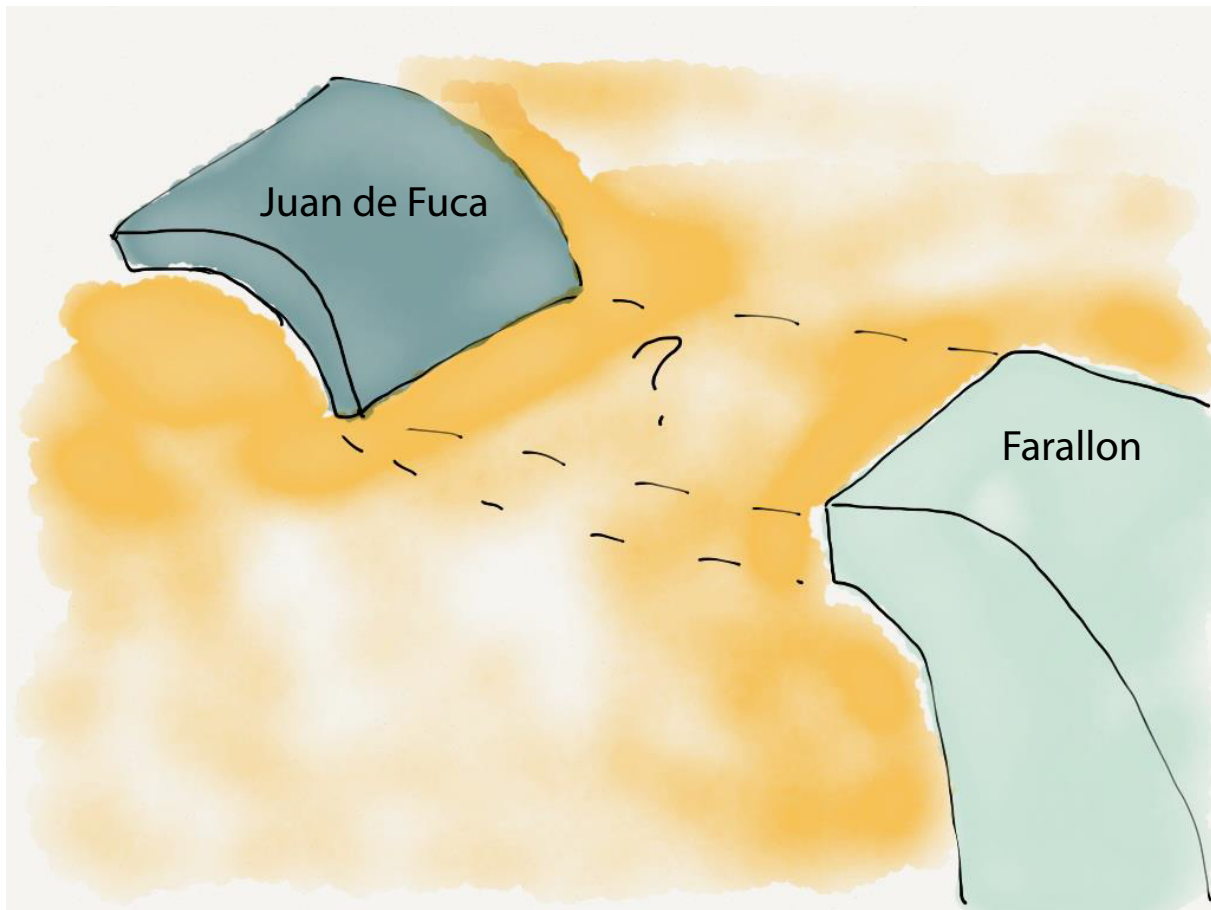


Figure 1.3: Cartoon of subduction structure under the continuous United States before detailed seismic imaging facilitated by USArray. Red represents the background warm western U.S. mantle, blues depict the Farallon and Juan de Fuca plates, and the dashed volume with a question mark indicates region of suspected, but un-imaged, slab.

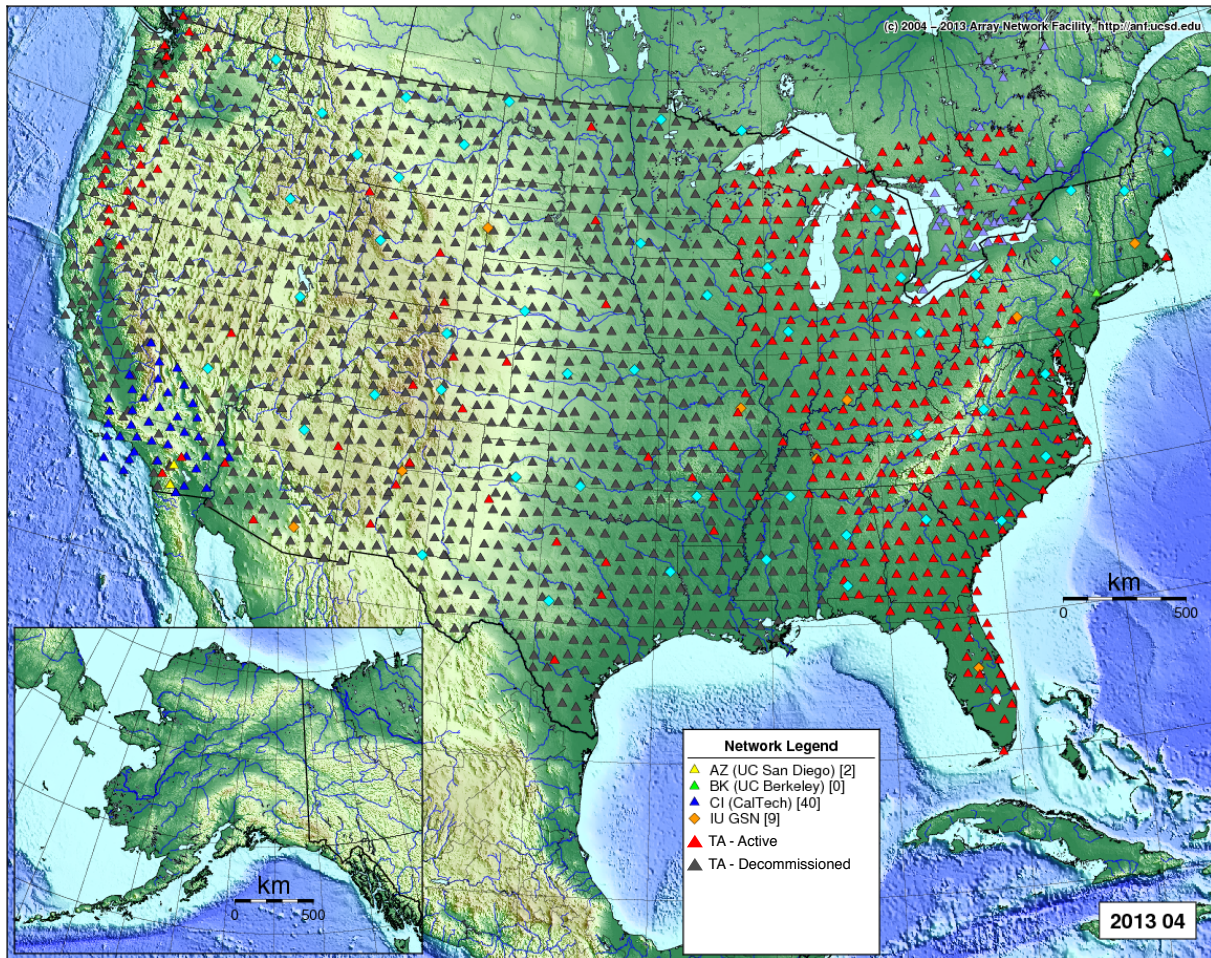


Figure 1.4: Cumulative state of the USArray-Transportable Array at time of writing (modified from the Array Network Facility).

the Yellowstone and Newberry hotspot tracks, uplift of the Sierra Nevada mountains, and extension of the Basin and Range province. Early USArray based studies have investigated many of these features and have argued whether these features have a lithospheric origin, a subduction origin, or a deep mantle origin, but many of the arguments remain inconclusive. East of the Rocky Mountain Front, the North American Laurentia Craton is composed of proterozoic blocks including the Wyoming Craton, Medicine Hat Block, and Llano Uplift [Whitmeyer and Karlstrom, 2007]. While these features offer tantalizing clues into the formation and stability of the cratons, previous studies, such as Yuan and Dueker [2005], have utilized high-density linear arrays which are unable to fully define the three-dimensional structure of the craton and underlying slab.

In this dissertation, I utilize USArray seismic data and novel imaging methods to analyze the last vestiges of the Farallon plate under North America. The 70 km station spacing of the Transportable Array and tighter spacing achieved with Flexible Arrays and regional networks provides far greater two-dimensional spatial sampling than has previously been achieved. This network combines the high resolution of small regional networks with a far greater aperture than has ever been proposed. This array, combined with rapid advancements in computational infrastructure, has allowed the implementation of new imaging techniques such as ambient noise tomography [Lin et al., 2008; Moschetti et al., 2007; Porritt et al., 2011; Yang et al., 2008], non-planar wave surface wave tomography [Pollitz and Snoke, 2010; Pollitz, 2008], teleseismic body wave tomography with multiple phases [Burdick et al., 2012; James et al., 2011; Obrebski et al., 2011, 2010; Schmandt and Humphreys, 2011; Sigloch, 2011], common conversion point stacking of receiver functions [Frassetto et al., 2011; Kumar et al., 2012; Levander and Miller, 2012], and various flavors of joint inversions of body-waves, surface-waves, and receiver functions [Bailey et al., 2012; Liu et al., 2012; Obrebski et al., 2011]. All of these methods have their own strengths and weaknesses and thus the best method to use is dependent on the target being analyzed and the data available. For the goal of imaging the slab, from the shallow Juan de Fuca to the deep eastern U.S., I use a combination of ambient seismic noise, teleseismic surface waves, and teleseismic body waves. Ambient noise alone is sufficient to image the shallow portion of the slab and a joint inversion of SV-component body waves and Rayleigh wave phase velocities provides the best images of the sub-cratonic slab currently available.

This dissertation broadly contains three main components. In the first section I present the PNW10-S model and use it to investigate the lithospheric structure associated with segmentation of the Juan de Fuca - Gorda slab. In the next section, I redefine the coordinate system used in teleseismic body wave imaging to determine relative arrival times of compressional waves (P), horizontally polarized shear waves (SH), and vertically polarized shear waves (SV). This rotation allows the joint inversion of Rayleigh wave phase velocities, which are sensitive to vertically polarized shear velocity, with the SV body-wave component. With this model, DNA13, I present a novel model validation method which addresses the predic-

tive power of the velocity model and investigate the structure of two paleozoic provinces and the eastern Farallon plate in the upper mantle. Finally, I investigate several high velocity anomalies of the western U.S. and assess the relative merits of arguing whether they represent lithospheric instabilities or remnants of the subducting Farallon plate. Through this process, I image the current state of the Farallon plate, assess the locations of missing slab, and propose a self-consistent history where the slab is able to break up and founder during its dying stages of subduction.

Chapter 2

Investigation of Cascadia segmentation with ambient noise tomography

Advisor: Richard M. Allen

Coauthors: Michael Brudzinski and Devin Boyarko

2.1 Introduction

The Cascadia Subduction Zone is where the last remnants of the Farallon Plate continue to subduct below continental North America [van der Lee and Nolet, 1997]. The southern terminus of the trench is the Mendocino Triple Junction, offshore northern California, and the northern terminus is the Queen Charlotte Triple Junction to the northwest of Vancouver Island (Figure 2.1). The Juan de Fuca plate is small in a global context, but the length of the subduction zone is sufficient to generate magnitude 9 earthquakes [Goldfinger et al., 2012]. The subduction zone is atypical for a variety of reasons. It has a distinct paucity of seismicity, with no earthquakes greater than 75 km depth, and almost no sub-crustal earthquakes beneath Oregon. The trench is undergoing rollback and clockwise rotation as the Basin and Range expands to the southeast [Humphreys and Coblenz, 2007]. Finally, the subduction zone exhibits anisotropic fast directions normal to the trench as observed from shear wave splitting [Currie et al., 2004; Eakin et al., 2010], whereas the vast majority of subduction zones have trench-parallel fast directions [Long and Silver, 2008].

In this chapter we employ ambient noise tomography to image the lithospheric structure of the Cascadia Subduction Zone from southern Vancouver Island to California. Ambient seismic noise tomography has been used to study several regions including the western United States [Moschetti et al., 2007], the eastern United States [Liang and Langston, 2008], Taiwan [Huang et al., 2010; You et al., 2010], Costa Rica [Harmon et al., 2008], Norway [Köhler et al., 2011], Australia [Saygin and Kennett, 2010], and Europe [Yang et al., 2007]. Ambient noise is particularly useful in seismically quiescent areas because recovery is primarily influenced by receiver array geometry and not the distribution of earthquakes. We make

use of seismic stations from the Earthscope Transportable Array, regional seismic networks, and two Earthscope Flexible Array deployments resulting in an array covering most of the United States with greatly increased density in Cascadia (Figure 2.1). The measurements typically derived from ambient noise are fundamental mode Rayleigh wave phase velocities between 7 and 40 seconds period. These measurements have peak sensitivity between the surface and roughly 50 km depth and thus this method provides excellent sampling of the crust. In order to investigate the structure throughout and immediately below the lithosphere, we use measurements from noise cross-correlations to periods of 90 seconds. This requires manual data selection to ensure high signal-to-noise ratios. The benefit of this labor intensive process is that the resulting model is able to resolve structure from the surface to 120 km depth. It therefore provides the missing link between previous crustal studies (ambient noise, controlled source [Trehu et al., 1994], and seismicity studies) and the larger scale models using teleseismic surface and body-waves, which have only longer wavelength or deeper sensitivity.

2.2 Cascadia segmentation

Several lines of evidence suggest that simple subduction with one downgoing and one overriding plate is an insufficient model of the Cascadia Subduction Zone. Instead, the subduction zone and arc are segmented, exhibiting variations in multiple characteristics along strike. A first order observation of this is the Sovanko and Blanco Fracture zones separating the Explorer and Gorda micro-plates from the main Juan de Fuca plate (Figure 2.1). A similar scale feature is the distinct change in strike of the trench from nearly north-south in California and Oregon to northwest-southeast through northern Washington and Vancouver Island [Audet et al., 2010; McCrory et al., 2004]. On a shallower scale, modeling of the GPS velocity field by McCaffrey et al. [2007] shows that the data is best fit by a series of crustal block motions rather than by pure plate motion based models.

The topography of the forearc provides further evidence of segmentation. The southern and northern ends of the subduction zone are mountainous, but the central region is relatively flat and low lying. The Klamath Mountains at the southern end of the subduction zone are composed of metamorphic oceanic rocks [Harden, 1998]. The Olympic Peninsula at the northern end of the study region is also composed of metamorphic and sedimentary oceanic rocks [Brandon et al., 1998]. However, the central lowland region is a mixture of sediment deposited from erosion of the Cascades Range and uplift of the Siletzia Terrane [McNeill et al., 2000]. The mid-crustal portion of the Siletzia Terrane is considered to be a captured oceanic arc and is often mapped by its enriched chemistry [Schmidt et al., 2008] and high seismic velocities [Trehu et al., 1994].

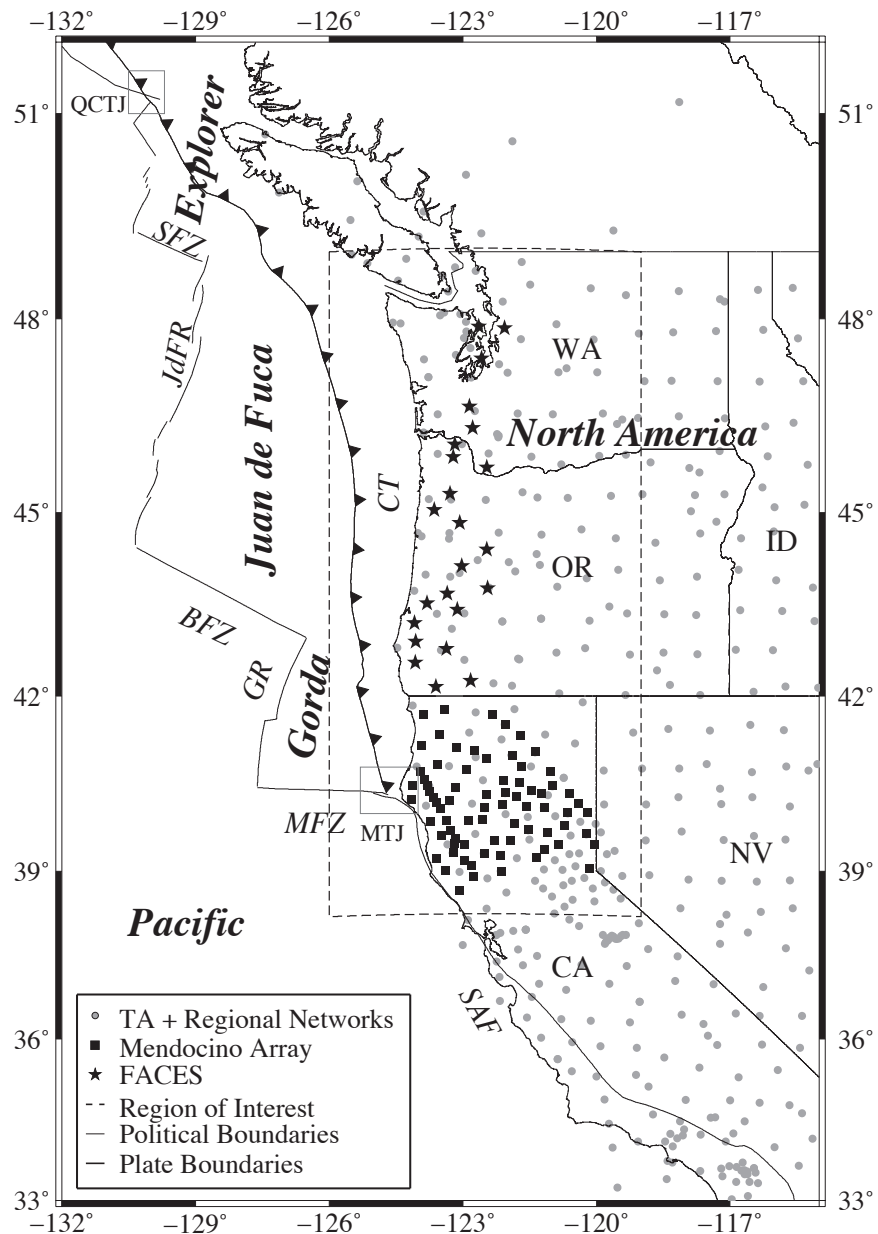


Figure 2.1: Station coverage of Pacific Northwest. Dashed box designates PNW10-S. FACES and FAME arrays designated by stars and squares respectively. Gray circles indicate non-FlexArray stations. Major features labeled as follows: MTJ - Mendocino Triple Junction, SAF - San Andreas Fault, MFZ - Mendocino Fracture Zone, GR - Gorda Ridge, BFZ - Blanco Fracture Zone, CT - Cascadia Trench, JdFR - Juan de Fuca Ridge, SFZ - Sovanko Fracture Zone, QCTJ - Queen Charlotte Triple Junction.

Variations in seismicity suggest another form of segmentation. The subduction zone is atypical everywhere in that there are no seismic events below 75 km depth anywhere along its length and thus the Wadati-Benioff zone is sparsely defined and shallow. There are a few subduction interface events deeper than the continental crust at the northern and southern ends of the subduction zone in Washington and California, but only to 75 km depth. However, there are almost no sub-crustal (>30 km depth) earthquakes beneath Oregon. In contrast, Episodic Tremor and Slip (ETS) events have been mapped throughout the subduction zone [Brudzinski and Allen, 2007]. The recurrence rate of ETS, consisting of many non-volcanic (or tectonic) tremors at the same time as geodetically measured backslip [Rogers and Dragert, 2003], varies along strike [Brudzinski and Allen, 2007] with similar segment boundaries as observed by the variation in seismicity and topography.

Other evidence for segmentation along the arc comes from the composition of arc volcanism. Detailed analysis of primitive basalt families in the main volcanic arc reveals variable mantle domains and melting regimes attributed to the effects of the slab window to the south, impingement of the Basin and Range terrane, and interaction with the Siletzia Terrane [Schmidt et al., 2008]. In addition, measurements of total heat production from volcanic fumaroles, thermal springs, and slightly thermal springs [Ingebritsen and Mariner, 2010] show significantly higher total heat production in the southern part of the arc where Basin and Range extension is thought to create permeable zones in the crust [Ingebritsen and Mariner, 2010].

2.3 Data and methodology

Our dataset focuses on two Flexible Array experiments, FlexArray along Cascadia Experiment for Segmentation (FACES) and the Flexible Array Mendocino Experiment (Mendocino), while also including data from the Berkeley BDSN, Canadian Seismic Network, USArray Transportable Array, and the Advanced National Seismic System (ANSS) backbone seismic network. We also include broadband stations from a total of 42 networks listed by network code in the acknowledgments resulting in a total of 1554 broadband stations. The dataset extends temporally from July 2007 through September 2010. While we focus on the Pacific Northwest, the dataset extends spatially throughout the entire United States with some coverage in Canada. The focus region and a broader subset of our station coverage are shown in Fig. 2.1.

We follow the method of Bensen et al. [2007] to compute empirical Green's functions (EGFs) from ambient noise cross correlations. For each broadband station, single day vertical component waveforms are time aligned, whitened to broaden the noise band, and filtered to isolate the fundamental mode Rayleigh wave between 5 and 150 seconds period. The cross-correlation is then computed for each station pair and stacked for the time period

when both stations are available. We then implement a frequency-time analysis [Dziewonski et al., 1969] with phase-matched filters [Levshin et al., 1989] to measure Rayleigh wave group and phase velocities from the EGFs.

The dominant source for the Rayleigh wave signal is the microseismic background noise [Bromirski et al., 2005; Landès et al., 2010]. Microseismic noise is strongest near the primary and secondary microseisms at 16 and 8 seconds period respectively [Cessaro, 1994], but broadly extends to 40 seconds period [Peterson, 1993]. We therefore treat the short period band (7-40 seconds) separately from the longer period (45-90 seconds) measurements. The short period phase velocities from 39 months of data (800,000 paths) are compared with a distribution of expected phase velocities (Fig. 2.2) computed from global and regional models including PREM [Dziewonski and Anderson, 1981], IASPI91 [Kennett and Engdahl, 1991], WUS [Pollitz, 2008], and GIL7 [Dreger and Romanowicz, 1995]. The measurements are then required to exceed a variable threshold for signal-to-noise ratio (SNR) and wavelength dependent inter-station spacing. Those data that are within 1 standard deviation of the expected value are given a relatively low threshold in both SNR and distance in order to be included in the later inversion, while those which fit within only 3 standard deviations must satisfy a higher threshold to pass. Those that are outside 3 standard deviations are rejected outright (see Table 2.1 for values).

The longer period measurements (45, 50, 55, 60, 65, 70, 80, and 90 seconds) are extracted from an 11-month, 200,000 path dataset. The 200,000 paths were manually graded based on the strength of signal in raw correlation and how well the dispersion curves fit to a reasonable distribution of phase velocities. This was facilitated through a Matlab GUI which displays information about each station pair individually. This information included the inter-station distance and azimuth, the number of days stacked in the correlation, the names of the two stations, the symmetric cross correlation, the measured group and phase velocities, and the measured spectral SNR. The user could then input an acceptable bandpass and grade them as excellent, good, average, poor, or rejected. To achieve good or excellent grades, the correlation needed to show a clear dispersive waveform around 3 km/s and a relatively smooth and continuous dispersion curve. The paths were then further selected via similar threshold SNR and distance criteria (see Table 2.1) as the automatically selected short period measurements, but with the manual grade in place of the standard deviation. This manually intensive approach has little effect in the short period band, but drastically improves the recovery at periods greater than 40 seconds. Other studies [Calkins et al., 2011; Yang et al., 2008] have incorporated measurements of phase velocity from earthquake-based methods. Both approaches are designed to stabilize the inversion at greater depths than are typically considered with ambient noise. In general, using earthquake derived long period phase velocities is preferable where available due to the time involved with the manual selection process.

The path integrated phase velocities are inverted for phase velocity maps using the

method of [Barmin et al., 2001]. Smoothing and damping weights are constant for each period. The smoothing uses a correlation radius of one wavelength to reduce short-wavelength anomalies. Fig. 2.3a-e, f-j shows the phase velocity maps for both the hand-picked and auto-picked data at a range of periods, and a comparison with the phase velocity maps of Pollitz and Snoke [2010] (Fig. 2.3k-o) from earthquake-based measurements. The earthquake-based approach is well established for periods greater than 18 seconds because those modes are strongly excited by teleseismic earthquakes. Ambient seismic noise is well established between 7 and 40 seconds as a source for seismic tomography [Bensen et al., 2007]. The two methods agree well in their overlapping passband (18-40 seconds). But, as can be seen in Fig. 2.3, the hand-picked ANT dataset shows much greater similarity to the Pollitz and Snoke [2010] phase velocity maps than the auto-picked ANT data does at periods greater than 40 seconds. The auto-picked long period maps are therefore rejected because they are dominated by short wavelength features not present in earthquake-based measurements. In the final inversion we therefore use the auto-picked ANT phase-velocities at 7-40 seconds and the manually selected ANT phase velocities at 45-90 seconds (shown in Fig. 2.3p-t).

In the final step we invert the phase velocities at each location for isotropic shear velocity. The phase velocities are first corrected for variable crustal thickness using the method of Pollitz and Snoke [2010]. A crustal thickness model (shown in Fig. 2.4) is interpolated from Audet et al. [2010] and Levander et al. [2007] with a minimum thickness of 10 km imposed. This model uses the detailed depth to mantle constraints of Audet et al. [2010] where the subducting plate is shallower than the continental Moho, and the Levander et al. [2007] constraints elsewhere. We then invert phase velocity perturbations using damped least squares and Fréchet kernels computed for the reference 35 km crust (crustal thickness variability has already been accounted for in the corrections to the phase velocity measurements). The inversion is damped towards a global mean of zero. For presentation we remove a depth dependent mean value and apply a final smoothing function with 25 km radius.

2.4 Noise source distribution

The theoretical basis for noise correlations returning an accurate and stable estimate of the Green's function between two stations relies on the assumption of homogeneously distributed noise sources. Using a large number of inter-station paths, long time periods, and symmetric sided correlations helps satisfy this approximation, but there is still debate about the source distribution of microseismic noise and therefore its suitability as a source for tomography. The long period earth hum located by Rhie and Romanowicz [2004] shows

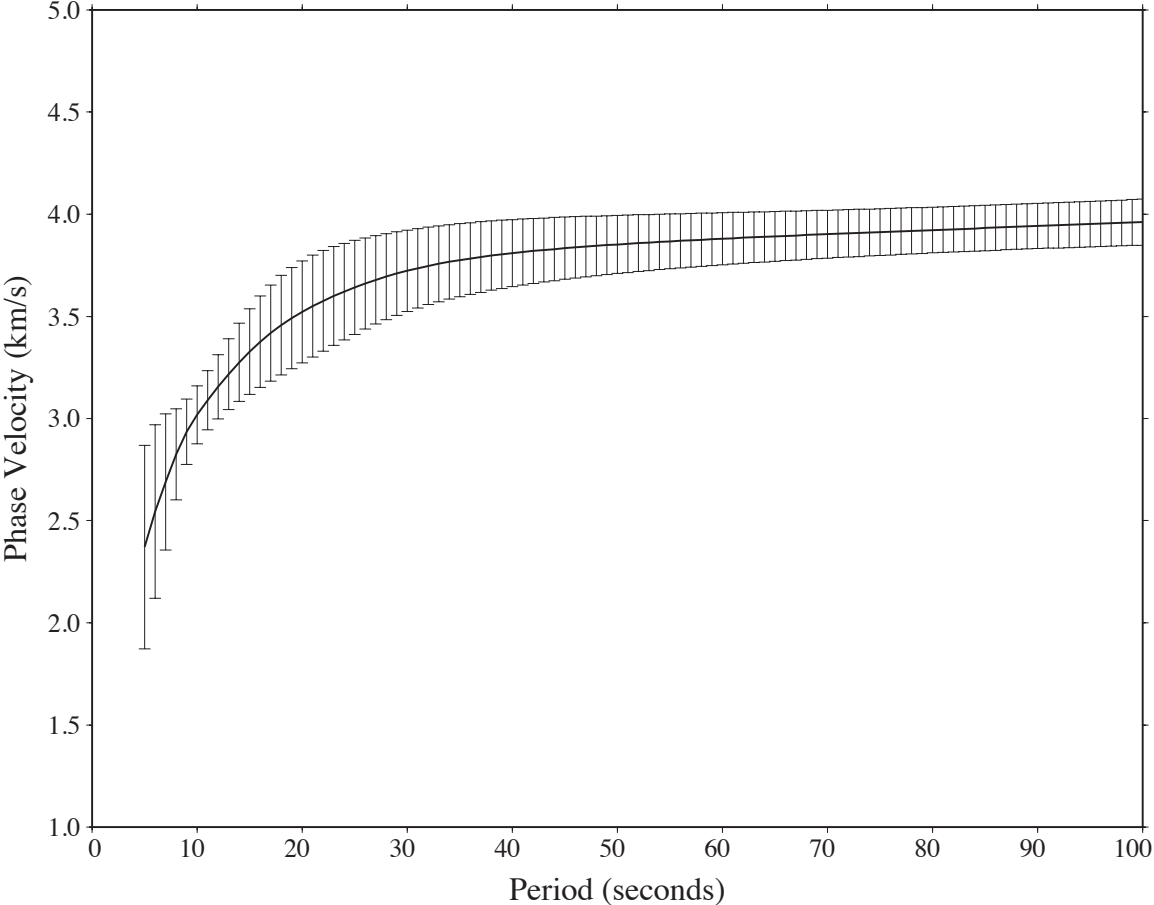


Figure 2.2: Mean and 1 standard deviation expected phase velocity curve computed from a set of 1D models.

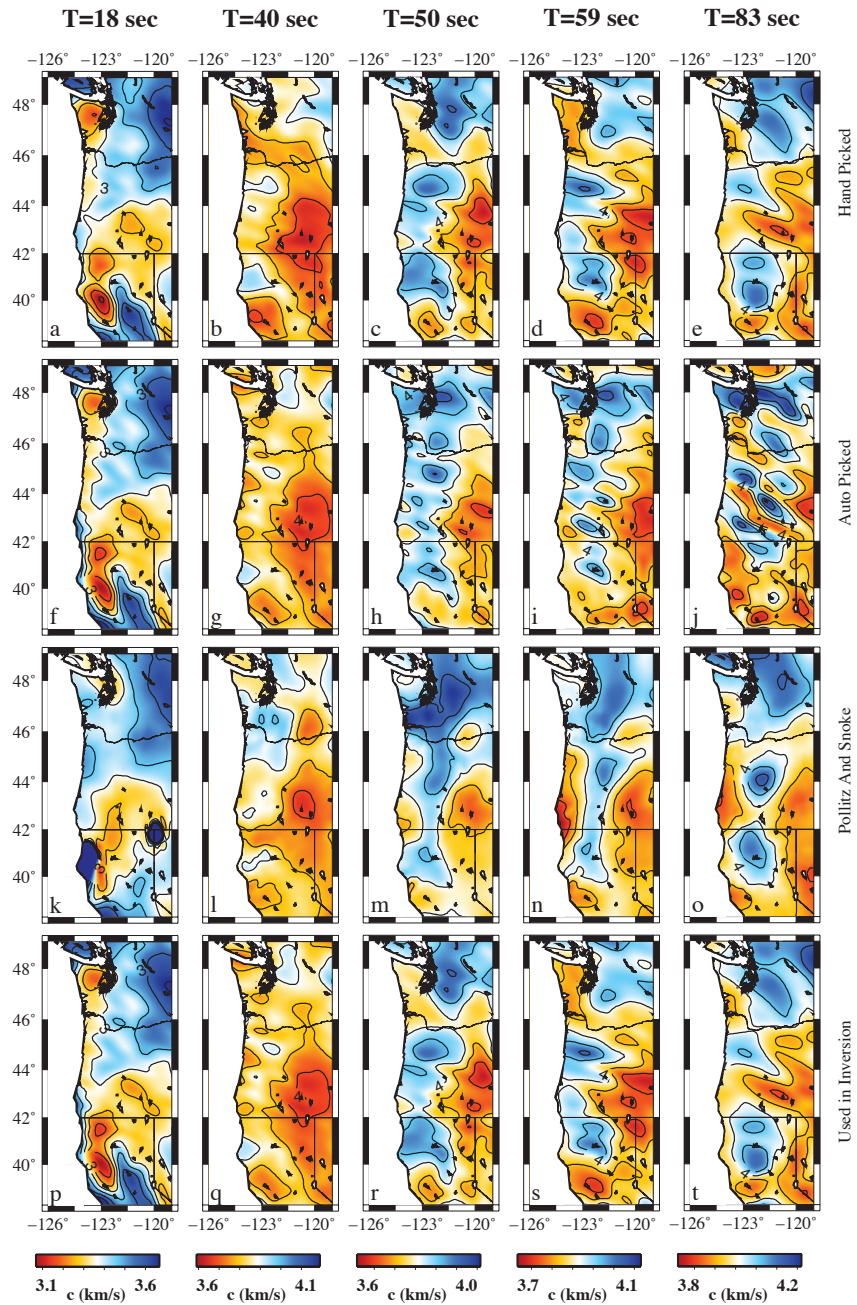


Figure 2.3: Phase velocity maps from PNW10-S. Top row (a-e) are from the hand-picked dataset. Second row (f-j) were determined by automatic selection criteria. Third row (k-o) are from a teleseismic method. Final row (p-t) are the phase velocity maps used in the inversion.

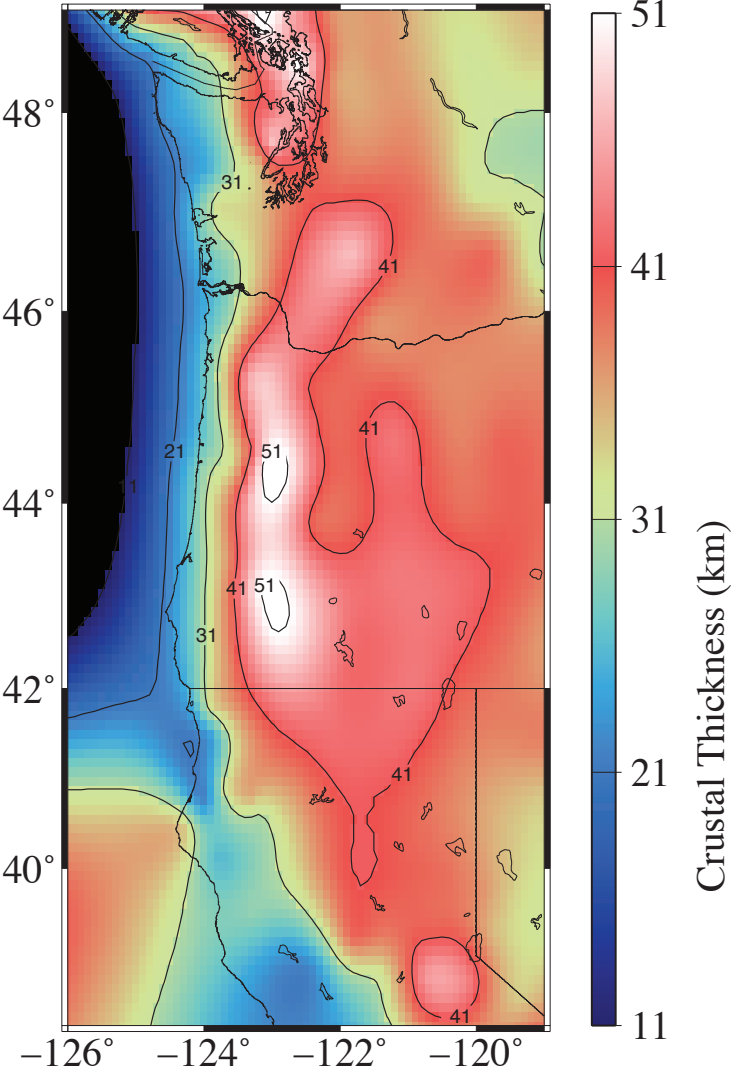


Figure 2.4: Map of crustal thickness used in our starting model. This was generated using receiver functions and imposing a 10 km minimum thickness.

Table 2.1: (top) Parameters used in automatic selection of phase velocities for periods of 740 seconds. A measurement which fits within the number of standard deviations from the reference model (S1) in the first column must pass the minimum SNR and minimum number of wavelengths in columns 2 and 3 corresponding to that row, i.e. a measurement within 1 standard deviation needs a minimum SNR of 5 and at least 2 wavelengths inter-station distance. (bottom) Parameters used for the hand-graded measurements.

Standard Deviations	Min SNR	Min number of wavelengths
1	5	2
2	20	3
3	30	4
4	30,000	40,000
Manual grade		
Excellent	2	1
Good	15	2
Average	20	3
Poor	30	4

the strongest energy is generated in the northern Pacific Ocean basin during the Northern Hemisphere winter and in the southern Pacific during the Southern Hemisphere winter. Other authors have located shorter period microseisms as a combination of deep-ocean and near shore sources [Bromirski et al., 2005]. Recent observations by Landès et al. [2010] have identified compressional waves in the secondary microseismic band within noise correlations, which back-project to similar winter sources as the hum.

We follow the beam forming method of Landès et al. [2010] to locate the source of energy in the cross correlations between station pairs within the Mendocino experiment (Fig. 2.1). Fig. 2.5 shows the azimuth of the peak energy from the center of the array in northern California for each month during the Mendocino Experiment. This shows the energy propagating to the northeast during the summer months and to the southeast in the winter months. Because the array is near a north-south trending coastline, a near coastal source should appear as nearly pure eastward propagating energy. Therefore it is more likely the energy is coming primarily from deep ocean activity during the winter months of the northern and southern hemisphere ocean basins. This implies that to maximize the distribution of noise sources in a measurement, the cross-correlation function should be computed over a period of 1 or more years. Optionally, sampling evenly between a few winter and a few summer months may also achieve a reasonable distribution of noise sources.

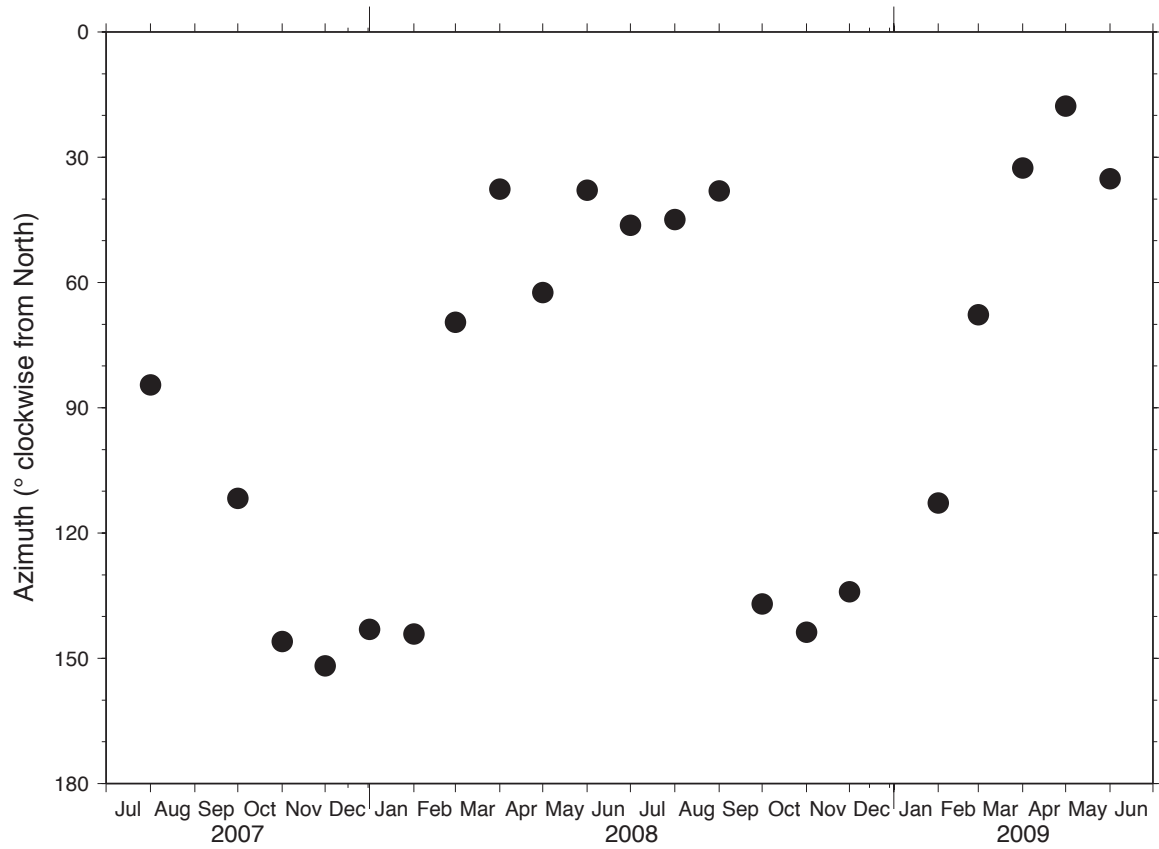


Figure 2.5: Azimuth of the maximum energy propagation direction with velocity between 2 and 5 km/s as a function of time. This is derived from the Mendocino array over the duration of the experiment and shows that the energy comes from the southwest in the summer and the northwest in the winter.

2.5 Resolution

We address the resolution of the model in three ways. The first two concern the inversion from path-averaged phase velocity to phase velocity maps, while the third assesses the full methodology. In the first approach we perform checkerboard resolution tests (Fig. 2.6a-e) at various periods to determine the ability of the data and inversion to resolve alternating high and low phase velocities. The recovery of these tests is dependent on both our ray-path coverage and chosen inversion parameters. To isolate the effect of the inversion parameters, we present an ideal recovery map (Fig. 2.6a) created by tracing 500,000 infinite frequency (thin) rays randomly generated in the model space through the input checkerboard with sides of $1.5^\circ \times 1.5^\circ$ and inverting with our inversion parameters. In a perfect inversion, the sides of alternating anomalies would be straight lines. The recovered checkerboard maps for a set of periods (8, 20, 40, and 70 seconds) are shown in Fig. 2.6b-e to illustrate the effects of both the ray coverage and the inversion parameters for the given period. Largely the recovery is good, but the 70 seconds period map's amplitude recovery is reduced compared to the shorter periods. Further, note that the checkers nearest the coast are smeared west relative to the ideal recovery map, which indicates reduced path coverage along the coast.

The second approach we use is the method of Barmin et al. [2001], which defines resolution as the minimum distance (km) at which two delta functions can be uniquely identified. The approach results in a spatial function describing areas of better or poorer coverage with lower values indicative of better resolution. These maps are shown in Fig. 2.7 for the same set of periods as the checkerboard test. These quantitative resolution maps show a decrease in resolution near the coasts and an overall reduction in the resolvable length-scale in the long period map which is reasonable for longer periods. Therefore deeper features near the coastlines cannot be considered fully resolved.

Finally we test the resolution of the full two-stage inversion approach by inverting our three-dimensional reference model. To create the reference model, we adjust the WUS model of Pollitz [2008], which has a 35 km Moho, to the Moho defined by our crustal thickness model at each spatial point. The three-dimensional shear velocity model is then converted to phase velocity for each period at each location by a propagator matrix method [Shapiro and Ritzwoller, 2002]. The rays used in our inversion are then traced through the synthetic phase velocity model to generate raw synthetic phase velocity observations. These data are then inverted as with the real data; first to determine phase velocity maps, and then the phase velocity maps are inverted using the same damped least squares method to obtain relative shear velocity. A perfect inversion should yield zero anomalies everywhere, indicating we recover the reference model. Deviations from zero are therefore indicative of artifacts. As seen in Fig. 2.8, the magnitude of the anomalies resulting from this test is very small and significantly lower than those in the final model. The distribution of these features is also randomly distributed without structure correlated to structure in our model. This suggests

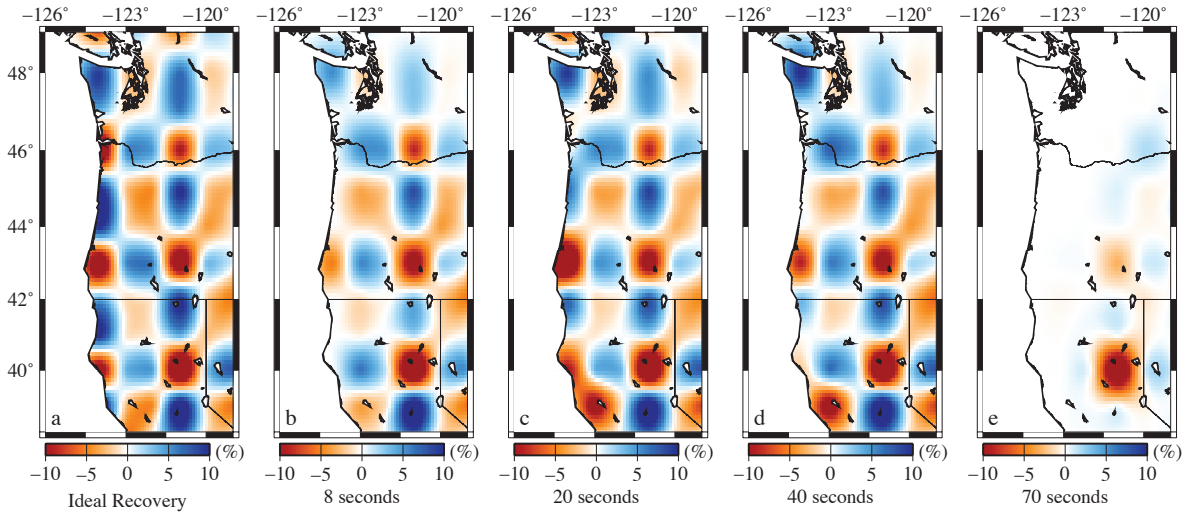


Figure 2.6: Checkerboard resolution test of ambient noise. The input synthetic velocity model has alternating boxes of high and low velocity $1.5^\circ \times 1.5^\circ$ in size with velocities of 5 ± 0.5 km/s. Panel (a) shows the recovery with 500,000 randomly distributed paths and tests the effect of the choice of inversion parameters. (b-e) show the recovered phase velocity maps for 8, 20, 40, and 70 seconds periods.

that our model does not contain significant structural artifacts resulting from the processing. However, because low amplitude structure in our model may be false, we focus on only the high-amplitude anomalies in our following interpretation.

2.6 Results

Map sections of the resulting model, PNW10-S, are shown in Fig. 2.9 with surface features and tectonic observations illustrated to the left (Fig. 2.9a and e). Crustal structure is seen in Fig. 2.9b-d and mantle structure is shown in Fig. 2.9f-h. The shallowest image at 5 km depth shows structure similar to mapped geology with sedimentary areas imaged as low velocity regions and mountainous regions as high velocity regions. In the mid crust, at 10 km and 15 km depths, the structure shows only limited correlation with surface features.

The Columbia Basin appears as a strong low velocity in the 5 km and 10 km images. The Sierra Nevada and Central Valley are distinct high- and low-velocity anomalies, respectively, at 5 km depth. The southern Cascade Range appears slow in the crust, while the northern Cascade Range is largely high velocity. The high velocity northern Cascade Range

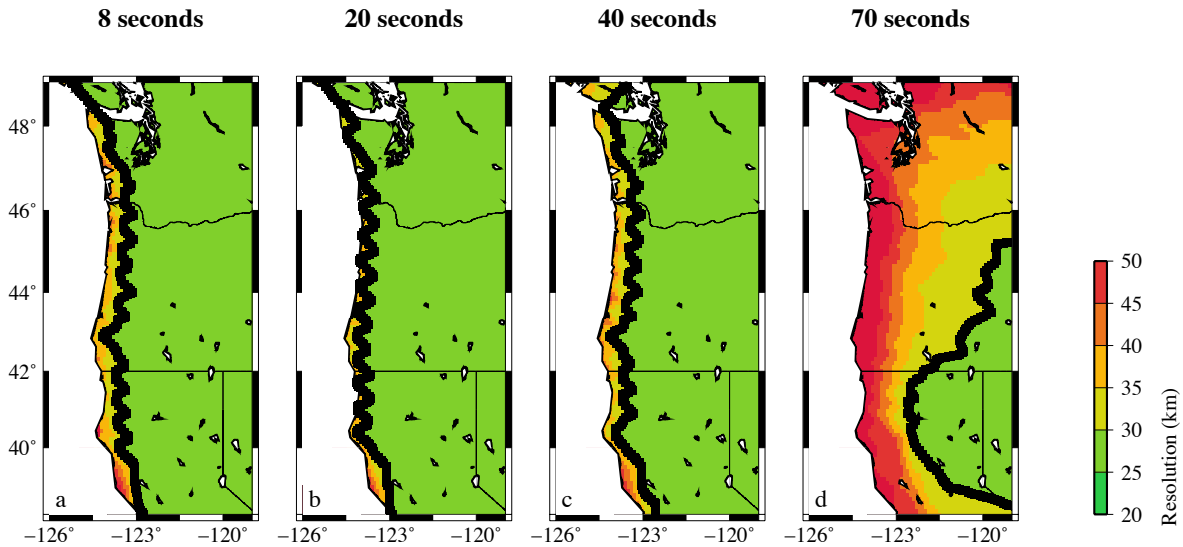


Figure 2.7: Minimum distance (km) at which two delta functions in phase velocity can be resolved. Lower values indicate greater resolving power. Thick black contour shows the 30 km limit.

merges with the high velocity region in the mid crust below the Oregon Coast Range and the Willamette Valley to the west and the eastern section containing the Columbia River Basalt. The Olympic Peninsula appears as a low velocity package dipping to the west.

An approximately linear north-south striking feature dominates the deeper images beginning near the coast at 35 km depth and progresses eastward with depth. This is the subducting Juan de Fuca slab. At 35 km depth a predominantly slow anomaly is observed beneath the onshore region with the edge of a high velocity feature just visible along the coastline. At greater depth, a broader high velocity feature is observed with low velocities to the east at each depth. The high velocity slab is segmented into two or three zones. The southern segment boundary is visible in slices from 35 to 100 km depth and is near the California-Oregon border (42°N). A northern segment boundary is also observed in the 100 km image near the Oregon-Washington border (46°N). However, this boundary is less consistent at different depths. In the 100 km map, the high velocity anomaly is broadest which is probably due to the drop in resolution near the coast, particularly at longer wavelengths.

Fig. 2.10 shows a cross section through the southern portion of the subduction zone. Fig. 2.10a shows color scales of absolute velocity in the crust and relative velocity in the mantle. For comparison, Fig. 2.10b has the entire section in relative velocity. While both images

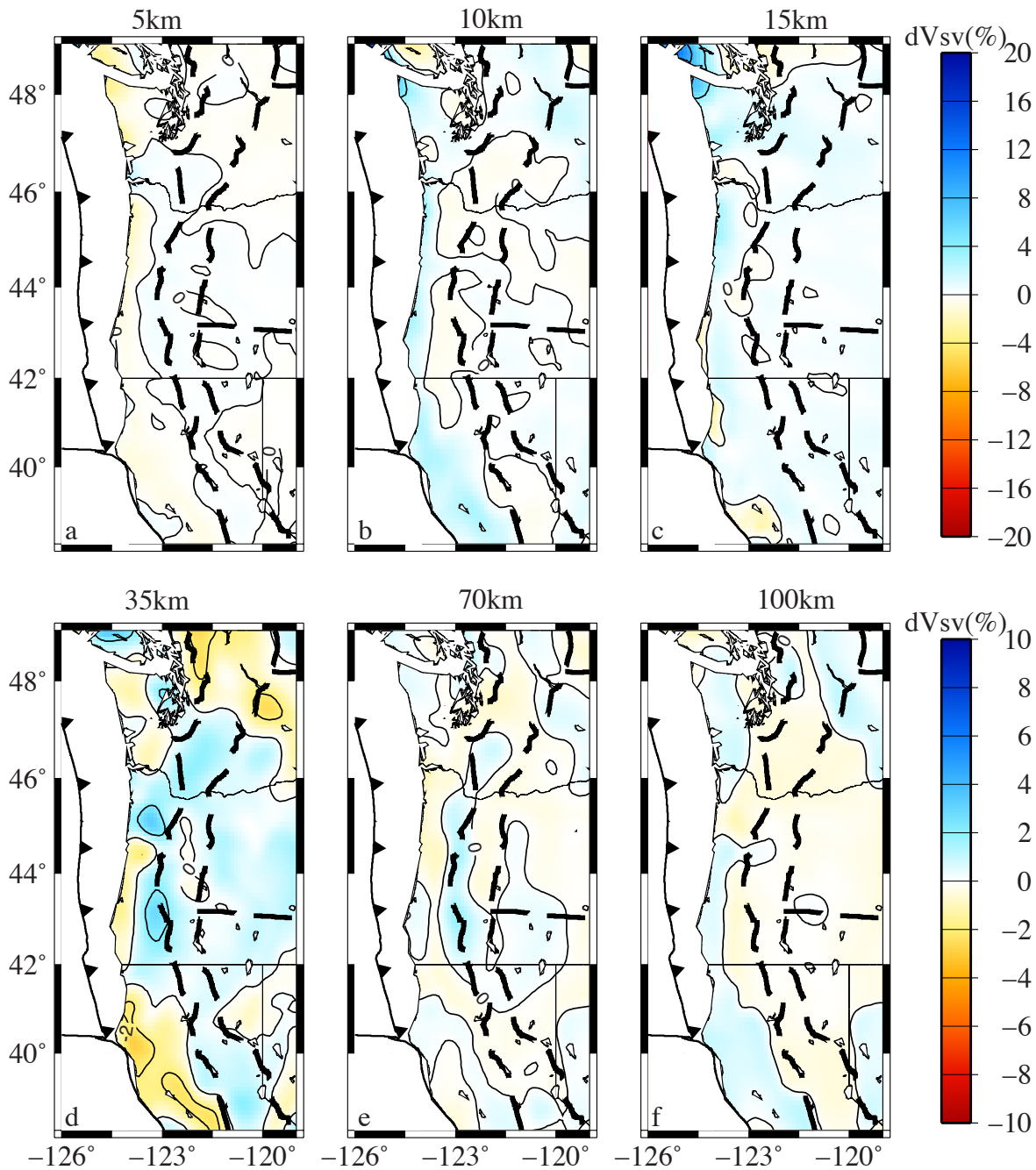


Figure 2.8: Result of inverting synthetic phase velocity data generated from our 3D starting model. With perfect resolution we would resolve zero anomalies; deviations from zero represent artifacts introduced by the data distribution and modeling procedure. The anomalies recovered are all low amplitude and do not show correlation with the predominant structure in our model.

display essentially the same structure, major features are more prominent in Fig. 2.10b and thus we use a relative velocity scale for the fence diagrams in Figs. 2.11 and 2.12 discussed below.

2.7 Discussion

The continental crust is an amalgamation of multiple blocks that have been accreted to the continent. The Klamath Mountains are a crystalline block of oceanic material [Harden, 1998], which is relatively fast in the upper crust, but relatively slow in the deep crust. The high velocity mid-crust under central Oregon is the Siletzia Terrane [Snavely et al., 1980]. Above the Siletzia, the Oregon Coast Range and Willamette Valley are low velocity features. McNeill et al. [2000] reconstruct this as uplift of the Siletzia with older sedimentary cover and backfill of the basin with younger sediments. The Olympic Peninsula is a largely slow anomaly owing to a sedimentary and metamorphic core formed through a continuous mass recycling process in the accretionary wedge [Brandon et al., 1998]. Furthermore, the Crescent formation basalts form a high velocity half ring on the eastern side of the sedimentary core, which is expected for the large basaltic feature [Babcock et al., 1992].

The crust of the Cascades Range shows a strong north-south dichotomy in terms of velocity structure with higher velocities in the north and lower velocities to the south. Ingebritsen and Mariner [2010] show a similar separation near 45.25°N based on the total heat production measured in hydraulic systems near volcanic centers. They interpret this as impingement of Basin and Range extension in the crust of the southern arc leading to more permeable pathways for fluid circulation. This coincides well with the low velocities imaged in the upper crust of the southern region. However, the imaged low velocities in the southern region extend to far greater depths than heated fluids could circulate [Saar and Manga, 2004]. Thus we consider the large scale low velocity anomalies as regions of magmatic plumbing systems, but we are unable to uniquely constrain the dimensions of individual magma chambers due to the scale of our model and smoothing inherent in tomographic inversions.

The deeper structures (>30 km) can be readily interpreted in terms of subduction zone features. In the 35 km map, the Juan de Fuca plate appears as a relatively slow anomaly beneath onshore regions as we are imaging the subducting oceanic crust including sediments and possible fluids while the other material at that depth is either mantle peridotite or deep crustal granitoid with little water content. Low velocities above the plate interface may reflect fluid rich oceanic sediments being underplated to the continent as described in Calkins et al. [2011]. In the deeper images, the fast velocity is the subducting oceanic lithosphere, which is colder than the background mantle due to exposure near the surface. In the mantle, the slab appears segmented into at least two, and possibly three, sections with high velocity cores at 41°N , 45°N , and 47.5°N and reduced high velocities at the boundaries at 42°N and

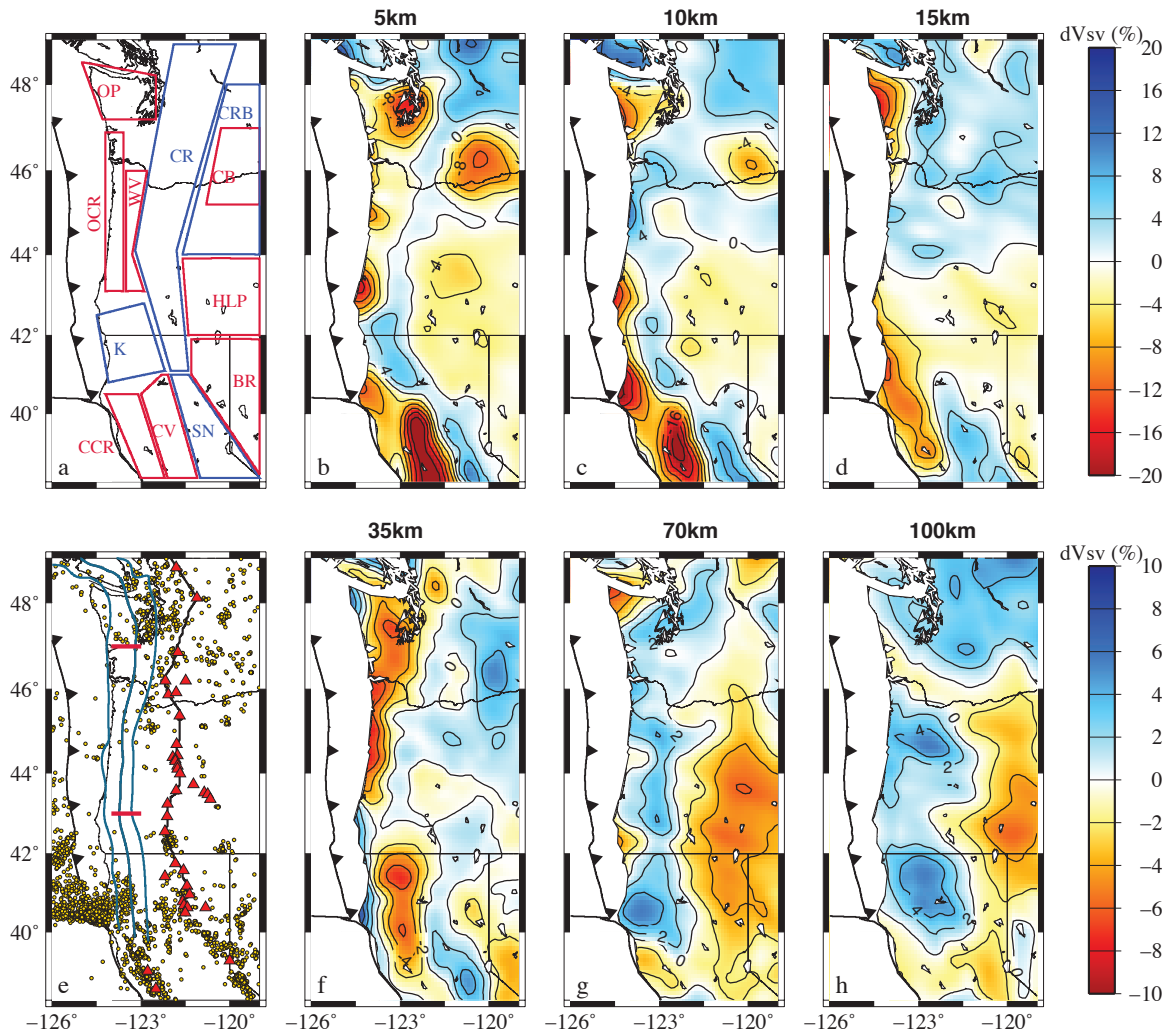


Figure 2.9: (a and e) Tectonic maps of the Pacific Northwest. (a) Highlights crustal structure showing sedimentary regions in red and igneous/metamorphic regions in blue. OP - Olympic Peninsula, CR - Cascades Range, CRB - Columbia River Basalts, OCR - Oregon Coast Range, WV - Willamette Valley, CB - Columbia Basin, K - Klamath Mountains, HLP - High Lava Plains, BR - Basin and Range, CCR - California Coast Range, CV - Central Valley, SN - Sierra Nevada. (e) shows earthquakes since 1990 (gold dots), tremor segmentation bounds (red lines), volcanoes (red triangles), depth to slab contours at 20, 30, and 40 km (blue lines), and the locations of profiles in the following figures. (b-d, f-i) Depth slices of PNW10-S at 5, 10, 15, 35, 70, and 100 km. Overlaid on the depth slices are the quaternary volcanic centers as unfilled triangles.

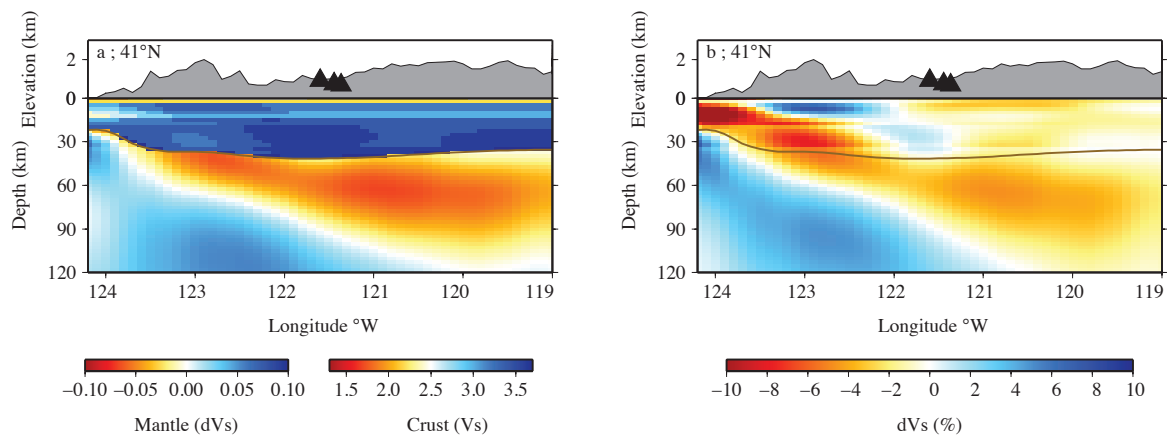


Figure 2.10: East-west cross-sections of PNW10-S at 41°N through the Klamath Range. Panel a gives the best fit shear velocity in the crust and perturbation in the mantle. Panel b shows only relative velocity perturbations after a depth-dependent mean value is removed. In both cases the topography is shown in gray over the structure. Active Quaternary volcanoes within 30 km are overlain on topography and the Moho is overlain on the shear velocity structure. All depths and elevations are in km. Velocity scales are shown at the bottom of the figure.

46°N. The northern edge of the southernmost segment coincides with the landward continuation of the Blanco Fracture Zone near the California-Oregon border (42°N), and which separates the Gorda and Juan de Fuca sections of the subducting plate. Thus we interpret the southern slab segment as the Gorda microplate. The second segmentation boundary is near the Oregon-Washington border (46°N) where a low velocity corridor separates the central and northern segments. This northern segmentation boundary is less clear in our model, but similar to an area of reduced high velocity imaged in teleseismic body wave studies [Obrebski et al., 2010].

2.7.1 Implications for tremor

Brudzinski and Allen [2007] identify a variation in the recurrence interval of ETS along the arc with a recurrence interval of 14 months in the north, 20 months in the center, and 11 months in the south. We seek to expand on that observation by investigation of three-dimensional structure. ETS events are typically thought to occur on the plate interface [Brown et al., 2009; Ghosh et al., 2009; Shelly et al., 2007] between 30 km and 45 km depth [Audet et al., 2010]. The cross section in Fig. 2.11c is constructed by extracting the velocity values along a profile aligned to the 30 km slab contour from Audet et al. [2010], which is thought to represent the up-dip limit of ETS. Superimposed on this image are the long-term ETS segmentation boundaries at 43°N and 46.7°N [Brudzinski and Allen, 2007]. These boundaries, based on the recurrence interval for ETS events, are aligned with both the location of the high velocity Siletzia Terrane in the mid-crust (15 km depth) and also the deeper three-way segmentation in the subducting oceanic lithosphere between the Gorda, Southern Juan de Fuca, and Northern Juan de Fuca at 60-120 km depth as described above. Thus the segmentation of ETS is aligned with structural boundaries in both the continental crust and the subducting oceanic lithosphere.

The frequency of tremors along the strike of the subduction zone is shown in Fig. 2.11a [Boyarko and Brudzinski, 2010]. The three peaks in the proportion of events around 41°N, 42.5°N, and 48°N do not correspond to peaks or troughs in topography or to significant structural anomaly centers of crustal or lithospheric blocks as imaged tomographically. However, they do correspond to regions with strong lateral gradients in the upper crust (0-15 km depth). This correlation between tremor frequency and near surface structure is surprising because tremor is believed to be occurring at greater depths. This may imply that the conditions for tremor generation are dependent on upper crustal structure whether they occur on the plate interface or throughout the continental crust [Kao et al., 2005].

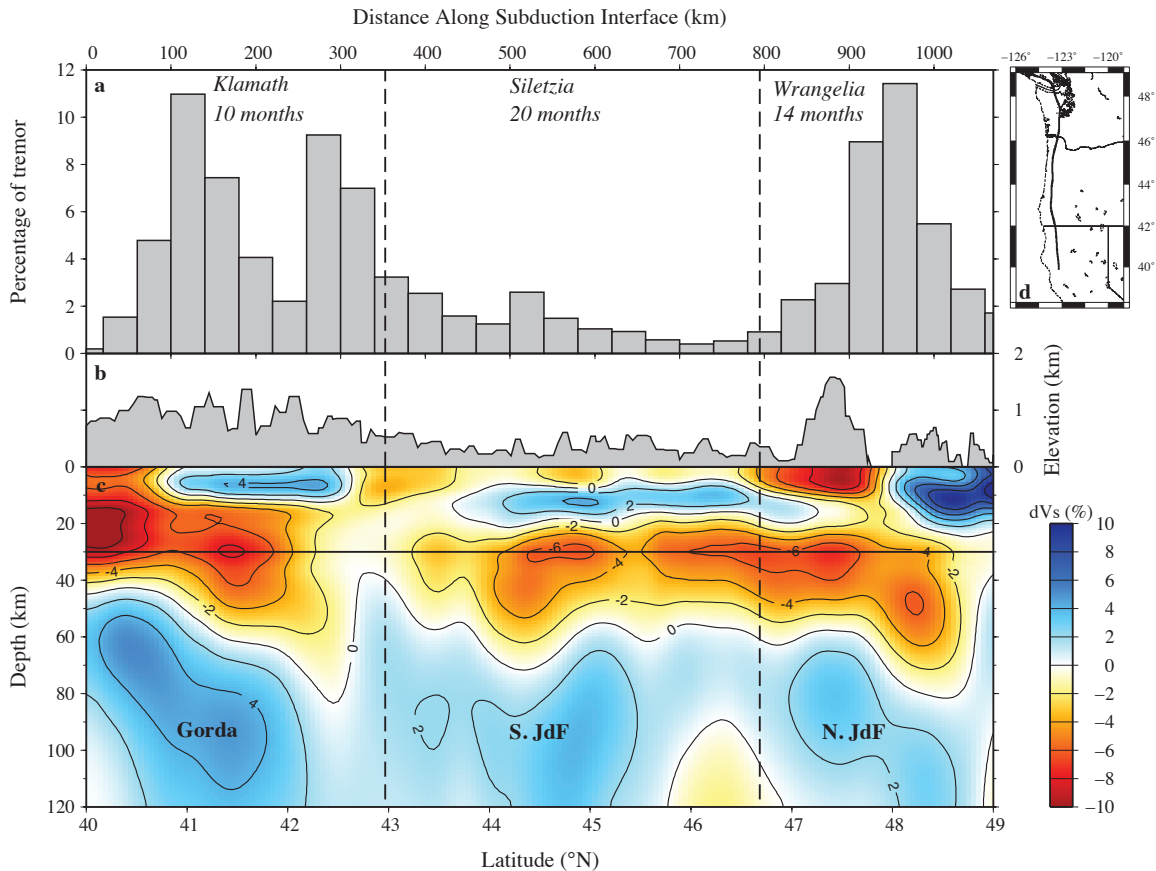


Figure 2.11: Comparison of PNW10-S with characteristics of ETS. (a) Histogram showing variability in tremor occurrence along strike [Boyarko and Brudzinski, 2010]. (b) Topography along profile. (c) Relative shear velocity structure along a profile where the slab is at 30 km depth (profile location shown in d). Vertical lines on profile at 43 $^{\circ}$ N and 46.7 $^{\circ}$ N indicate the tremor segmentation bounds of Brudzinski and Allen [2007] with the names and recurrence interval given. The horizontal line is the top of the ocean crust from Audet et al. [2010]. Also labeled are the slab sections corresponding to the Gorda, Southern Juan de Fuca (S. JdF) and Northern Juan de Fuca (N. JdF).

2.7.2 Implications for volcanic activity

Fig. 2.12 shows a set of observations along the axis of the Cascades volcanic range. Fig. 2.12a is modified from Ingebritsen and Mariner [2010] showing cumulative heat production from the north to the south as measured from volcanic fumaroles, thermal springs, and slightly thermal springs. Comparing this to PNW10-S (Fig. 2.12c) shows a strong correlation between the high heat production south of 45°N and a large zone of low velocities between 40.5°N and 45°N . The water-based measurements for the total heat production sample fluids circulating between 0 and 15 km depth [Saar and Manga, 2004] and thus Ingebritsen and Mariner [2010] interpret this high heat production zone as due to the influence of extension from the Basin and Range province creating permeable pathways for fluid flow in the upper crust. This helps explain the low velocity zone in the upper crust (Fig. 2.12c; anomaly SC), however the low velocity zone extends to 80 km depth.

The extension of the Basin and Range, and the associated clockwise rotation of the Cascadia margin [Bates et al., 1981; McCaffrey et al., 2000], could explain the lower velocities in the southern half of the subduction zone at all depths (Fig. 2.12c; anomalies SM1, SM2, and SM5). The rotation leads to extension at the southern end, which promotes melting and results in the larger low velocity zone. The center of this low velocity zone is also located at the slab segmentation boundary (at 43°N , Fig. 2.12c, anomaly SM5) described earlier and associated with the continuation of the Blanco Fracture Zone separating the Gorda and Juan de Fuca portions of the plate. The Gorda portion of the plate is actively deforming to a much greater extent than the Juan de Fuca section to the north. This is evidenced by an echelon strike-slip seismicity throughout the plate, and the clockwise rotation of magnetic anomalies relative to the Gorda Mid-Ocean Ridge and also relative to the magnetic anomalies north of the Blanco Fracture Zone as seen in the North American Magnetic Anomaly Database [NAMAD, 2011]. This may also imply increased rotation of the Gorda segment relative to the Juan de Fuca portion. This could promote separation of the Gorda and Juan de Fuca plates below the trench exposing more of the slab to hot mantle resulting in increased melting and further increased plate separation. The low velocity feature below 90 km which separates the slab segments at 43°N (anomaly SM5) may therefore be a channel feeding melt to the southern section of the arc. The other slab segmentation boundary discussed above is defined by the deep low-velocity anomaly between 45°N and 46°N (anomaly SM6). This feature is not coupled to broad low velocities beneath the arc. As described above, this segment boundary is less clearly defined in the tomography, and there is no association with differential deformation processes as in the case of the Gorda-Juan de Fuca. In the northern portion of the arc there is also reduced extension, which would not promote melting as it does to the south.

In addition to the large-scale north-south variability in the velocity structure beneath the arc, we observe four smaller-scale pockets of low velocity just below the Moho near 42°N , 44°N , 47°N , and 49°N (anomalies SM1, SM2, SM3, and SM4 respectively). These may be

regions where melt is ponding and differentiation is occurring before the melt continues its path up through the crust. Evidence from Schmidt et al. [2008] suggests there are four distinct source regions for the arc melts along Cascadia and the boundaries that they identify correlate approximately with the locations of the four low-velocities at the base of the Moho. Recent numerical modeling by Karlstrom et al. [2009] describes how crustal magma chambers between the surface and 30 km depth grow by capturing feeder dikes from below the magma chamber. The individual crustal magma chambers are likely too small to be resolved by our tomography, but these broader low-velocity pockets below the Moho are likely the sources of the feeder dikes, which become captured in relatively discrete mid-crustal magma chambers before being erupted at the surface with the observed evidence of variable source characteristics.

2.8 Summary

By utilizing ambient noise tomography at longer periods than is typical (to 90 seconds), a single method based velocity model of the entire lithosphere is resolved allowing us to address questions relating to processes within the continental crust, and the relationship of these processes to lithospheric-mantle structure and the underlying subducting oceanic crust and mantle in the Cascadia Subduction Zone. At shallow depths (5 km) the velocity structure correlates well with surface geologic observations as basins are imaged as low velocity features and mountain ranges show high velocities. Below 10 km depth, structure transitions from a reflection of crustal blocks to structure dominated by the subducting slab at 70 km depth. The slab is imaged as a broad high velocity feature with a thin low velocity layer on top believed to be the subducting oceanic crust.

Episodic tremor and slip is observed along the length of Cascadia, but the characteristics vary along strike. The recurrence interval of ETS defines three zones along the arc with a recurrence interval of 14 months in the north, 20 months in the center, and 11 months in the south [Brudzinski and Allen, 2007]. These three segments correlate well with several structures within PNW10-S. The three segments of the subducting plate align with the ETS segmentation, and the mid-crustal location of the Siletzia Terrane aligns with the region of 20-month recurrence. We also note that the three peaks in tremor activity are collocated with upper crustal lateral velocity gradients.

While the slab is imaged all along the Cascadia margin, it shows strong variability in structure. Three segments are apparent at 100 km depth, which is consistent with deeper structure [Obrebski et al., 2010]. The southern segment appears to be an extension of the Gorda section of the plate implying that the continuation of the Blanco Fracture Zone below the trench is a weak zone allowing increased clockwise rotation of the Gorda slab and/or

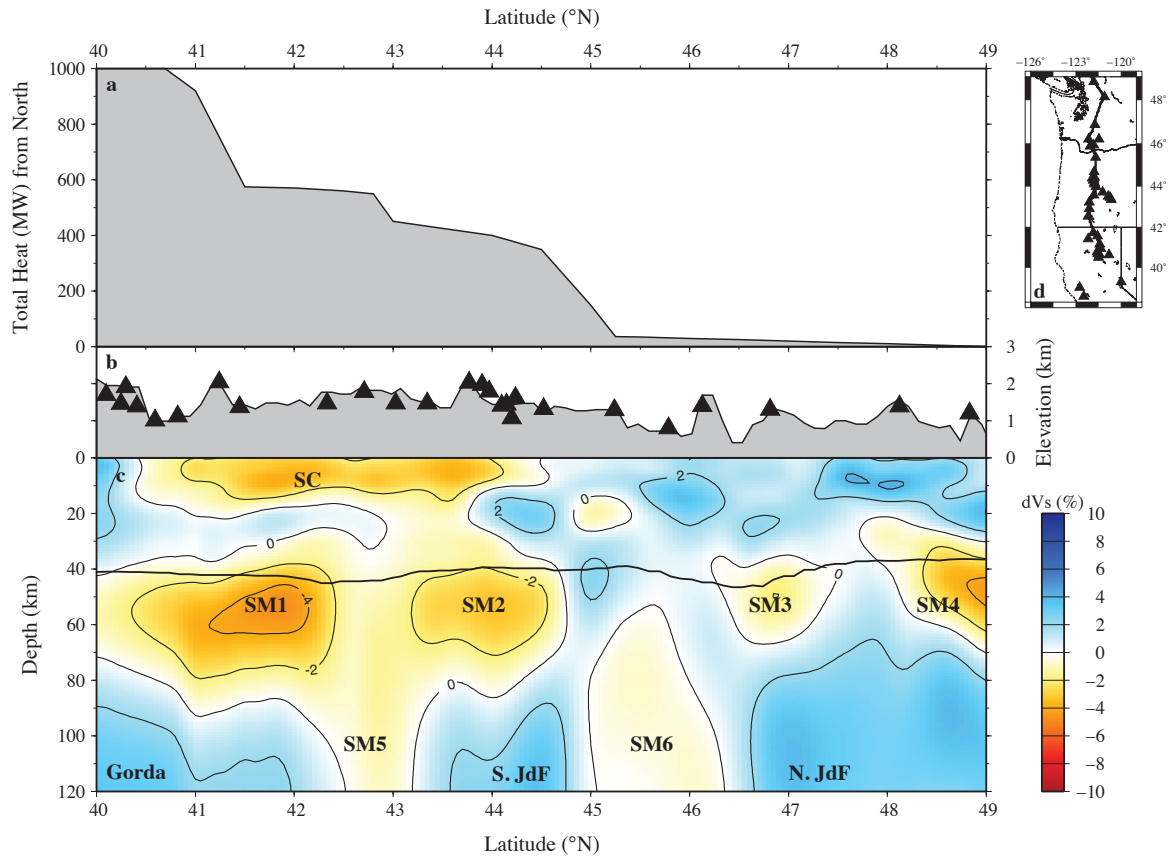


Figure 2.12: Comparison of PNW10-S with heat production observations. (a) Cumulative heat production from the north to south along the arc (modified from Ingebritsen and Mariner [2010]). (b) Topography along profile with nearby volcanoes plotted as triangles. (c) Shear velocity structure along the profile that runs along the arc. Profile shown in the upper right (d). The black line around 40 km depth is the Moho. Major anomalies are labeled. Slow crust (SC) is the area of Basin and Range impingement. Slow mantles (SM14) are the interpreted ponded areas of melt. SM5 and SM6 are the plate segmentation boundaries separating the Gorda, Southern Juan de Fuca (S. JdF), and Northern Juan de Fuca (N. JdF).

increased melting along its locus. The entire southern half of the arc (south of 45°N) is lower velocity than the northern half. Total heat production measurements [Ingebritsen and Mariner, 2010] show the same northsouth divide and we observe lower velocities in the shallow crust (0-15 km depth), which correlates well with the higher heat production. While the lower crust shows no strong velocity anomalies, lower velocities are again seen below the Moho to a depth of 80 km. We propose that increased melting along the extension of the Blanco Fracture Zone, promoted by the clockwise rotation of the arc and the associated extension in the south, is responsible for the lower velocities and increased heat production in the southern portion of the arc. We further note the location of four distinct pockets of low velocity just below the Moho. These are likely regions where melt is ponding and differentiating before the lighter components rise through the crust. These are likely the source of the feeder dikes drawn on by crustal magma chambers [Karlstrom et al., 2009].

The full published version of this chapter was published in *Earth and Planetary Science Letters* [Porritt et al., 2011] and can be found through doi: 10.1016/j.epsl.2011.06.026.

2.9 Chapter Acknowledgements

Awards EAR-0643392, EAR-0745934, and EAR-0643077 from the National Science Foundation's Earthscope program funded this work. We would like to thank a multitude of fieldwork helpers involved with the FACES and Mendocino experiments including Hector Hinojosa, Eugene Humphreys, Alan Levander, Leland O'Driscoll, Pat Ryan, Stefany Sit, Andrew Tran, and Yongbo Zhai. All figures were made with GMT [Wessel and Smith, 1998]. We thank Morgan Moschetti, Michael Ritzwoller, Anatoli Levshin, and Mikhail Barmin for providing FTAN and path tomography codes. We thank Mathieu Landes and Nikolai Shapiro for codes to calculate forward dispersion models and to locate energy in cross-correlations. We thank Oliver Kreylos and Louise Kellog for providing 3D Visualizer software used in our interpretation. Thanks to the PASSCAL Instrument Center for help installing and maintaining the stations as well as for helping process the data for archival at the IRIS DMC. Data was obtained from the IRIS DMC, the NCEDC NETDC for BDSN data, and the Canadian Seismic Network's AutoDRM from the Geological Survey of Canada for Canadian data. The networks providing data are: AZ, BK, CC, CI, CN, CO, EP, ET, HW, II, IM, IU, IW, LB, LD, LI, NE, NM, NN, NR, PB, PE, PN, SC, TA, UO, US, UU, UW, WY, XC, XE, XQ, XR, XT, XU, XV, Y8, YU, YW, Z2, and ZG. Finally we thank Mathias Obrebski, Pascal Audet, Leif Karlstrom, and two anonymous reviewers for insightful comments.

Chapter 3

Imaging east of the Rocky Mountains with USArray: DNA13 model update and validation

Advisor: Richard M. Allen

Coauthor: Fred F. Pollitz

3.1 Introduction

The ability to map the internal velocity structure of the Earth is rapidly advancing due to the seismic waveform dataset provided by USArray. Prior to the array (with a 70 km station spacing) rolling across the U.S., global models showed a clear contrast between the deformational western U.S. from the stable cratonic eastern U.S. in the upper 200 km [van der Lee and Nolet, 1997]. In the lower mantle, the relatively cold Farallon slab is visible below the transition zone in the eastern U.S., contrasting with the warm to neutral mantle under the western U.S. [Grand, 1994; van der Hilst et al., 1997]. Body wave tomography models utilizing USArray are now recovering high-resolution images, primarily in the western U.S., revealing dynamic interactions between high velocities, interpreted as slabs and drips, and low velocities such as the Yellowstone Plume and the Rio Grande Rift [Burdick et al., 2008; James et al., 2011; Obrebski et al., 2011, 2010; Schmandt and Humphreys, 2010; Sigloch, 2011; Xue and Allen, 2010]. Now that USArray is crossing the Midwest U.S. and approaching the east coast, the picture that is emerging begins to contain elements of both the high-resolution body wave models and the longer wavelength global models.

The observable geologic history of the North American Continent begins in the Paleoproterozoic (2.0-1.8 Ga) with the accumulation of Archean continents to form the core of the Laurentia Craton [Whitmeyer and Karlstrom, 2007]. In the western two thirds of North America (the study region for this chapter) the most notable Archean province is the Wyoming Province [Foster et al., 2006; Roscoe and Card, 1993; Ross, 2002]. This province is linked to Laurentia on the east by the Trans-Hudson Orogen, to the northwest by the Little Belt Arc, and to the South by the Cheyenne Belt (Fig. 3.1). Following the accretion of the

Wyoming Province, a series of orogens grew the continent from the south-southeast starting with the Yavapai (1.8-1.7 Ga), then the Mazatzal (1.7-1.6 Ga), and finally the Grenville (1.3-1.0 Ga). Plutons associated with these orogens helped weld together the young continent and allow precise age dating. During the Grenville orogeny, the last major continental component of the Precambrian craton, the Llano province, formed a distinct sequence associated with back-arc rifting, crustal formation, and ocean closure through northward-directed subduction [Mosher, 1998]. Major rifting events also contribute to the mosaic of Laurentia, including the 1.2-10 Ga Keweenaw Mid-Continent Rift [Van Schmus and Hinze, 1985] and the (\sim 500 Ma) Cambrian Southern Oklahoma Alucogen [Keller and Stephenson, 2007] and Reelfoot Rift [Braile et al., 1986].

The late Mesozoic and Cenozoic tectonism is largely controlled by eastward progressing subduction of the Farallon plate [Schellart et al., 2010]. The Juan de Fuca, Gorda, and Monterey [Wang et al., 2013] plates are the young western remnants of the Farallon observable off the U.S. west coast. The long history ($>$ 150 Ma) of this plate has contributed to significant tectonic uplift and magmatism throughout the western U.S. The inboard uplift of the Rocky Mountains and magmatic hiatus from 90-30 Ma followed by the ignimbrite flare-up indicates the slab became flat during this period [Humphreys et al., 2003]. When the Farallon Ridge subducted at 30 Ma the plate boundary transitioned to transform motion between the North American and Pacific plates [Atwater and Stock, 1998]. Following this transition, the 17 Ma emplacement of the Columbia River Basalts and subsequent Yellowstone and Newberry hotspot tracks indicate continued deformation due the Farallon plate and dynamic interaction with the Yellowstone plume [Darold and Humphreys, 2013; James et al., 2011; Liu and Stegman, 2011; Obrebski et al., 2011].

In this chapter we present the new tomographic model, DNA13. This model contains four independent estimates of the isotropic velocity structure useful for imaging relative mantle thermal and compositional anomalies. We address the validity of the model through an assessment of its predictive power against a synthetic waveform dataset computed for a 3D global model. We then use DNA13 to compare and contrast the Archean Wyoming craton and the Mesoproterozoic Llano province. Below the mantle transition zone, the Farallon slab is observed to have significant topography and two isolated high velocity anomalies. We propose this variability may be due to heterogeneity from a ridge and geometrical forcing during subduction.

3.2 Method

The DNA13 models are constructed in a similar manner as DNA09 [Obrebski et al., 2010] and DNA10 [Obrebski et al., 2011], but with some significant updates. For the body wave

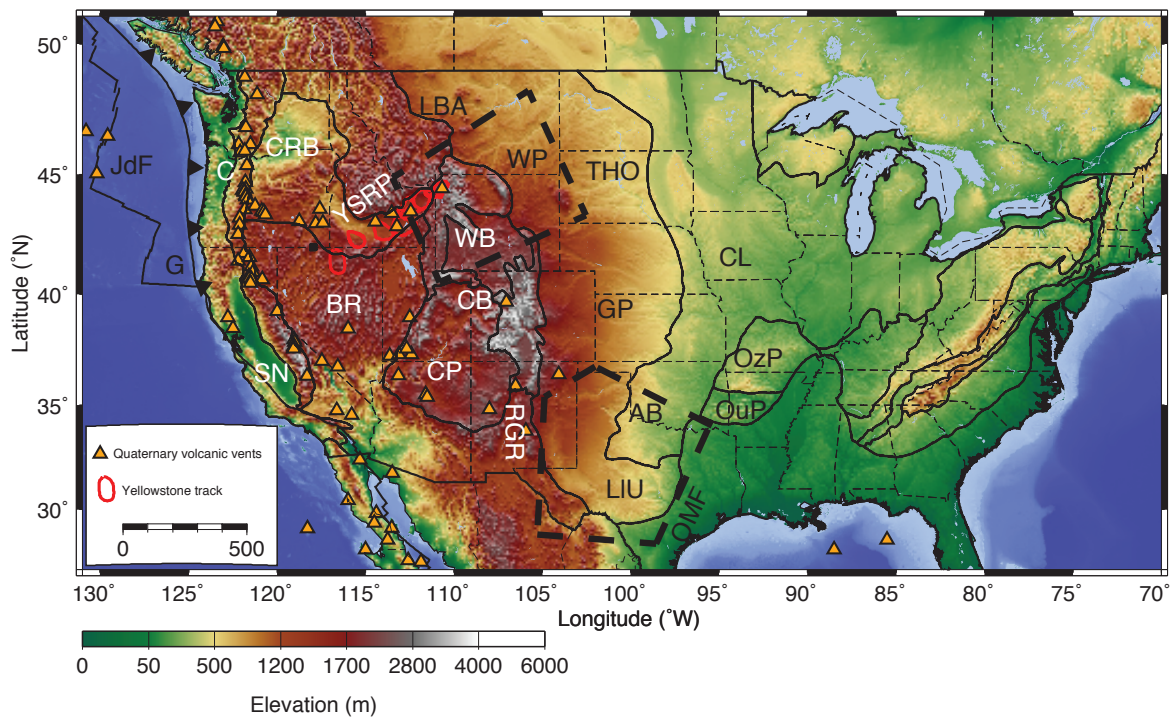


Figure 3.1: Topographic map of the continuous U.S. Also highlighted are the physiographic boundaries [Fenneman and Johnson, 1946], Quaternary volcanic centers, the Yellowstone track, plate boundaries, and dashed outlines approximating the Wyoming Province (WP) and Llano Province (LIU). Abbreviations: Juan de Fuca Plate (JdF), Gorda Plate (G), Cascades (C), Sierra Nevada (SN), Columbia River Basalts (CRB), Basin and Range (BR), Yellowstone-Snake River Plain (YSRP), Colorado Plateau (CP), Little Belt Arc (LBA), Wyoming Province (WP), Wyoming Basin (WB), Cheyenne Belt (CB), Rio Grande Rift (RGR), Trans-Hudson Orogen (THO), Great Plains (GP), Anadarko Basin (AB), Llano Uplift (LIU), Ouachita-Marathon Front (OMF), Central Lowlands (CL), Ozark Plateau (OzP), and Ouchita Province (OuP).

portion of DNA13, the Generalized Radon Transform [Bostock et al., 2001] is used to rotate the instrument corrected ground velocity from the vertical, east, and north coordinate frame into the P-SV-SH coordinate frame (Fig. 3.2) utilizing the slowness parameter computed for the IASP91 [Kennett and Engdahl, 1991] model via the TauP toolkit [Crotwell et al., 1999]. Arrival time windows are picked for the direct P, SV, and SH arrivals and the relative delay times are refined with the VanDecar and Crosson [1990] multi-channel cross-correlation method in period bands appropriate for the phase. The P-velocity model uses the 1.25-2.5 seconds period band, while the SV and SH models use the 10-50 seconds band. The sensitivities of the delays are then computed with the finite frequency kernels of Hung et al. [2000] and the body wave models are computed via an LSQR inverse problem solver.

The waveform data for this model is available at the IRIS DMC through the use of the FetchBulkData script. For the body wave arrivals, the event timing and location data are available from the NEIC earthquake catalog. Events between magnitude 5.5 and 8.0 are used when at least 3 stations are available between 30° and 80° from the event epicenter. The distribution of events analyzed is chosen to maximize the coverage without oversampling due to the use of many events from a highly active region. This is accomplished by considering the global distribution of events and requesting at most two events per 3° by 3° bin. In order to account for the variable coverage of the Transportable Array, the data is spatially sorted and requested at multiple times during the USArray experiment.

The cross-correlated delay times are culled, keeping only delays with a minimum average correlation coefficient of 0.9 and maximum standard deviation of 0.02 seconds. DNA13-P contains 76,322 P observations from 462 events and 2,284 stations; DNA13-SH contains 91,997 SH observations from 397 events and 2,274 stations; DNA13-SV contains 62,231 SV observations from 351 events and 2,246 stations. The P-velocity model observations are bolstered by 3,283 P-wave measurements on the Z component and the SV and SH models contain 292 tangential component S-wave measurements focused on the Yellowstone hotspot [Waite et al., 2006]. Station and event coverage is shown in figure 3.3 with the color scale representing the static corrections to the inversion described below.

In addition to the P, SV, and SH body wave only models, the joint body wave-surface wave inversion method of Obrebski et al. [2011] is used to invert Rayleigh wave phase velocities with the SV body-wave delay times to form the DNA13-SV-Joint model. This includes constraints from an updated dataset of phase velocities from Pollitz and Snoke [2010], who use local fits to teleseismic earthquakes, and also an expanded ambient seismic noise dataset from the previous chapter. Together, these two datasets span the 8-125 seconds period band and provide regularly sampled phase velocity maps. To combine the datasets, both are used where they overlap, but with greater weight given to the ambient noise dataset at the shorter periods and greater weight given to the teleseismic derived dataset at the longer periods via the weighting factor q shown in the top panel of Figure 3.4. This is done to account for vari-

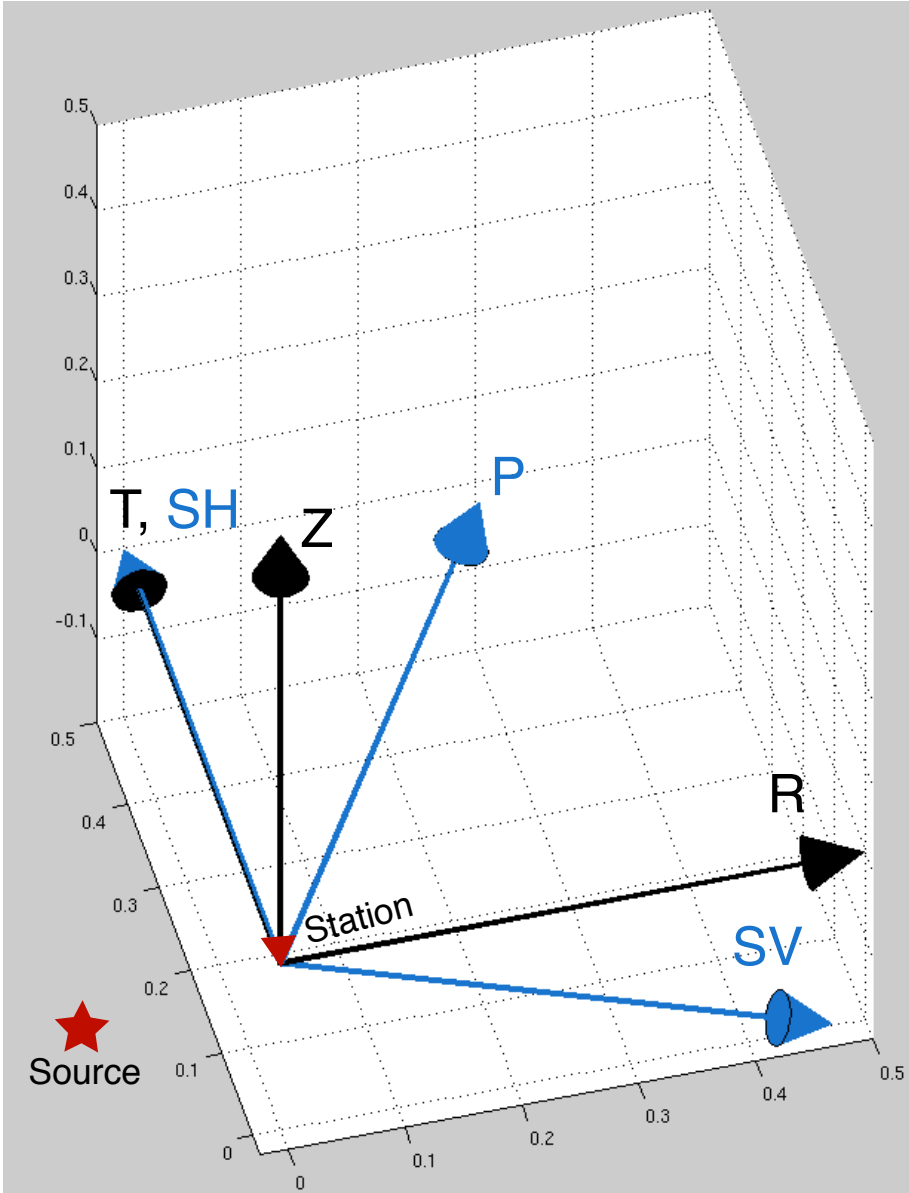


Figure 3.2: Rotation from vertical (Z), radial (R), and transverse (T) coordinate frame (black) to P-SV-SH ray centric coordinate frame (blue). The recording station is at the origin and the source is teleseismic. The star is only given to represent the relative back-azimuth to the station.

ability in the seismic source because ambient seismic noise is strongly excited in the shorter periods (8-40 seconds) whereas teleseismic earthquakes excite longer period waves (30-125 seconds). Assessment of the variation between ambient noise and earthquake derived phase velocities finds the two datasets typically agree.

The models are inverted for relative velocity perturbation on static grids without adaptive refinement. The body-wave only models have sufficient coverage from 126°W to 72°W and 25°N to 52°N with node spacing of 0.42° in both lateral directions. The vertical node spacing is set to 20 km to avoid aliasing small features. The surface wave dataset is less extensive laterally, but the improved vertical resolution allows the vertical spacing to be reduced to 10 km. The grid for the SV-Joint model is defined from 126°W to 90°W, 25°N to 52°N with spacing of 0.6° longitude by 0.45° latitude. The bottom of the models are constrained to 1280 km depth as we expect sub-transition zone anomalies to be relatively minor and crossing raypaths at greater depths are limited.

In the damped LSQR inverse solution for the models, we also solve for static station and event corrections. The station corrections account for shallow short-wavelength, and therefore unresolvable structure, beneath the stations; the event corrections accommodate errors in the timing and location of events as well as common structure out of the model space. In order to solve for the SV-Joint inversion we first convert the phase velocity observations to perturbations to the 1D WUS model of Pollitz and Snoke [2010] with a correction for the crustal thickness from CRUST2.0 [Chulick and Mooney, 2002]. Second, a weighting parameter, p , must be determined for the relative weight of the body wave delays versus the phase velocity perturbations. This parameter is defined from 0 to 1 with a value of 0 indicating the surface wave only model and a value of 1 for the body wave only model. We use a weight of 0.7 based on the trade-off analysis of Obrebski et al. [2011]. Finally, a linear ramp in the sensitivity of the travel time delays to the velocity structure in the upper 60km is imposed with zero weight at the surface and a weight of 1 at 60 km depth. This is to reduce the influence of the body waves on shallow velocity structure where the rays do not cross and provide little sensitivity. Electronic data files of the final velocity models are available in the online supplementary material.

3.3 Resolution

The surface wave inversion is a two-step procedure, and thus resolution must be addressed at both steps. The resolution of the ambient noise alone is shown in Figure 3.5. This is a resolution estimate from the method of Barmin et al. [2001], which approximates the resolvable wavelength of a delta function as a spatial map. This is shown at two periods representing the shorter periods well recovered by ambient noise and the longer periods less

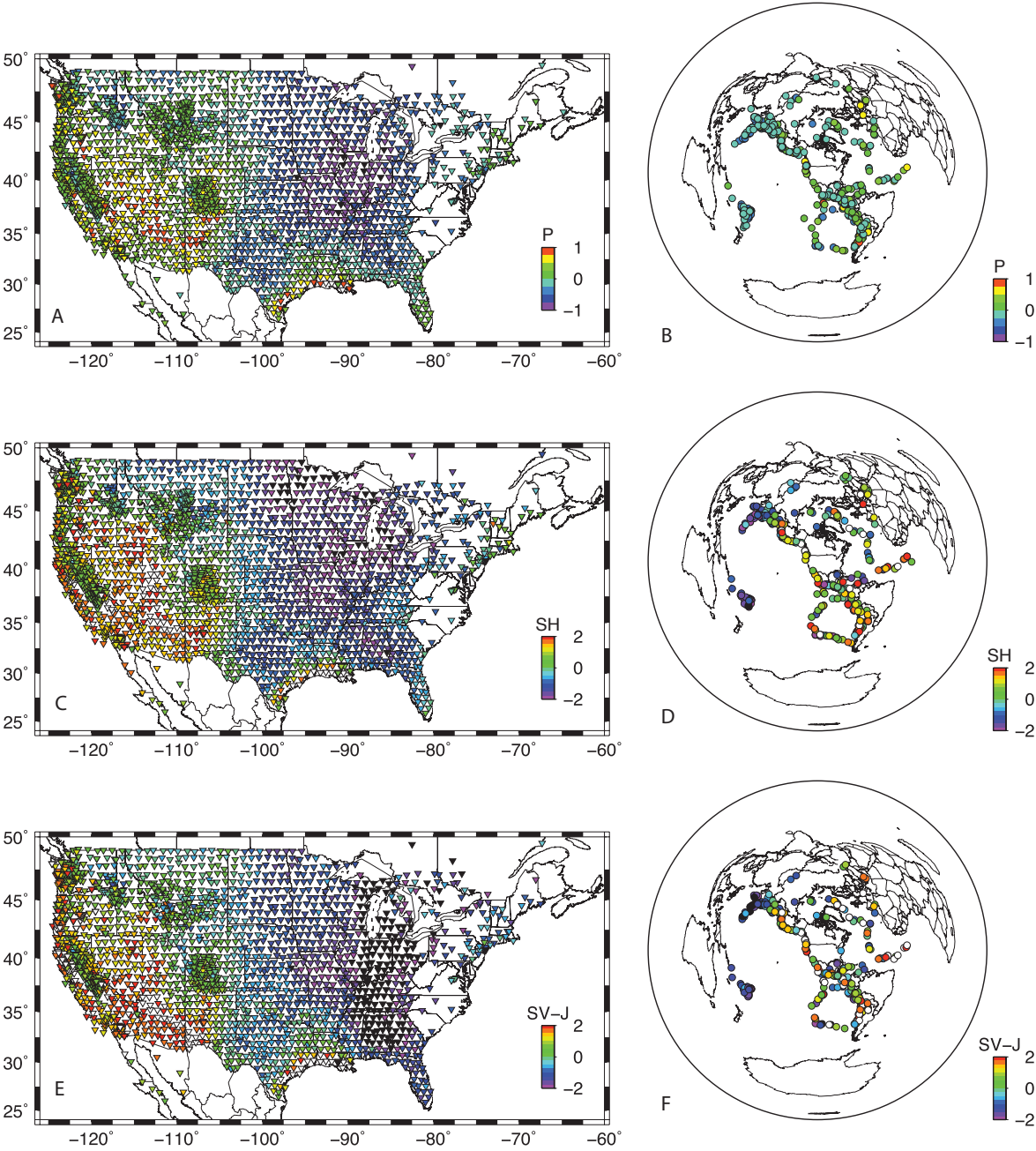


Figure 3.3: Station correction and event correction terms for the P model (A,B), SH model (C,D), and SV-Joint model (E,F). All color scales given in seconds.

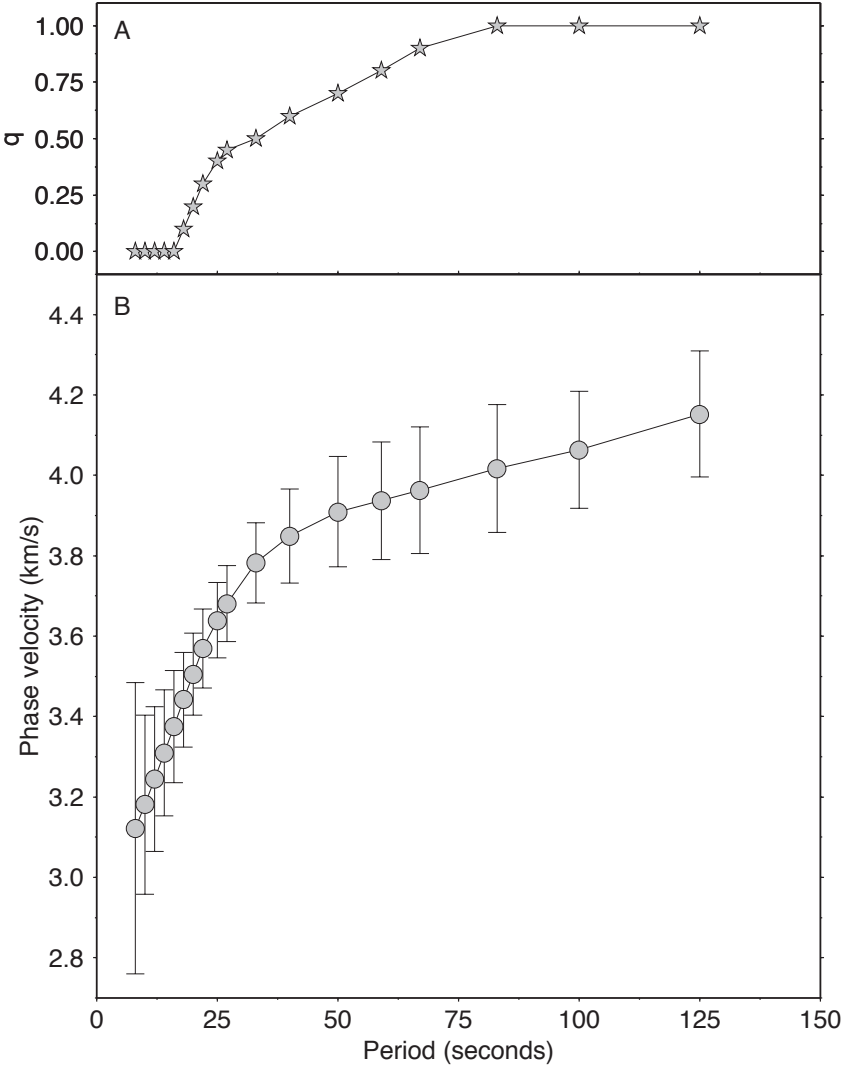


Figure 3.4: (A) Weighting parameter (q) between the ambient noise phase velocities and teleseismic phase velocities. (B) Average phase velocity in the study region and ± 1 standard deviation

well recovered by noise alone.

The resolution of the body wave models and the SV-Joint model is determined through the standard checkerboard resolution test. Progressively smaller checkers are employed to determine the range of recoverable anomaly wavelengths. Figure 3.6 illustrates the checkerboard resolution of the P, SH, and SV body wave only models and figure 3.7 displays the SV-Joint model. The tests show slightly better recovery of the P model relative to the SH model at 200 km (note the different cell sizes that are being recovered in Figure 3.6), likely due to the smaller sensitivity kernel of the higher frequency P-waves. It is also notable that the P-wave model at 200 km shows better amplitude recovery around Yellowstone and southern California due to the increased station coverage of these regions. The deeper portions of the model require larger checkers for acceptable recovery, and all the features interpreted below are the size of these recovered blocks or larger. The SV-Joint model has similar recovery to the SV model in the transition zone, but the shallow recovery (<200 km) is much improved due to the inclusion of surface waves (Fig. 3.7, 3.8, and 3.9).

3.4 Validation

An important aspect of seismological models is the ability to predict independent observations. Checkerboard tests are able to assess the resolving power of the inversion matrix, but they are unable to address the accuracy of the input data. Therefore, we determine the predictive power of the model by measuring the arrival times of a set of teleseismic events not used in DNA13 and comparing those measurements with the expected arrival times based on DNA13. We present the results as probability density functions in figure 3.10 and summarize with the correlation coefficient, R . The probability density functions display the relative probability of occurrence between observed and predicted delays. The correlation coefficient is determined as the covariance between the observed and predicted delays divided by the product of the variance of the observed delays and the variance of the predicted delays. A correlation coefficient of 1 indicates a linear relationship such that the observed delays are perfectly predicted by the model.

We perform the test for three different datasets. First, we compare the data used in the inversion to delay times predicted by the model (Fig. 3.10 A-D). We calculate these delay times by solving the forward problem using the finite frequency sensitivity matrix and the velocity model. This provides an estimate of the expected data fit. We next compare the observed and predicted delays for a set of events not used in the inversion. As shown by the probability density functions and correlation coefficients (Fig. 3.10 E-H), these predicted delay times are fit nearly as well as the data used in the inversion. This suggests these delays are well predicted by the DNA13 model. Finally, we measure arrival times from

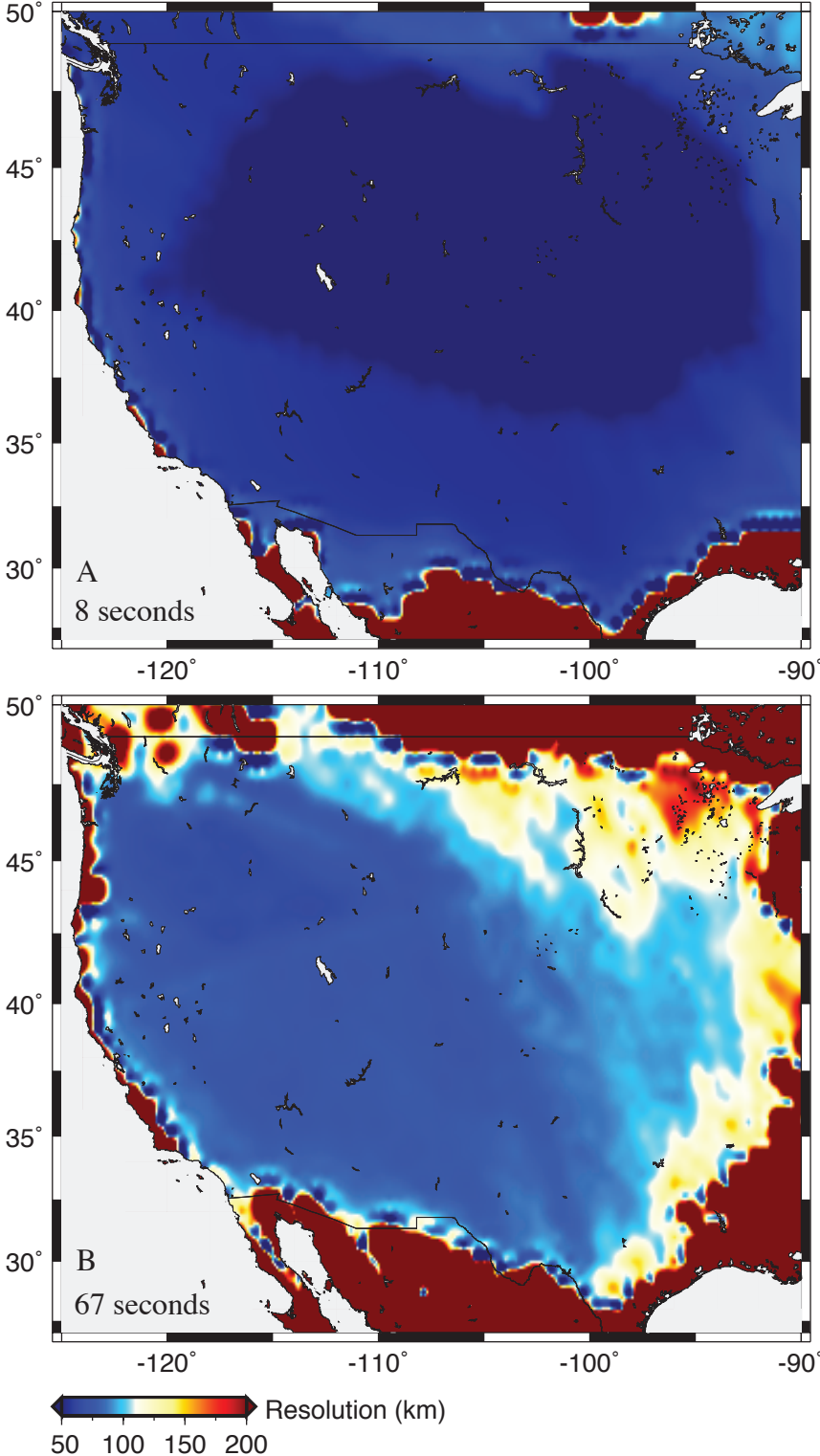


Figure 3.5: Metric of inversion resolution for ambient noise at (A) 8-second period and (B) 67-second period. Values depict the minimum wavelength that could be recovered with the ambient noise dataset at the two periods.

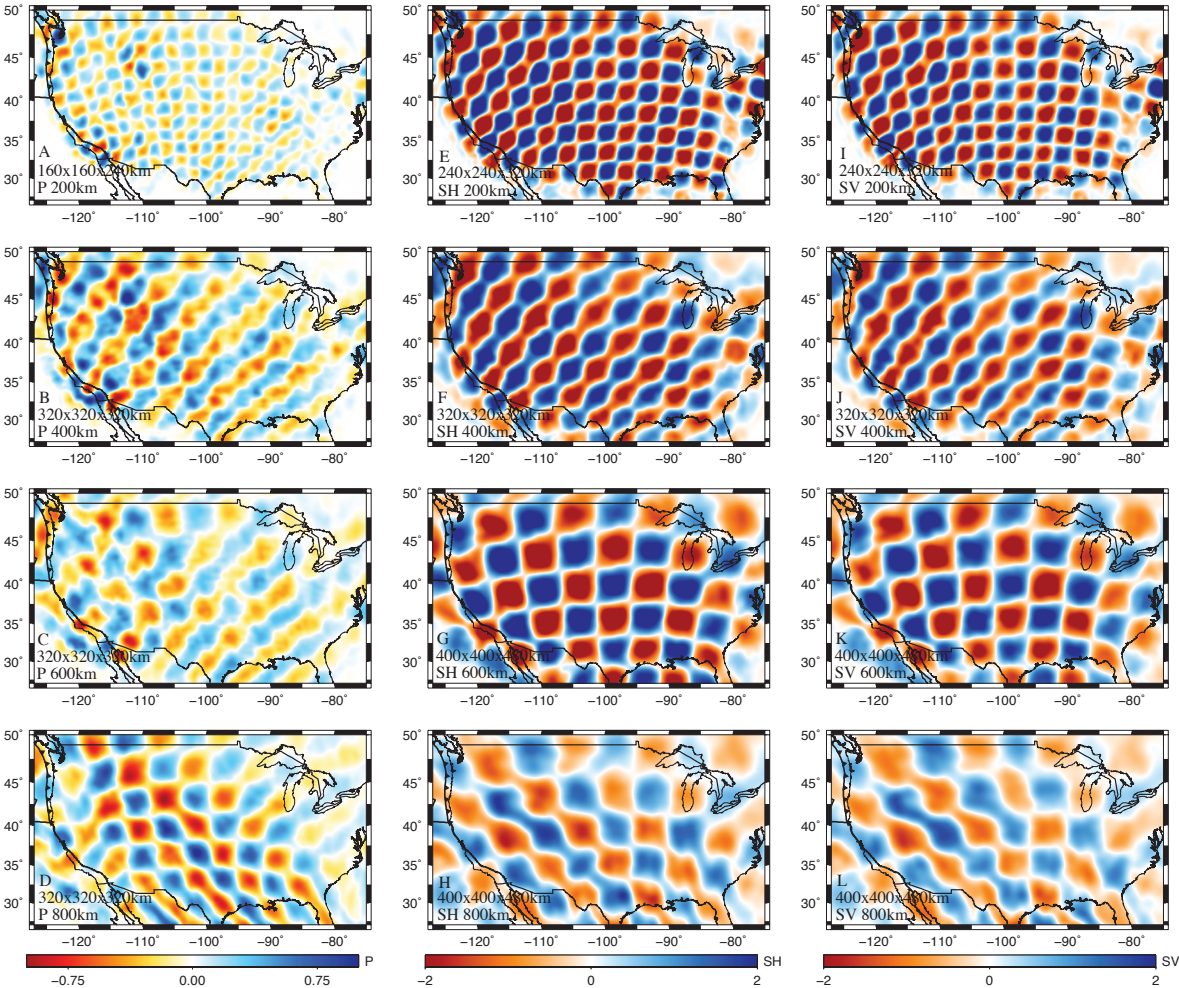


Figure 3.6: Checkerboard resolution tests for the DNA13 body wave only models. Model phase, depth of slice, and size of checkers annotated in lower left of each panel.

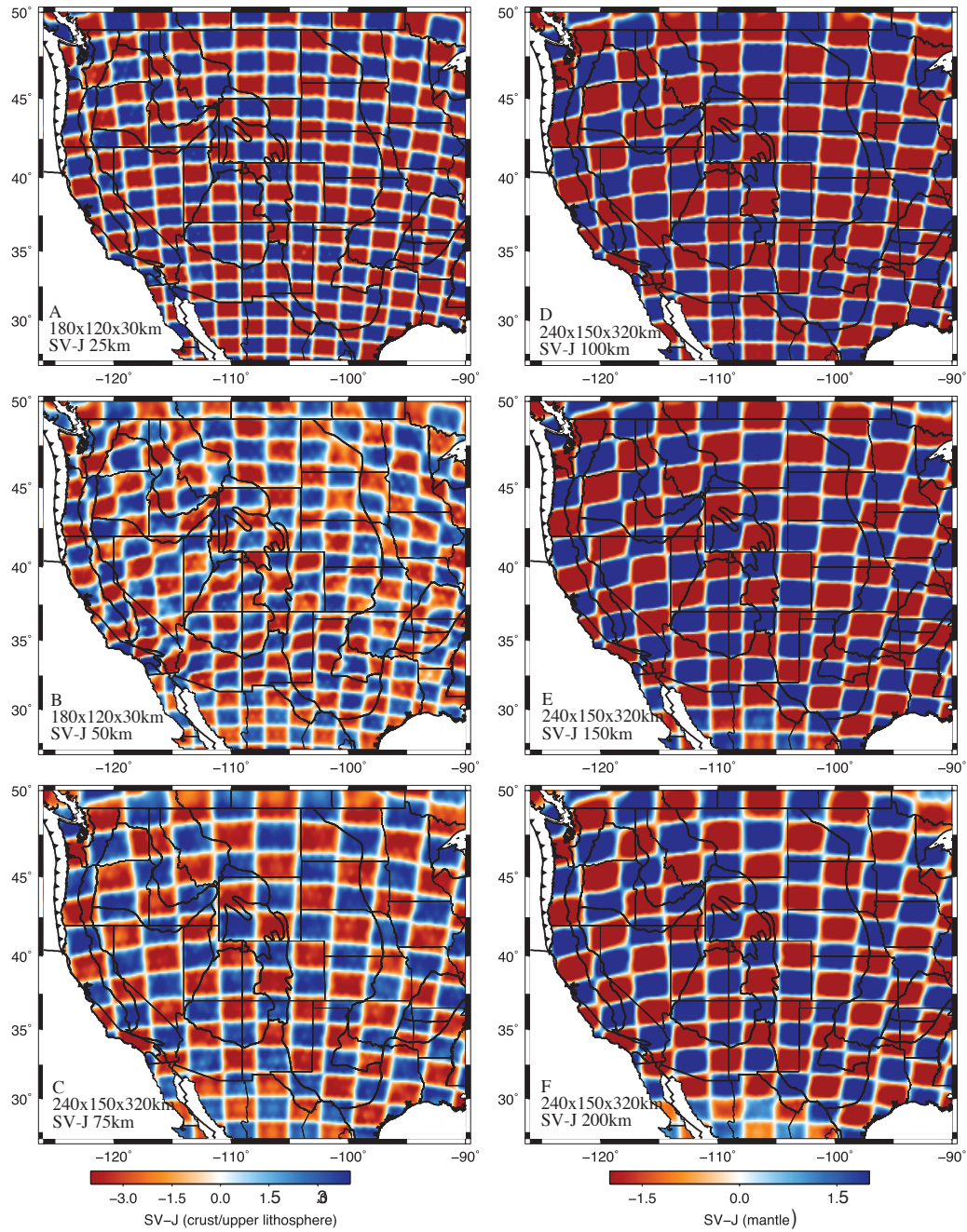


Figure 3.7: Checkerboard resolution tests for the DNA13-SV-Joint model. Depth of slice and size of checkers annotated in lower left of each panel.

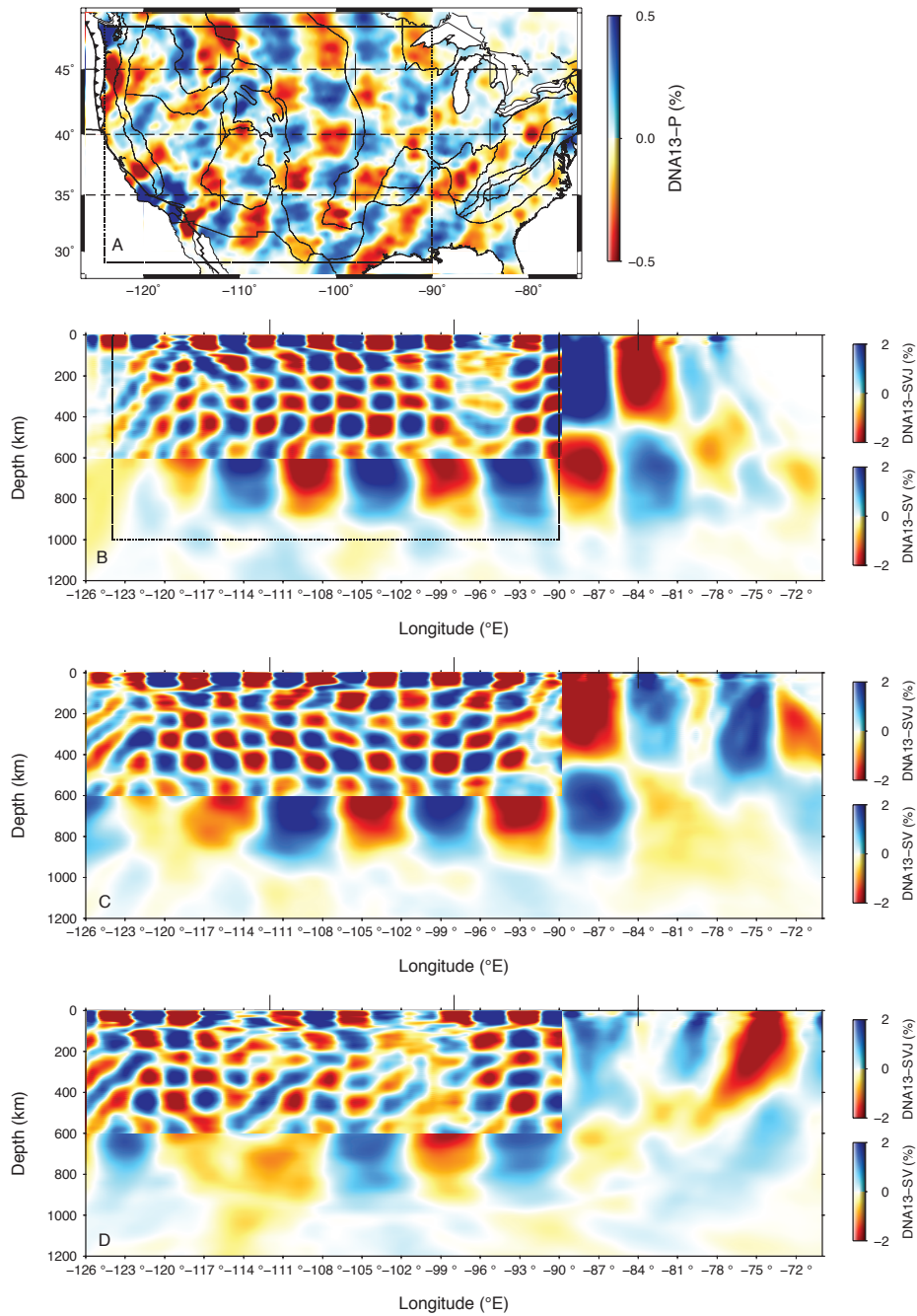


Figure 3.8: Checkerboard resolution tests for the DNA13 P, SV, and SV-Joint models. (A) Slice through P resolution test at 700km. Dashed lines give location of profiles in panels B-D. Solid box indicates the region of high resolution in the SV-Joint model. (B-D) Slices of constant latitude through the SV-Joint and SV models. Small checkers are from the SV-Joint model above 600 km and the large checkers are from the SV body wave only model. Solid box in (B) gives region of high confidence in the model and thus the region focused on in the discussion.

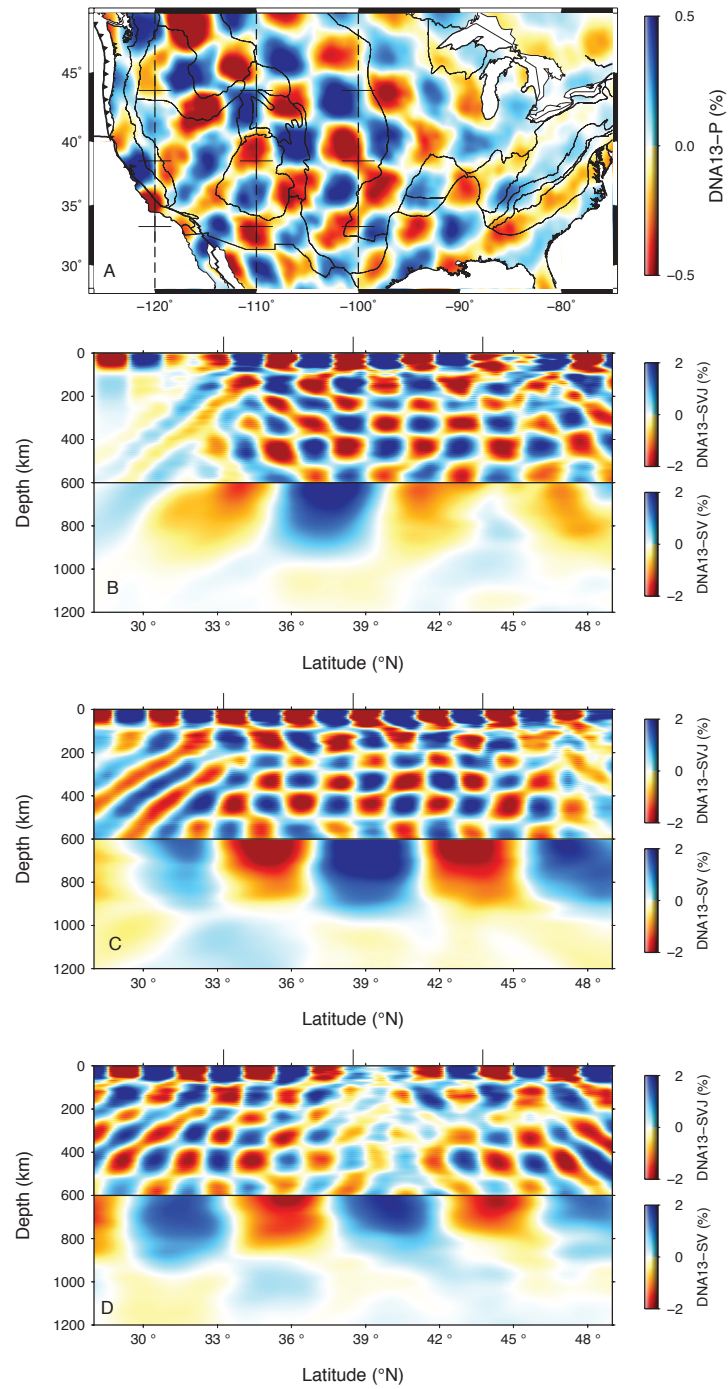


Figure 3.9: Same as figure 3.8, but for constant longitude sections.

synthetic waveforms computed with the Spectral Element Method (SEM) through the 3D Global model S362ANI and CRUST2.0 [Chulick and Mooney, 2002; Kustowski et al., 2008; Tromp et al., 2010]. These synthetics are now available through IRIS for a limited set of events. The fit of the SH and SV delays from this model are not as good as DNA13, but still show a positive correlation indicating a moderate fit. The poor fit of the P delays is likely due to the high frequency of the P observation (~ 1 Hz) relative to the maximum computed frequency in the SEM synthetics (~ 0.06 Hz).

3.5 Results

3.5.1 Upper 200 km structures

The upper 200 km of the model encompasses the crust, thin Phanerozoic lithosphere, most of the cratonic lithosphere, and a portion of the western U.S. asthenosphere and is best represented by the SV-Joint model in figure 3.11. These maps show the marked contrast between the slow western U.S. and fast eastern U.S. throughout the upper 200 km. The shallowest map displayed, at 25 km, depicts mostly mid to lower crustal structure with pockets of upper mantle lithosphere in central California (CC) and the California-Arizona (SC) border. The crust east of the Rocky Mountain Front is largely high velocity, with the notable low velocity crescent along the Gulf Coast (GC) of Texas and Louisiana. High velocities in the western U.S. crust are primarily located in the Colorado Plateau (CP) and Columbia River Basalts (CRB) regions.

At sub-crustal depths, three high velocity features begin to emerge. First, the Juan de Fuca plate (JdF) is a north-south oriented high velocity feature most noticeable below 100 km depth. This plate is only slightly high velocity, which may be due to a relatively weak contrast with the lower cratonic lithosphere to the east. The second high velocity feature is the Colorado Plateau. In this region, the central high velocity of the lower crust disappears in the upper lithosphere and is replaced by two high velocity bodies at the northwest and southeast edges. These features have previously been interpreted as lithospheric drips [Liu et al., 2011; Obrebski et al., 2011] and this model is consistent with that interpretation. The last features we note are the Isabella Anomaly (IA) [Frassetto et al., 2011; Zandt et al., 2004] and Transverse Range Anomaly (TR) [Wang et al., 2013] in southern California. These features are high velocity bodies in regions of slightly thicker crust than the surrounding and have been argued to be either plate fragments or lithospheric instabilities [Frassetto et al., 2011; Pikser et al., 2012; Wang et al., 2013; Zandt et al., 2004].

Low velocities are mostly observed in the western U.S. and a few of these are exceptionally high amplitude slow features. First, the Yellowstone (YS) hotspot track is observed

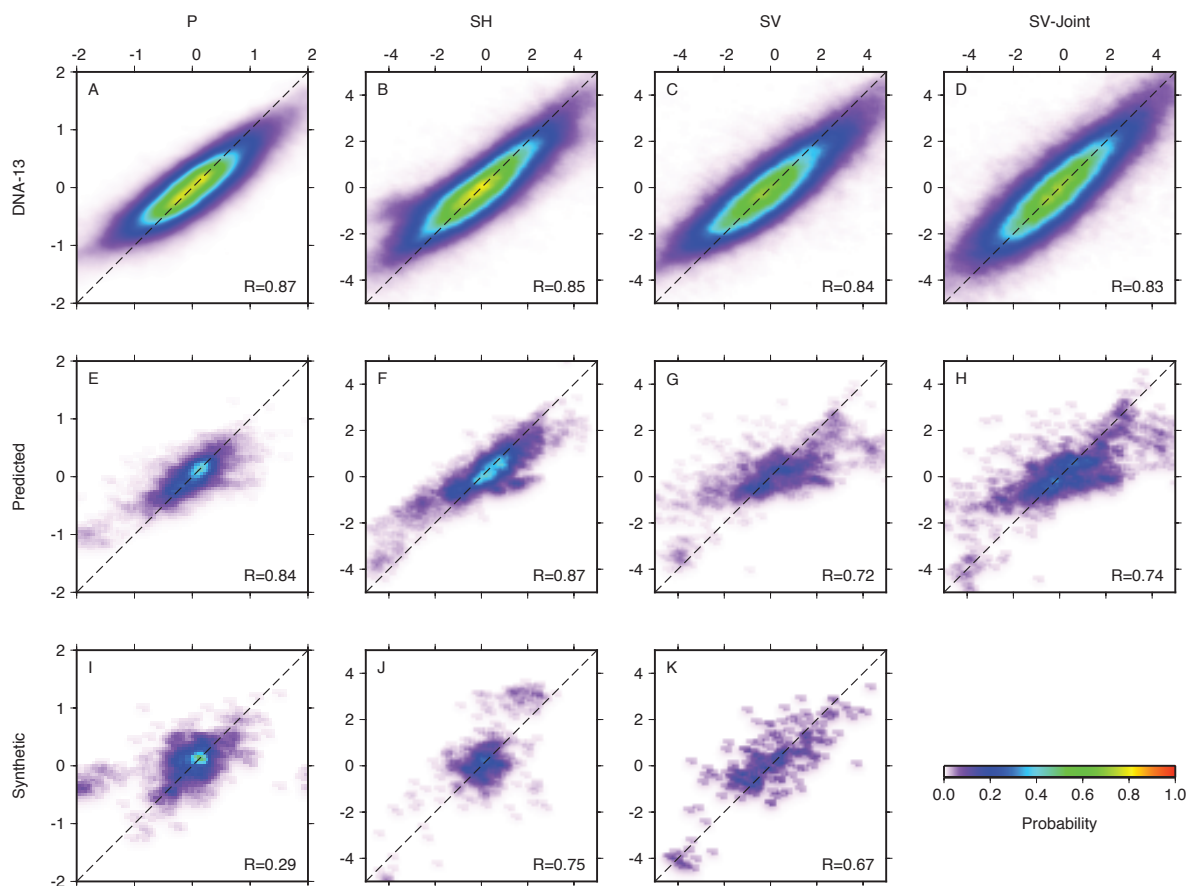


Figure 3.10: Results of the predictive power test. The x-axis of each panel is the observed delay time and the y-axis is the predicted delay time. Top row (A-D) is for the delays used in the generation of DNA13. Center row (E-H) displays the predicted delays through DNA13 and the bottom row is the predicted delays from the global model. Dashed line is the 1:1 line indicating a perfectly predicted delay time. Correlation coefficient, R , for the given test are displayed in the bottom right of each panel.

as very low velocity along the northeast end of the Snake River Plain (SRP) throughout the upper 200 km. In the crust and upper mantle, the Yellowstone hotspot has a relatively broad parabolic shape, which tightens to a thinner parabola at 100-200 km depths. Other low velocity features tend to focus along province boundaries such as around the Colorado Plateau and eastern Sierra Nevada [Obrebski et al., 2011]. One other notable feature from 75-200 km depth is a gradational west to east increase in velocity towards the center of the Laurentia craton (LC). The high velocity continent starts along the eastern margin of the Rocky Mountain Front and grades to higher velocities across the Great Plains to the Central Lowlands.

3.5.2 Deeper structures

The broad east-west contrast is also seen in the deeper images. The body-wave models illustrate this in figure 3.12 with maps at 200, 400, 600, and 800 km depths. The western U.S. is primarily slow with interspersed high velocity anomalies. This image also allows tracing of the Yellowstone plume from the sub-lithospheric plume head to a broad upwelling at 800km (YS). The eastern U.S. is largely high velocity with notable anomalies in Texas (L1), Nebraska (F1), and Tennessee (F2). The high velocity anomaly in Texas extends to 600 km depth and weakens to the northeast. The low velocity under eastern Colorado and Oklahoma demarcates the Texas anomaly from the main high velocity body of the eastern U.S. Within the main high velocity body of the eastern U.S., the F1 and F2 anomalies are unusually high velocity features. Body-waves are unable to uniquely determine the depth extent of these features, but the pervasiveness of the features on all components suggests a robust observation of a high velocity anomaly within the Farallon plate.

The DNA13 model compares very well with other regional seismic velocity models. In figure 3.13 we display the DNA13 SV-Joint and SH models at 200 km and provide images from Yuan et al. [2011] and Nettles and Dziewoński [2008] at the same depth. These models all show a consistent east-west contrast between the slow western U.S. and the fast eastern U.S. at 200 km. They also display a transitional zone across the Rocky Mountain Front where the velocity increases towards the center of the Laurentia Craton. However, we note the significantly increased detail of DNA13 in the western U.S. where the high lateral resolution of body waves is able to recover the Juan de Fuca slab missing from the other models. However, DNA13 shows smaller velocity anomalies than the surface wave derived models, which is likely an effect of damping in the inversion.

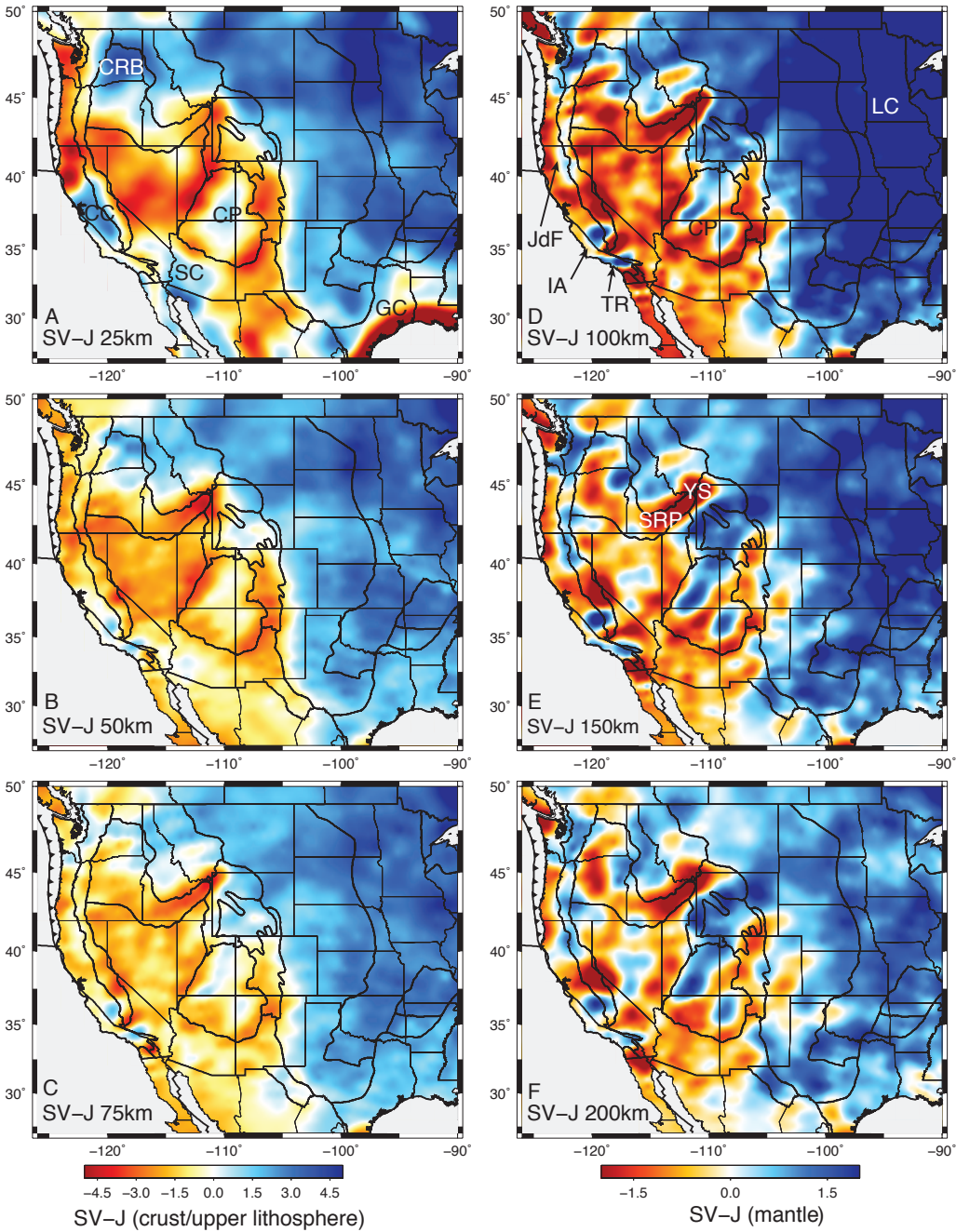


Figure 3.11: Shallow structure computed for the SV-Joint model. Map depths for A-F given in lower left hand corner. Annotations are given for the Columbia River Basalts (CRB), Central California (CC), Southern California (SC), Colorado Plateau (CP), Gulf Coast (GC), Juan de Fuca Slab (JdF), Isabella Anomaly (IA), Transverse Range (TR), Yellowstone (YS), Snake River Plain (SRP), and Laurentia Craton (LC).

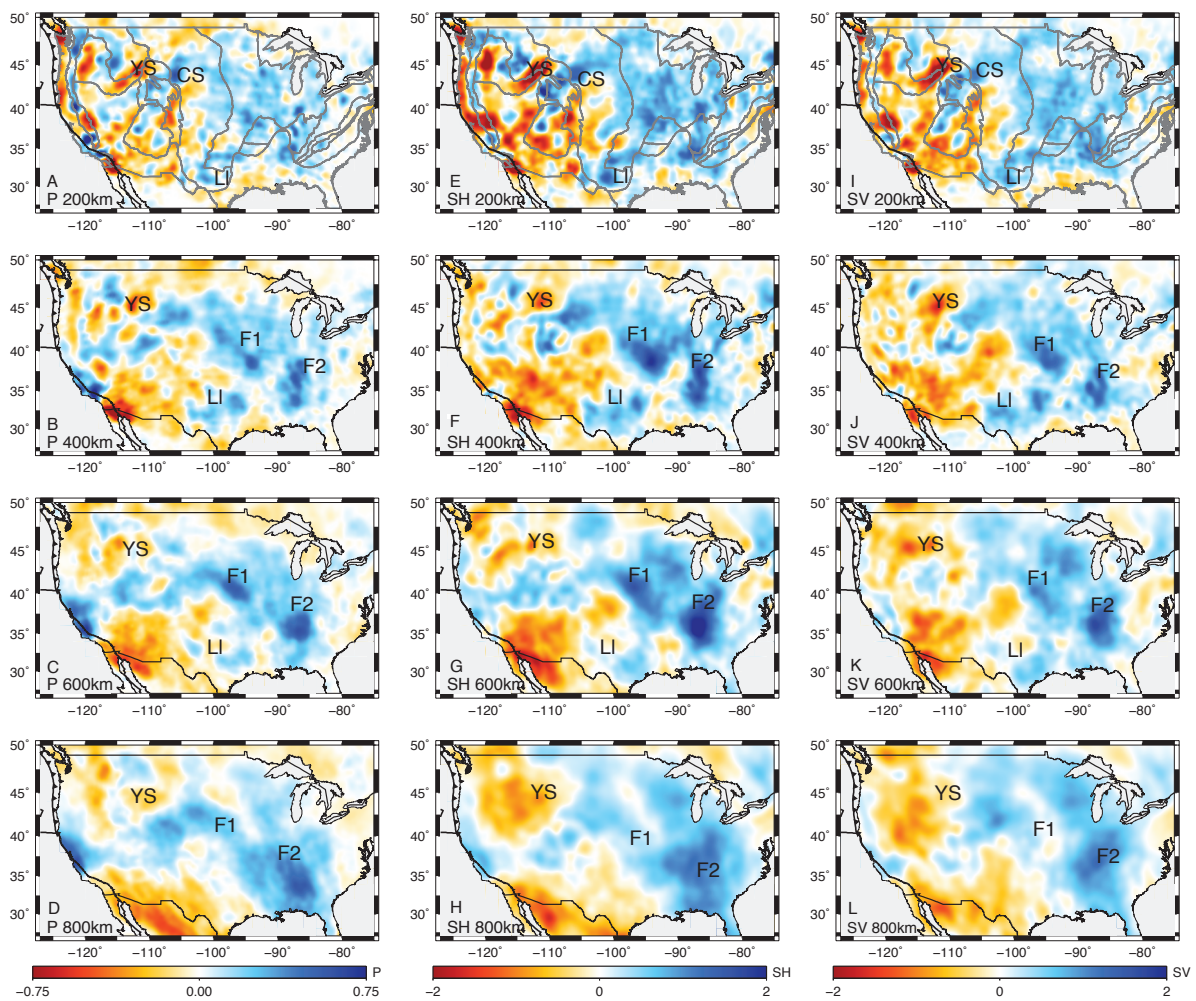


Figure 3.12: Mantle maps for the 3 body-wave only component models. Phase and depth are given in lower left corner. Annotations given for the Yellowstone hotspot (YS), Llano Province (LI), Cheyenne Slab (CS), and Deep Farallon 1 and 2 (F1, F2).

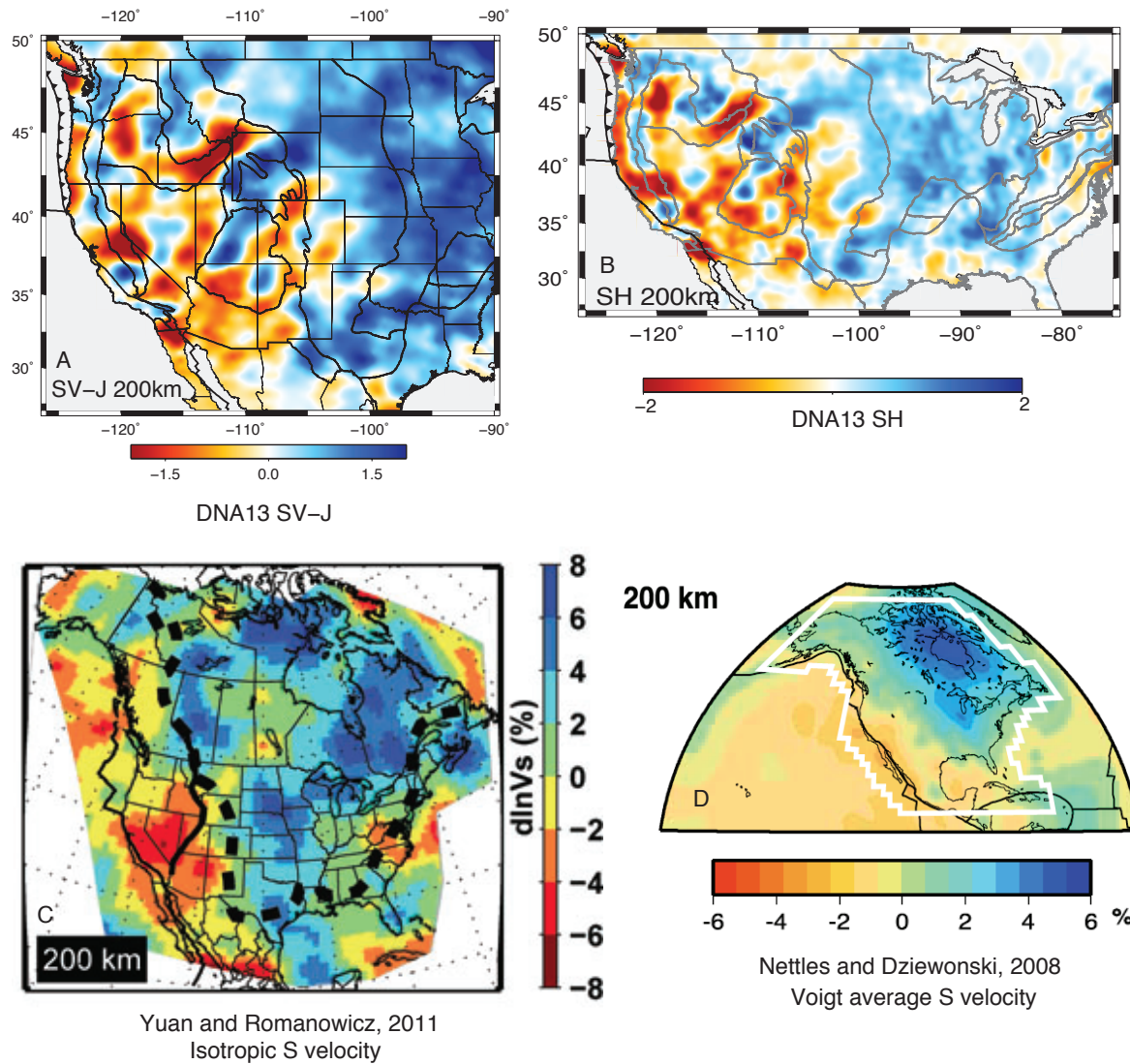


Figure 3.13: Comparison of DNA13 at 200km depth with other regional models: (A) DNA13 SV-Joint, (B) DNA13 SH, (C) Yuan and Romanowicz, 2011 isotropic, and (D) Nettles and Dziewonski, 2008 Voigt average.

3.6 Discussion

The progression of USArray through the Laurentia Craton is providing detailed images of the remnants of continental creation. The Archean age Wyoming Province and Mesoproterozoic Llano Province represent the early (~ 1.8 - 2.0 Ga) and late (~ 1.3 - 1.0 Ga) stages of continental accumulation. The proposed primary mechanisms of continental formation are stacking of oceanic slabs and amalgamation of volcanic arcs [Lee, 2006]. These processes leave remnant structures in the lithosphere, which we image to reconstruct the formation of the continent.

The deep structure of the model is primarily associated with the subducting Farallon plate. Fragments of this plate can be traced from the eastern U.S. to the modern Juan de Fuca system [Burdick et al., 2012; Pavlis, 2011; Sigloch, 2011]. Detailed imaging of this plate has proven difficult for two reasons. First, the station coverage of the eastern U.S. has been historically sparse. This is rapidly being overcome by USArray and is less of a factor at the time of this publication. Secondly, the simplified structure of a thick high velocity cratonic lid [Abt et al., 2010] over a high velocity slab is difficult to image with body waves alone due to the near vertical ray propagation. Our joint body-wave surface-wave inversion overcomes this limitation by partitioning the proper amount of high velocity anomaly to the near surface and thereby allowing improved imaging of high velocity in the sub-lithospheric mantle.

3.6.1 Wyoming Province

The Archean age (>2.5 Ga) Wyoming Province (WP) is depicted in figure 3.14. The map views of the model (Fig. 3.14A,B) show high velocities for the WP are contiguous with the Laurentia Craton. The lithospheric map, at 100 km depth, shows three significant low wave-speed anomalies associated with the Little Belt Arc [Whitmeyer and Karlstrom, 2007], the Yellowstone Plume [Obrebski et al., 2011], and the northern Rio Grande Rift. The Little Belt Arc and the Rio Grande Rift are at the periphery of the province, but the Yellowstone plume intrudes on the province as a low shear velocity anomaly of -3%. Cross-section A-A' (Fig. 3.14C) shows that the low velocity anomaly beneath Yellowstone is contiguous to the bottom of the model, but with significant deflection through the transition zone. Figure 3.14C also depicts high velocity features associated with the cratonic lithosphere. The Cheyenne Slab [Yuan and Dueker, 2005] is shown as the southern margin of the Wyoming Province. Cross-section A-A' (Fig. 3.14C) only shows a northward dipping southern edge to the high velocity lithosphere and does not differentiate the Cheyenne Slab from the Wyoming Province as clearly as Yuan and Dueker [2005]. However, the cross-section B-B' (Fig. 3.14D) does show a thickened high velocity anomaly with an indication of a northward dip at the eastern end of the Cheyenne Slab. Yuan and Dueker [2005] suggest the northward dip of

the Cheyenne Slab reflects a reversal of subduction polarity after back-arc closure in the Proterozoic. North of the Yellowstone Plume we image a high velocity body with similar dip and amplitude as the Cheyenne Slab, which we label the Little Belt Slab. This fossil slab is associated with the suture of the Wyoming Province with the Medicine Hat Block. The impingement of the Yellowstone plume on this fossil slab may be focusing along the old plate interface leading to the observed low velocity of the Little Belt Arc. To the east, Figure 3.14D shows the Wyoming Province is largely intact with a low velocity zone along the southern margin associated with the northern Rio Grande Rift.

3.6.2 Llano Province

The Llano Province (LIU) in Texas is shown in figure 3.15. The map at 15 km (Fig. 3.15A) shows a primarily high velocity region with low velocities near the Gulf Coast east of the Ouachita-Marathon Front (OMF). Other low velocity anomalies in the crust are associated with the Anadarko Basin (AB) and the southern Rio Grande Rift. Immediately west of the Ouachita-Marathon Front in Central Texas, the Llano Uplift (LIU - Fig. 3.1) appears as an increased high velocity anomaly. This feature represents collision of a long-lived (~ 50 m.y.) arc being accreted to the southern margin of the Laurentia Craton (LC) from 1150-1120 Ma [Mosher, 1998].

The lower lithosphere structure presents the root of these anomalies (Fig. 3.15C). Low velocities are more prevalent and are primarily focused in the northwest and southeast of the region. The anomaly under the Anadarko Basin broadens and separates the lower portion of the Llano Province from the Laurentia Craton. The Llano Province consists of an irregular high velocity body, which we suggest is the Llano Slab (LIS). This slab is associated with the northeast and southwest closure events during the Mesoproterozoic. Figure 3.15C highlights the southwest portion of the Llano Slab as dipping to the north towards the Southern Oklahoma Aulacogen (SOA) and Laurentia Craton.

Cross-section D-D' in figure 3.15D depicts the structure to the southeast of the Llano Uplift. This shows gradationally thicker lithosphere towards the north and a high velocity body in the mantle transition zone. Based on scattered waveform imaging by Pavlis [2011] showing contiguity of this feature to the northeast, we interpret this to be the southeastern portion of the Farallon plate (FS). While most of the Farallon plate imaged under the western U.S. was north of the migrating Mendocino Triple Junction, this southern portion is associated with subduction south of the Rivera Triple Junction. Sigloch and Mihalynuk [2013] present a similar interpretation based on deeper mantle tomography. The relation of the Llano Slab and southern Farallon slab is depicted in cross-section E-E' (Fig. 3.15E) showing a resolvable separation is observed.

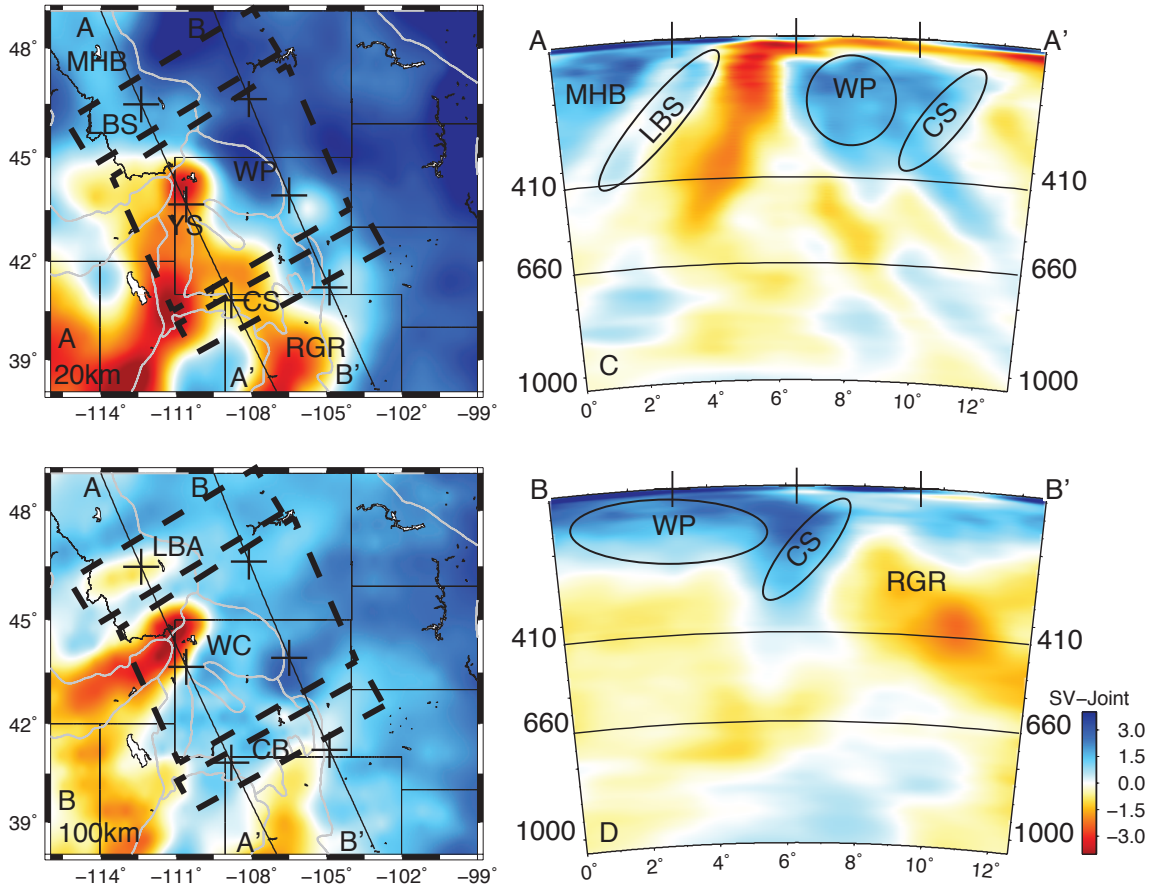


Figure 3.14: Maps and cross sections summarizing the Wyoming Province: see figure 3.1 for location. Maps are given at (A) 20 km and (B) 100 km. Locations of profiles A-A' and B-B' are given on the maps and dashed boxes outline the approximate Little Belt Arc (LBA), Wyoming Craton (WC), and Cheyenne Belt (CB). Annotations: Medicine Hat Block (MHB), Little Belt Slab (LBS), Yellowstone (YS), Wyoming Province (WP), Cheyenne Slab (CS), Rio Grande Rift (RGR), Laurentia Craton (LC). Ovals depict approximate locations on the cross-sections.

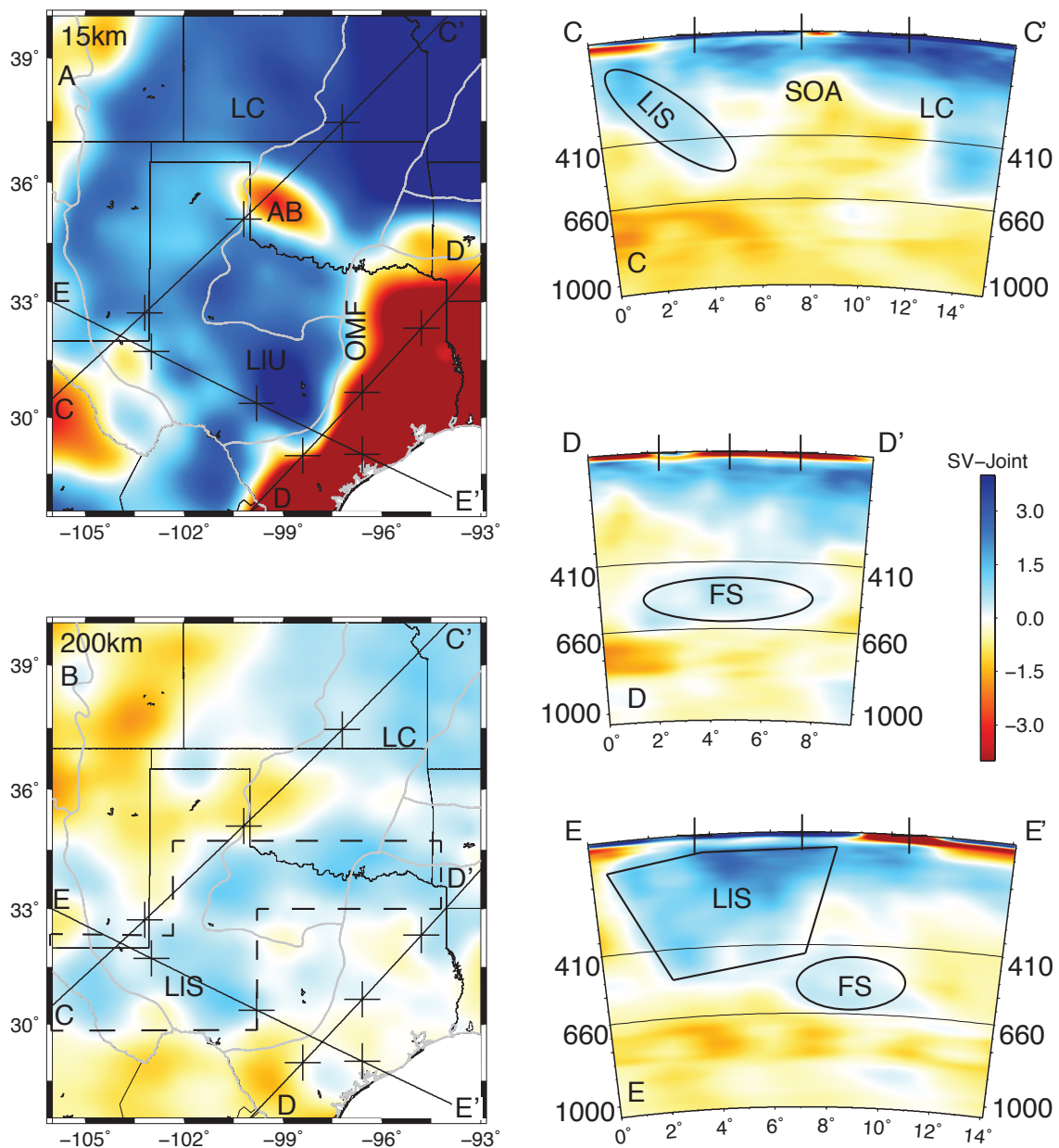


Figure 3.15: Structure of the Llano Province: see figure 3.1 for location reference. Maps depict structure at (A) 15 km and (B) 200 km. Also shown are the locations of profiles C-C', D-D', and E-E'. The dashed box on the 200 km slice outlines the interpreted areal extent of the Llano Slab. Ovals and boxes on cross-sections give approximate slab boundaries. Annotations: Laurentia Craton (LC), Anadarko Basin (AB), Ouachita-Marathon Front (OMF), Llano Uplift (LIU), Llano Slab (LIS), Southern Oklahoma Aulacogen (SOA), and Farallon Slab (FS).

3.6.3 Comparison of craton constituents

The above discussion has focused on two Proterozoic provinces independently. These two provinces have several important similarities. First, we are able to identify constituent fossil slabs along some paleo-margins. The Cheyenne slab and Little Belt Slab form the southern and northern province boundaries for the Wyoming Province while the Llano Slab is at the southern boundary of the Llano province. The Cheyenne Slab and Llano Slab are associated with subduction polarity reversal as back-arc basins closed. Additionally, lithospheric low velocities are associated with preserved suture zones such as the Little Belt Arc and Southern Oklahoma Aulacogen. Based on the tectonic history of the Southern Oklahoma Aulacogen [Keller and Stephenson, 2007; Soreghan et al., 2012], we suggest this is evidence of paleo-suture zones localizing deformation.

We further note some significant differences between the two provinces. The Wyoming Province had its primary orogeny to the east, via the Trans-Hudson Orogen, and no signal is seen in this suture zone: the Archean proto-continent shows no distinguishable structure relative to the eastern Laurentia Craton. However, the Llano Province has a significant zone of thinned lithosphere demarcating it from the Laurentia Craton. This is either due to variations in age of the provinces (2.0 Ga vs. 1.0 Ga) or subsequent deformation along the Southern Oklahoma Aulacogen. Additionally, in this model the Cheyenne Slab is not distinct from the Wyoming Province, but the dipping Llano Slab is a much thicker high velocity feature than the base of the Llano lithosphere. This suggests a significant rheological difference between the slabs, which may be due a combination of cooling, ambient mantle conditions at time of formation, age at time of accretion, or post-accretion deformation.

3.6.4 Deep Farallon Structure

The main feature in the model below the cratonic lithosphere is the Farallon slab. Deviations from the expected homogeneous planar structure of this feature include two high velocity anomalies (F1, F2, Fig. 3.16A) and significant topography of the slab surface under the Central Lowlands (CL) and Ozark Plateau (OzP) as imaged in the SV-Joint model. These anomalies may either be due to heterogeneities within the plate before it reached the trench, or they may have formed during subduction due to a combination of geometrical forcing and mineralogical phase transitions. Possible heterogeneities in the plate arise from plume-ridge interaction similar to Iceland and the Shatsky Rise [Liu et al., 2010]. In this scenario, a buoyant mantle plume intersects a paleo-ridge and is currently observed as the shallow portion of the Farallon slab at ~ 500 km depth (Fig. 3.16B, anomaly EF). The highest velocities, F1 and F2, could be oceanic plateaus formed by this plume at the ridge and pushed apart as spreading continued. This thickened oceanic crust would have provided the necessary positive buoyancy to promote flat subduction and keep the slab at upper mantle

depths for a protracted period of time.

3.7 Summary

The DNA13 tomographic models illuminate the upper mantle structure beneath the contiguous U.S. These models were created by adapting a ray-centric rotation into the P-SV-SH coordinate frame to provide multiple estimates of the velocity structure. SV constraints are also provided by Rayleigh waves, which are integrated into a joint body-wave and surface-wave inversion. Assessment of the predictive power of the models shows that we are able to predict delay times of new events to a high level of accuracy giving us confidence in the modeled structure.

Significant structures in the models relate to the fossilized remains of continental formation and provide insights to subduction kinematics and continental plate formation. The Wyoming Province retains evidence of fossil slabs along its southern (Cheyenne) and northern (Little Belt) boundaries. Its western end is strongly impinged upon by the upwelling Yellowstone plume, which is focusing into paleo-suture zones. This Paleoproterozoic province has some significant differences from the Mesoproterozoic Llano Province. While both have evidence of fossil slabs, the Wyoming Province has continuity with the Laurentia Craton not evidenced in the Llano Province. This may either be due to the deformation localized along the Southern Oklahoma Aulacogen or variations in proterozoic mantle rheology.

The deep eastern end of the Farallon is imaged to be shallower than may be expected for a slab generated in the middle Mesozoic. The increased high velocity anomalies around the shallowed part of the slab suggest this is a subducted oceanic plateau formed from the intersection of a plume and a ridge. This process is analogous to modern Iceland and may provide the necessary positive bouyancy to keep the slab at a relatively flat angle. As this anomalous structure reaches the transition zone, the viscosity contrast resists the negative bouyancy forces keeping the slab shallow.

This chapter is in preparation for submission to Earth and Planetary Science Letters.

3.8 Chapter Acknowledgements

All figures were made with Generic Mapping Tools (GMT). Wed like to thank IRIS and Earthscope for the USArray dataset. Wed also like to thank UC Berkeley undergraduate Jenny Taing for helping derive arrival time measurements. We thank Shu-Huei Hung and Mathias Obrebski for continued use of software and the rest of the UC Berkeley regional

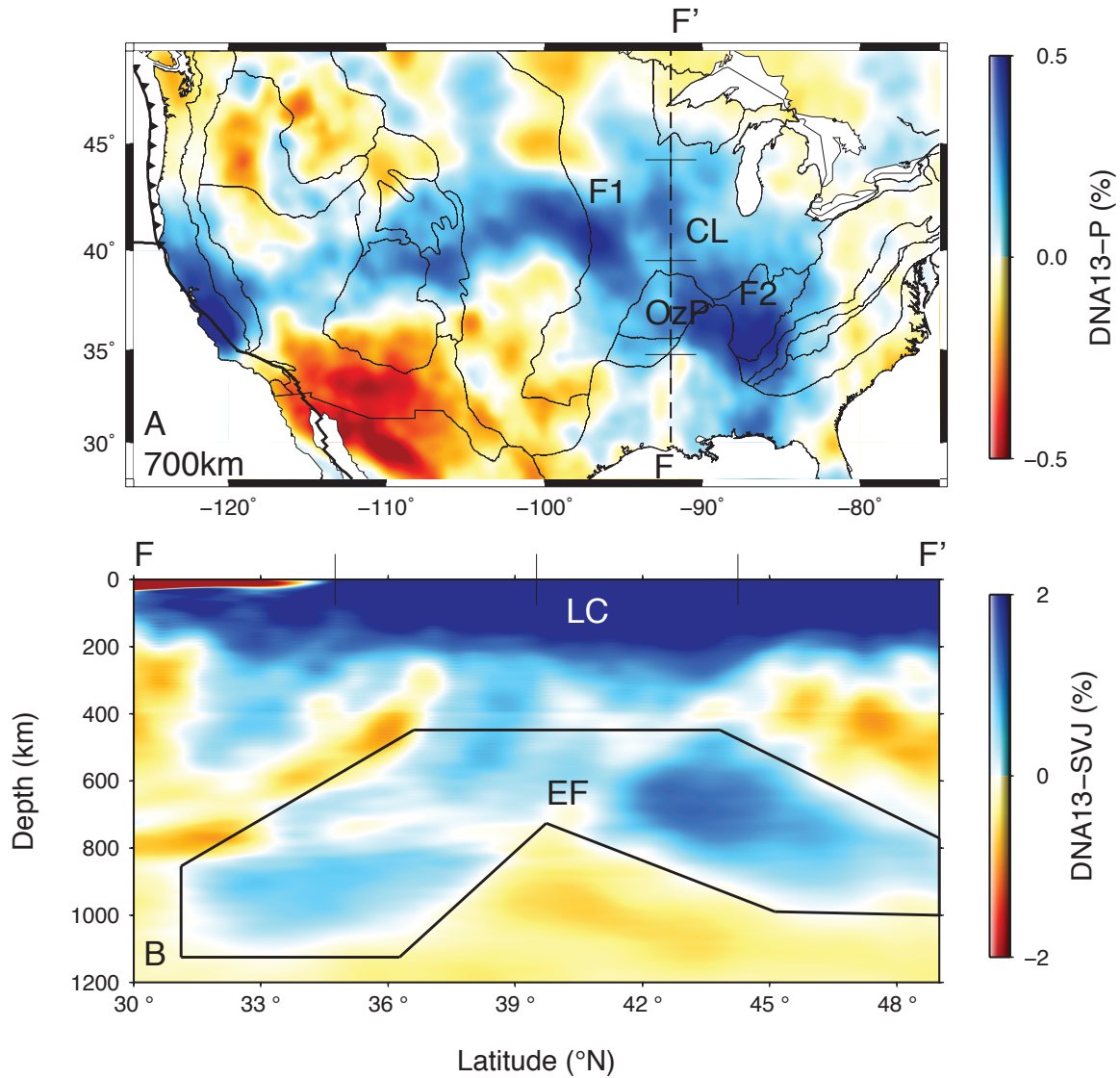


Figure 3.16: Deep structure in the DNA13 model: (a) map slice through the P model at 700km depth. (b) Longitudinal profile from south-to-north depicting the structure of the deep farallon slab. Abbreviations: Deep Farallon 1 and 2 (F1, F2), Eastern Farallon (EF), Central Lowlands (CL), Ozark Plateau (OzP), and Laurentia Craton (LC).

imaging group (Cheng Cheng, William Hawley, Qingkai Kong, and Robert Martin Short) for continuing discussion on early versions of this manuscript. This work was funded by National Science Foundation grants EAR-0643077 and EAR-0745934.

Chapter 4

Seismic evidence of remnant slabs beneath the western U.S.

Advisor: Richard M. Allen

4.1 Introduction

The USArray seismic experiment has revolutionized our ability to image the interior of the earth, providing a more detailed picture of the Earth structure below the contiguous United States. The USArrays ~ 400 broadband seismic stations deployed throughout the western U.S. collected data that helps provide highly detailed images of multiple high wave-speed anomalies in the upper mantle. Some anomalies are associated with present-day subduction of the Juan de Fuca (JdF) plate. Others are not, specifically the Siletzia Curtain Anomaly [Schmandt and Humphreys, 2011] (SCA), the Wallowa Anomaly [Darold and Humphreys, 2013] (WA), the Nevada Anomaly [Obrebski et al., 2010; West et al., 2009] (NA), and the Isabella Anomaly [Boyd et al., 2004; Frassetto et al., 2011; Jones et al., 1994; Zandt et al., 2004] (IA). These four features are markedly similar [Becker, 2012; Pavlis, 2011], which suggests a common origin, but local studies that consider the anomalies individually interpret them as having different origins. Here, we present seismologic evidence that collectively these anomalies comprise small pieces of oceanic lithosphere from the Farallon Plate system. This system of subducted plate fragments stretches over 3600km from the JdF plate off the U.S. west coast to the eastern U.S. where global models image fragments to depths of 1000km [Lebedev and Van Der Hilst, 2008]. Subduction of the Farallon plate has persisted for over 150 million years, providing an ample source of relatively cool mantle lithosphere. This proposed explanation for the observed high velocity features contrasts sharply with the alternative explanation that suggests these anomalies result from large-scale lithospheric dripping.

We use the DNA13-P tomographic model to assess the geometry and isotropic velocity of these anomalies. This model is derived using 76,322 relative delay times of direct P-waves from 483 earthquakes recorded on 2284 stations to constrain relative compressional

wave-speed in the mantle from 100km to 1000km depth. The DNA13-P model structure is similar to other seismic models derived using USArray data, [Becker, 2012; Pavlis, 2011] which suggests that differences in the dataset and method of model generation do not lead to different interpretations. Our hypothesis is primarily based on the shape and size of the models anomalies, but independent data sources including topography, shear-wave splitting, and Ps receiver functions support the remnant slab hypothesis.

4.2 Results

A broad geographic view of the DNA13-P structure shows a planar slice that dips to the east and captures many of the high-velocity anomalies, from the young, shallow western end where the JdF slab subducts today, to the deeper eastern portion of the Farallon slab (Fig. 4.1). East of Texas, the slab appears largely intact with apparent higher wave-speed anomalies beneath Alabama and Nebraska. The western high wave-speed features are markedly heterogeneous, compared to the eastern portion, indicating a discontinuous western Farallon slab. Some of these high-velocity features are seen in east-west cross-sections through the model (Fig. 4.2). A cross-section (Fig. 4.2C) that crosses the JdF plate, the WA, and the SCA shows the JdF plate to dip steeply to the east through the transition zone. The WA and SCA are located just east of the JdF plate in the shallow mantle. They appear as two parallel high velocity bodies in close proximity that extend no deeper than 500 km. A cross-section at lower latitude (Fig. 4.2D) shows the Gorda plate extends to ~ 500 km depth and the NA is the same shape as the Gorda plate, but offset to the east and slightly deeper. Further east, the high velocity flattens through the transition zone. Finally, the cross-section at the lowest latitude (Fig. 4.2E), south of the main components of the JdF/Farallon plate in the western U.S. shows the IA to be a significant high wave-speed feature in this region. The geometry of the IA is difficult to discern due to its proximity to the edge of the station coverage, but appears to be a nearly vertically oriented anomaly.

The IA and NA have previously been interpreted as lithospheric drips [Boyd et al., 2004; Frassetto et al., 2011; Jones et al., 1994; West et al., 2009; Zandt et al., 2004]. Lithospheric drips are proposed to form when relatively dense continental lithosphere becomes unstable and flows downward into the asthenosphere [Göğüş and Pysklywec, 2008]. This interpretation requires that the volume of observed high velocity material be sourced from an equal volume of lithosphere. To assess this constraint, we calculate the volume of observed high velocity material in the upper mantle and compare this volume with two scenarios of lithospheric removal. The first scenario posits that a 10 km thick layer of lower lithosphere was removed, representing only partial lithosphere removal. This scenario requires the lithosphere from beneath the entire Western U.S. to contribute to the drips (Fig. 4.3A). Alternatively, we consider removal of the entire mantle lithosphere column from the Moho to the lithosphere-

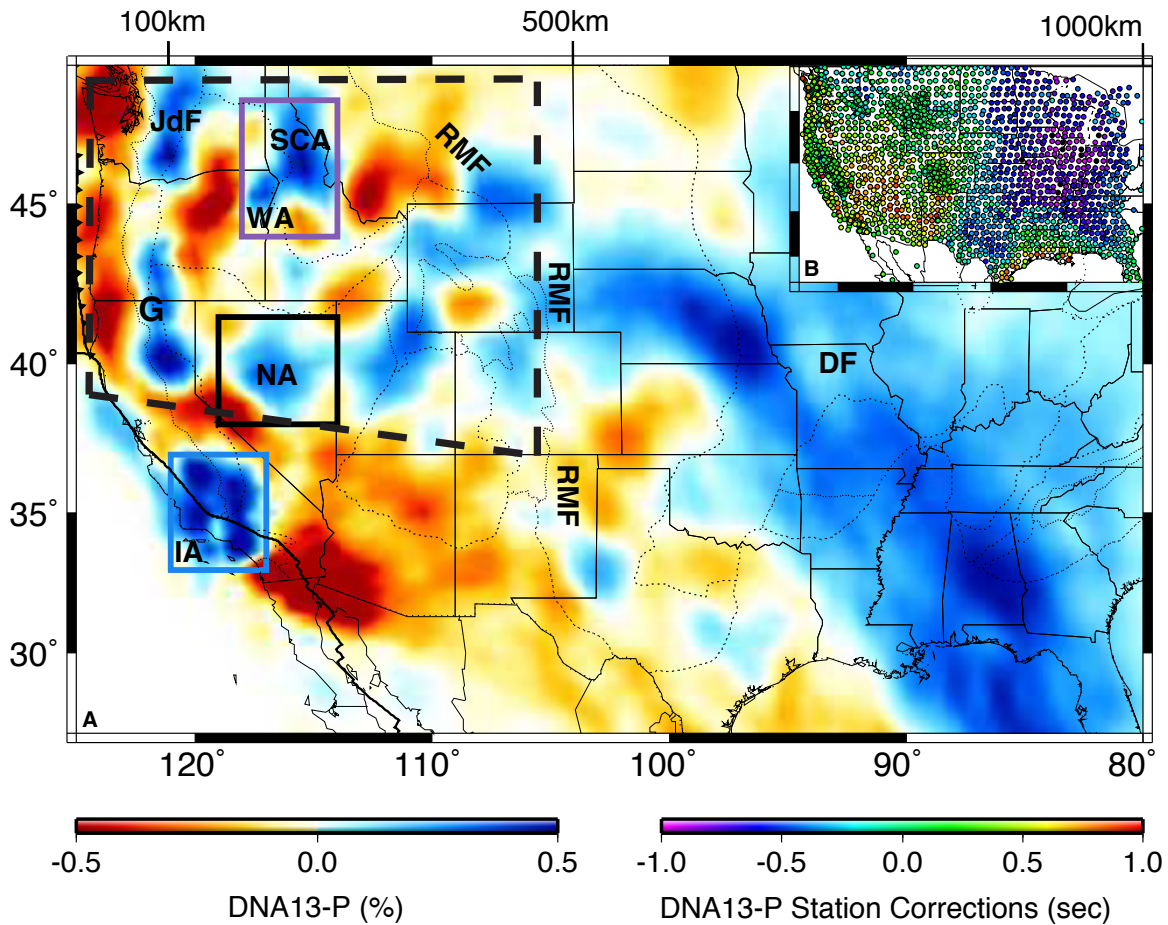


Figure 4.1: (A) Map projection of an east-dipping plane along the top trace of the Farallon plate. Color scale gives relative compressional wave-speed as determined in the DNA13-P model (left color-bar). Purple, black, and blue boxes respectively outline the Siletzia Curtain Anomaly and Wallowa Anomaly, Nevada Anomaly, and Isabella Anomaly. The scale across the top edge of the map displays the depth of the tomography slice. Dotted lines mark the US physiographic boundaries [Fenneman and Johnson, 1946]. Dashed outline displays the area considered in the calculation of expected western U.S. slab. (B) Inset map displays the station data used in the inversion and are color-coded according to station correction terms of DNA13-P (right color-bar), which represent the shallow unresolvable structure. Annotated abbreviations are given for the Juan de Fuca plate (JdF), Gorda plate (G), Isabella Anomaly (IA), Siletzia Curtain Anomaly (SCA), Wallowa Anomaly (WA), Nevada Anomaly (NA), Rocky Mountain Front (RMF), and Deep Farallon (DF).

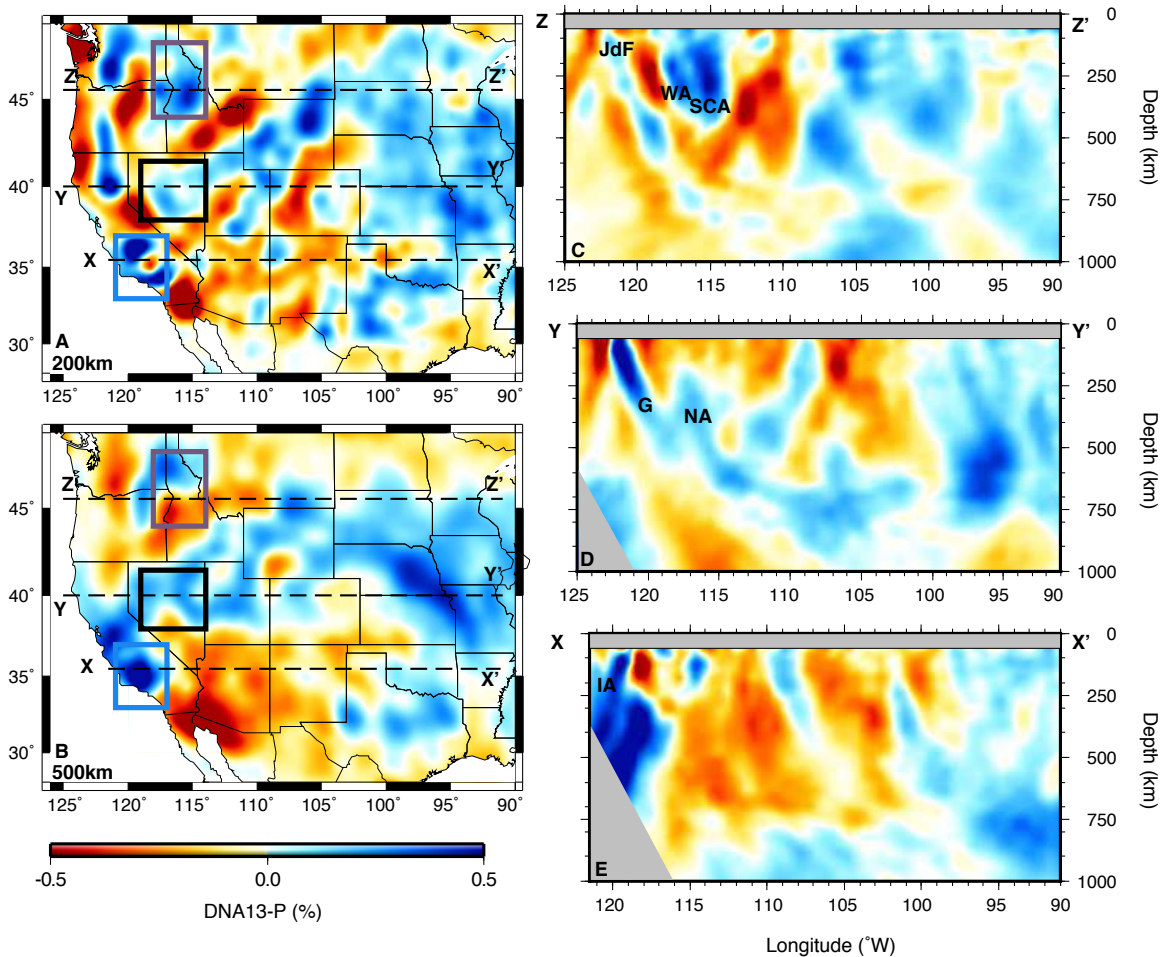


Figure 4.2: Maps at (A) 200km and (B) 500km depth of the DNA13-P tomographic model. Purple, black, and blue boxes designate the region of the Siletzia Curtain Anomaly (SCA) and Wallowa Anomaly (WA), Nevada Anomaly (NA), and Isabella Anomaly (IA). (C, D, and E) Cross-sections along constant latitude as indicated on maps A, B. Regions in grey mask the upper 60 km where body wave tomography lacks resolution and the low-resolution areas at the western edge of the model with low crossing ray coverage. Additional annotations on the cross-sections include the Juan de Fuca plate (JdF) and Gorda plate (G).

asthenosphere boundary. The average western U.S. crustal thickness is ~ 35 km [Levander and Miller, 2012] and the average lithospheric thickness is ~ 85 km [Levander and Miller, 2012]. Accordingly, we define this layer to be 50 km thick. The required source areas for each drip (Fig. 4.3B) do not overlap significantly in this scenario, but the still intact 60-80 km thick lithosphere observed in these large regions [Levander and Miller, 2012] makes this scenario improbable.

We also consider the volumetric constraints of a simplified subduction scenario. Assuming a 100 km thick layer of subducted lithosphere from the present JdF trench to the present upper limit of intact Farallon plate (Fig. 4.1), we expect $\sim 2.4 \times 10^8$ km³ of high velocity oceanic lithosphere beneath the western U.S. In DNA13-P, in the same region, we observe $\sim 1.9 \times 10^8$ km³ of high wave-speed material. Thus we observe 80% of the expected Farallon lithosphere beneath the western US. The missing $\sim 0.5 \times 10^8$ km³ of high velocity material may be due to (1) our overestimation of the amount of source material as North America is moving westward and the actual length of subducted slab is less than we estimate; (2) some slab has been lost/destroyed in the fragmentation process; or (3) uncertainties in the estimates. Still, these volume estimates are remarkably consistent, supporting the hypothesis that the high velocity anomalies are fragments of the Farallon slab.

4.3 Discussion

Tomographic evidence shows the SCA, NA, WA, and IA to be similar to the JdF plate in size and shape (Fig. 4.2). They are located in a region where the expectedly continuous Farallon slab is missing, and occupy a volume difficult to generate from delamination of the continental lithosphere. This is based on an assessment of the isotropic velocity structure. Analysis of topography, shear-wave splitting, and Ps receiver functions provide additional independent evidence for the origin of these features.

The removal of continental lithosphere by dripping has a pronounced effect on the overlying topography [Göğüş and Pysklywec, 2008]. Models predict an initial down warping of 0.5-1 km as the lithosphere drags down the crust, followed by a significant reversal as the material releases and results in ~ 1 km uplift at the center and 0.5 km depressions on the sides. In subduction zones, a similar topographic profile is generated where a volcanic arc forms and basins on either side of the arc compensate the crustal load. Comparing topographic profiles for the WA, SCA, NA, and IA to three profiles from the Cascadia subduction zone (Fig. 4.4), the SCA and the NA show relatively flat topography, but the IA profile is similar to the central and northern Cascadia profiles. The IA and Cascadia profiles have a larger eastern uplift, a central basin region, and uplift west of the basin. If the fully detached NA were a drip, a marked uplift should exist over the center of the drip. Instead, it is flat.

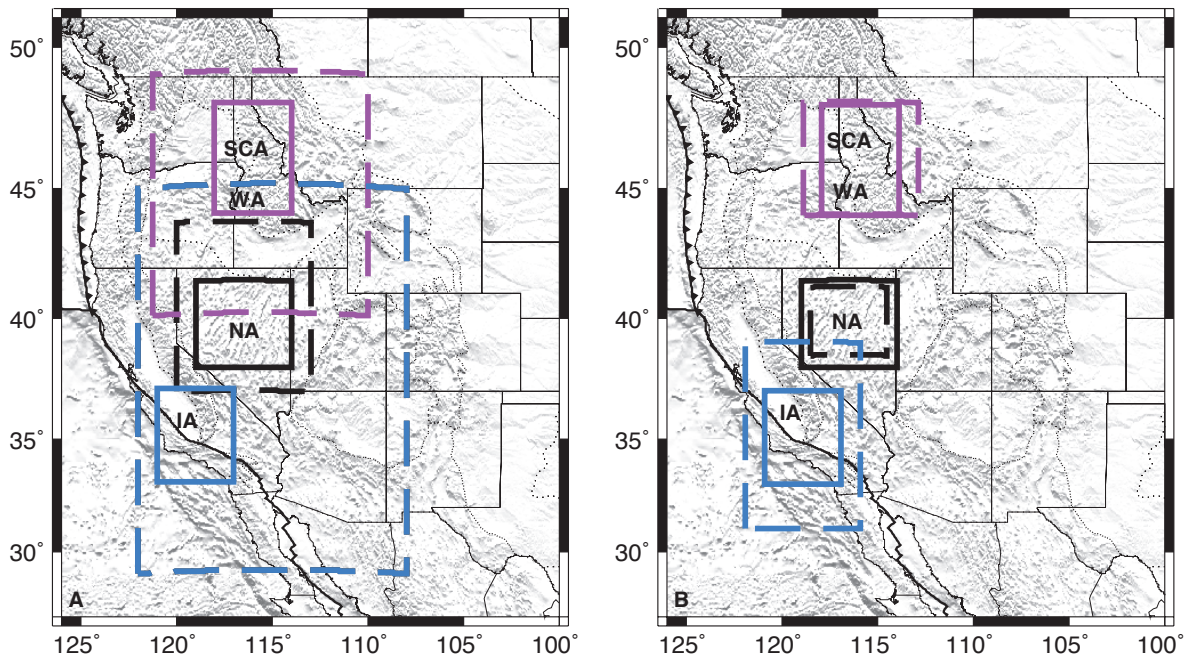


Figure 4.3: Comparisons of the area of the high velocity anomalies (solid) with potential source areas (dashed). (A) 10 km thick slab of lithosphere removal scenario. (B) 50 km thick slab of lithosphere removal scenario. Both maps display shaded topography and dotted lines representing the physiographic boundaries [Fenneman and Johnson, 1946].

No evidence of down warping of the crust above the SCA appears as would be expected for a drip that has yet to detach. The topography profile for the IA is identical to that of a subduction zone. Therefore, the topographic signal provides no substantial evidence supporting lithospheric dripping.

Shear-wave splitting analysis is proposed to support the drip hypothesis of the NA [West et al., 2009]. Shear-wave splitting results provide an estimate of mantle flow fabric [Silver, 1996]. A compilation of western U.S. observations of shear-wave splitting parameters [Wüstefeld et al., 2009] (Fig. 4.5) depicts a toroidal pattern around the NA with exceptionally low values in the center and a circular pattern around the high velocity body [West et al., 2009]. This is argued to represent downward flow from a convective downwelling [West et al., 2009]. However, there are at least two alternative explanations. Firstly, if the NA is a slab fragment, the negative buoyancy associated with a mostly subducted slab fragment is also a convective downwelling and would produce the same flow pattern as a lithospheric drip. Secondly, when depth-dependent anisotropy and a broader regional view is taken into account, this flow pattern is consistent with plate motion related lithosphere-asthenosphere coupling at depths shallower than 150 km and channeling of deep flow from the East Pacific Rise constrained by the southern edge of the JdF slab and western edge of the North American craton [Yuan and Romanowicz, 2010]. These two sources of anisotropy effectively cancel when integrated from the core-mantle boundary to the surface resulting in the observed low splitting times [Yuan and Romanowicz, 2010]. Western U.S. splitting patterns are further complicated by observations of little to no deflection of the fast axis splitting direction through the JdF, WA, IA, or SCA. The trench perpendicular splits through the JdF have been argued to indicate flow through a slab hole [Eakin et al., 2010] or alignment due to slab rollback [Faccenna et al., 2010]. This suggests that while typical subduction zones exhibit trench parallel splitting parameters [Long and Silver, 2008], more complex observations are possible when observed in a larger context. Again, little evidence supports the interpretation of lithospheric drips based on shear-wave splitting.

One of the more anomalous observations of the IA is a Moho hole, characterized by a small-amplitude, V-shaped signal in the Ps receiver functions [Frassetto et al., 2011; Zandt et al., 2004]. It has been proposed that the low amplitude is caused by a small velocity contrast between the crust and asthenospheric mantle after the lithospheric mantle is removed [Frassetto et al., 2011], and the lower crust being dragged to a greater depth than the surrounding crust causes the V-shaped signal. This would put the effective Moho over such a small temperature gradient [Frassetto et al., 2011] that it would not be recovered with standard P receiver functions. Additionally, similar weak phase conversions are observed in the wedge between a slab and continental lithosphere where subducted water causes serpentinization and mantle shear velocities to be reduced significantly to levels similar to those of lower crustal rock [Bostock et al., 2002; Christensen, 1966]. The V-shaped Moho would also be formed by the conversions off a remnant slab. Remnant slabs attached to the base of the

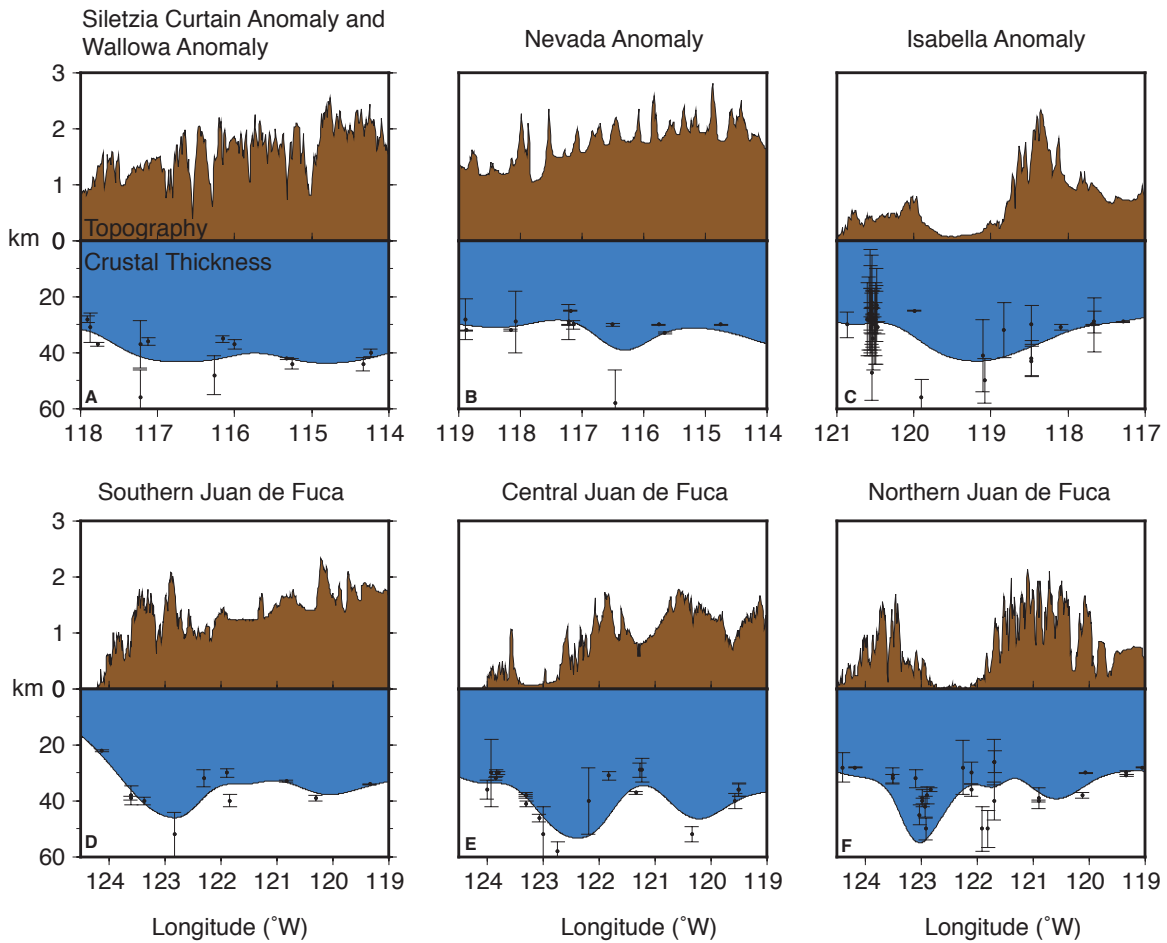


Figure 4.4: Topography and crustal thickness profiles across the (A) Wallowa Anomaly and Siletzia Curtain Anomaly, (B) Nevada Anomaly, (C) Isabella Anomaly, and three sections of the Juan de Fuca plate (D-F). Black points and error bars in the crustal thickness depict control points and error estimates of the crustal thickness from the Earthscope Automated Receiver Survey (EARS) experiment [Crotwell and Owens, 2005; Trabant et al., 2012]. Panels (A-C) are at the same latitude as shown in Fig 4.2(C-E).

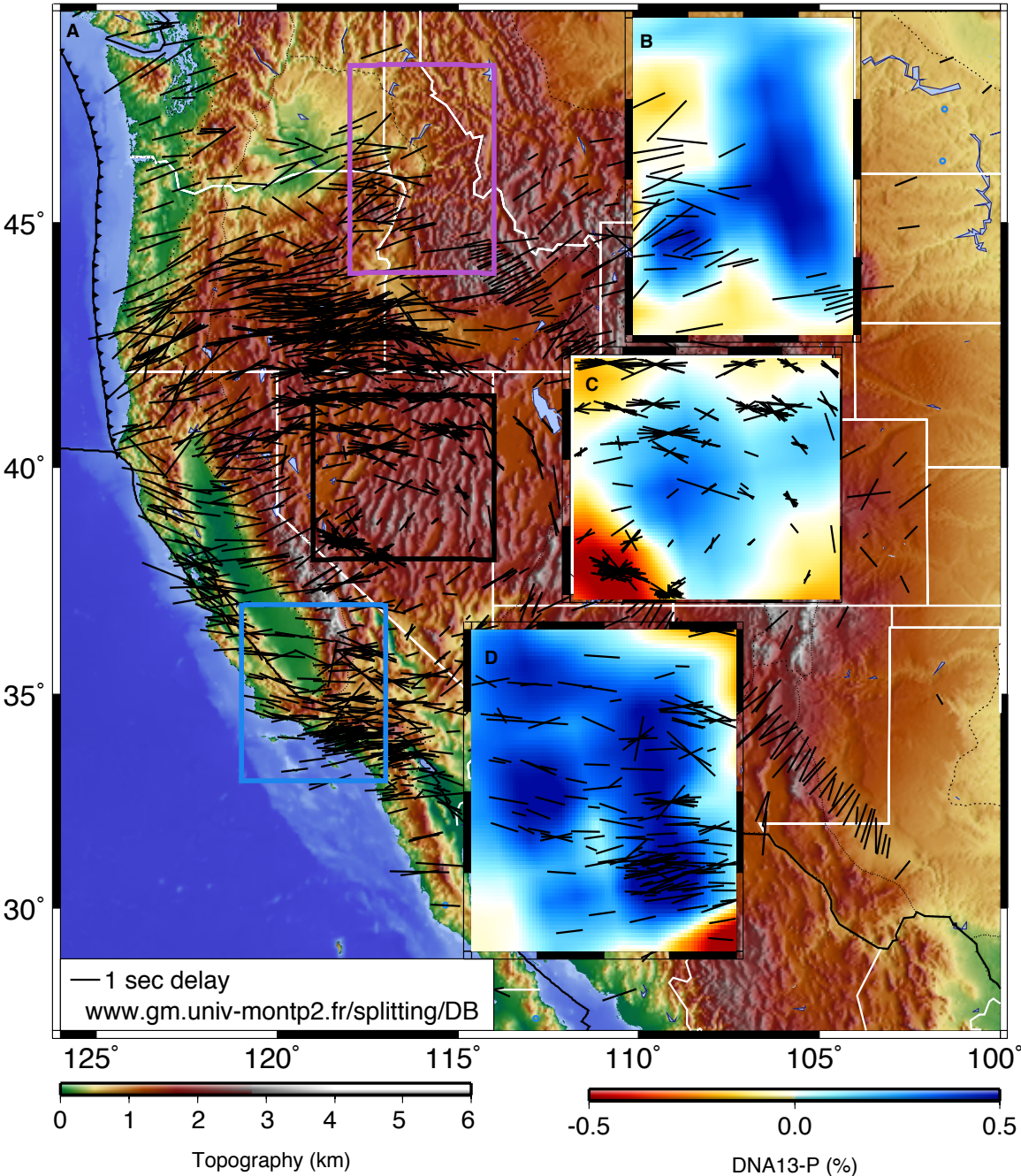


Figure 4.5: (A) Shear-wave splitting compilation for the western U.S. [Wüstefeld et al., 2009] superimposed on topography. Black sticks indicate the fast axis direction and relative splitting time. Inset maps depict the regions of interest at a larger scale and show the splitting parameters and wave-speed structure at 300 km depth for the (B) SCA and WA, (C) NA, and (D) IA.

continental lithosphere dip gently away from the trench and the Moho is observed through receiver functions until the serpentinized zone causes the Moho conversions to become too weak. Therefore the receiver function results for the IA [Frassetto et al., 2011; Zandt et al., 2004] do not conclusively point to a drip, and are consistent with a shallow remnant slab [Bostock et al., 2002].

The above arguments indicate that the evidence for large-scale mantle dripping in all of these locations is inconclusive. Rather, the long history of subduction provides a viable source for the high wave-speed material, and the observations used to argue for dripping lithosphere are consistent with stalled pieces of remnant slab. Furthermore, significant portions of the subducted Farallon slab are missing and the volume of the observed shallow high velocity bodies largely account for the missing slab.

The slab fragmentation hypothesis has two important criticisms [Frassetto et al., 2011]. First, the IA and SCA must have translated with North America since 20 Ma and 60 Ma, respectively. Geodynamic models considering a buoyant, young slab, such as the Siletzia plate or the Monterey plate, are able to reproduce this translation from negligible gravitational forces relative to viscous drag forces [Pikser et al., 2012]. Secondly, xenolith data indicate a ~ 140 km thick continental lithosphere in the Sierras at ~ 8 -10 Ma [Ducea and Saleeby, 1998]. This observation is suspect for two reasons. First, observations of the modern lithospheric thickness show an average of 76.1 ± 18.7 km for the western U.S. and significantly thinner lithosphere in the Cascades and Sierra Nevada [Levander and Miller, 2012]. If lithospheric thickness had been greater in the Miocene, we would either expect other locations of thickened lithosphere in the western U.S., which have not detached, or more drips in a variety of locations. Neither is observed. Additionally, if this thickened root was intact during the Mesozoic, the geometry of the Farallon slab would be unrealistically complex to account for the Miocene magmatic quiescence and uplift of the Rocky Mountains during the Sevier Orogeny. The slab would have had to dip steeply near the trench, flatten below 150 km depth, and then shallow to less than 100 km depth and flatten down-dip.

We next explore possible scenarios that generate the observed wave-speed structure through subduction-based processes (Fig. 4.6). The proposed accretion of the SCA considers a microplate within the Farallon system to have detached from the Farallon when trench rollback initiated [Schmandt and Humphreys, 2011]. The presence of the WA [Darold and Humphreys, 2013], west of the SCA, may represent the trenchward portion of the Siletzia microplate. The NA may have formed when the Yellowstone plume broke through a weak part of the Farallon plate [Obrebski et al., 2010]. Alternatively, the break in the slab may have occurred without the plume from the viscosity contrast with the asthenosphere [Liu and Stegman, 2011, 2012]. The IA represents the deeper portion of the Monterey Microplate [Wang et al., 2013]. The presence of an attached microplate may help explain the creeping section of the San Andreas Fault [Pikser et al., 2012] by providing a source of fluids.

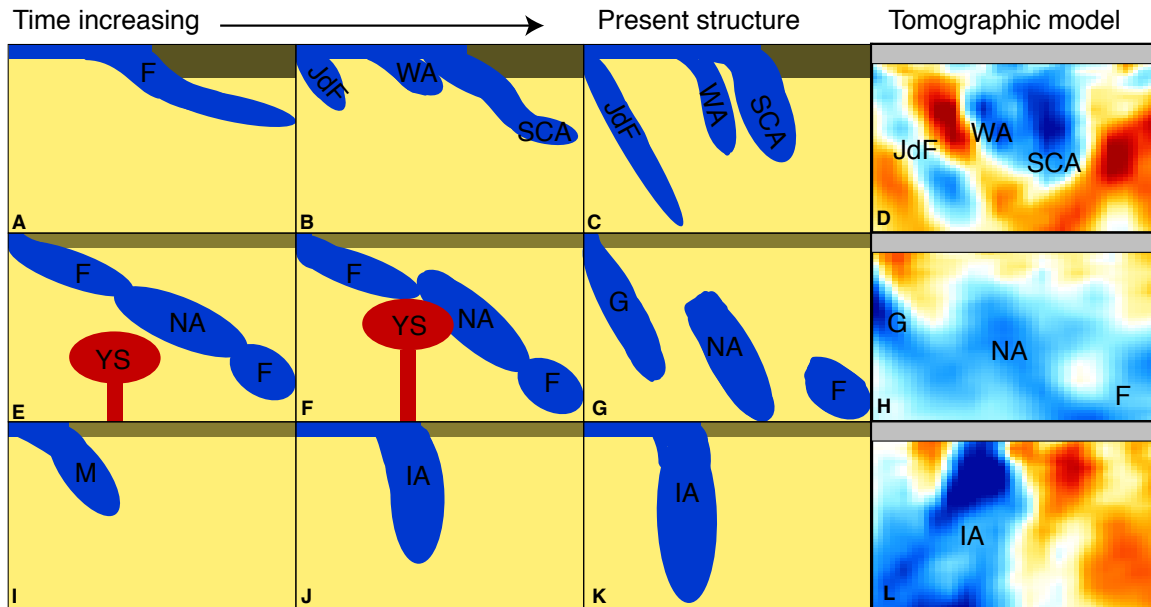


Figure 4.6: Proposed reconstructions for the Siletzia Curtain Anomaly and Wallowa Anomaly (A-D), Nevada Anomaly (E-H), and Isabella Anomaly (I-L). Time progresses from left to right in each column with the final image showing the wave-speed anomaly structure extracted from DNA13-P as seen in Fig. 4.2. Note the red plume in panels E-F, which has translated north out of plane by the final image. Annotated abbreviations are given for the Farallon plate (F), Juan de Fuca plate (JdF), Wallowa Anomaly (WA), Siletzia Curtain Anomaly (SCA), Nevada Anomaly (NA), Yellowstone Plume (YS), Gorda plate (G), Monterey Microplate (M), and the Isabella Anomaly (IA).

4.4 Conclusions

Ambiguous evidence prevents determining if high wave-speed anomalies in the upper mantle are drips or remnant slabs when considered as individual geologic objects. When the western U.S. is considered as a whole, the theory that continental lithosphere drips are the source for all of these anomalies becomes unreasonable. Simultaneously, an oceanic lithosphere origin, such as the western Farallon slab, provides a viable source of high wave-speed material. Indeed, if the observed high-wave-speed anomalies are not interpreted as remnant slabs, we must identify where the Farallon slab went. Relatively young oceanic lithosphere has less rheological contrast to typical asthenosphere and is more readily able to founder in

the upper mantle, or even accrete to the lower continental lithosphere, rather than sink into the lower mantle [Pikser et al., 2012]. With time, the eastward progression of the Farallon ridge toward North America provided younger and younger oceanic lithosphere into the subduction zone [Atwater and Stock, 1998]. This would also explain why a more continuous Farallon slab is imaged beneath the eastern U.S. as it was older at the time of subduction and survived the subduction process intact.

A recent study of lower mantle structure has argued that what we interpret as eastern Farallon plate is actually composed of three much older plates (Angayucham, Mezcalera, and Southern Farallon) and the actual Northern Farallon is nearly vertically sinking under the western U.S. Cordillera [Sigloch and Mihalynuk, 2013]. The apparent absence of subducted oceanic lithosphere between the present JdF subduction and the eastern Farallon plate is used as a supporting argument for this hypothesis. However, the fragments of high-velocity material in the upper mantle that we interpret as slabs stitch together, linking present subduction to the eastern high-velocity anomaly [Pavlis, 2011]. We therefore prefer the interpretation that the eastern Farallon anomaly is in fact a continuation of present day JdF subduction.

Our hypothesis further implies that we are potentially imaging the process of continental lithosphere creation, as remnant slabs may remain attached to the overriding continental lithosphere. While the evidence does not show conclusively that these features must all be slabs, the slab hypothesis is consistent with the observations and follows naturally from the 150+ Ma subduction history. Therefore, analysis of high velocity anomalies in the western U.S., and elsewhere, must start with the hypothesis of an oceanic lithosphere origin before a drip hypothesis should be invoked.

This chapter has been submitted for publication in Science magazine.

4.5 Chapter Acknowledgements

The DNA13-P tomographic model is available at dna.berkeley.edu. All figures were made with Generic Mapping Tools (GMT). We thank IRIS and Earthscope for the USArray dataset. We also thank UC Berkeley undergraduate Jenny Taing for helping measure arrival times. We thank Shu-Huei Hung for continued use of software and the rest of the UC Berkeley regional imaging group (Cheng Cheng, William Hawley, Qingkai Kong, and Robert Martin-Short) for continuing discussion on early versions of this manuscript. We thank Don Forsyth for early copies of references [Pikser et al., 2012; Wang et al., 2013]. We thank Barbara Romanowicz, Debi Kilb, and Judy Gaukel for helpful reviews of the manuscript. Author Porritt made the DNA13-P model and both authors contributed to the text of the manuscript.

Chapter 5

Conclusions

The Farallon plate system, as imaged today, is highly disjointed. The eastern end of the Farallon slab is imaged shallower than may be expected for a plate which formed ~ 100 Ma. The western end is highly heterogeneous with patches of high velocity material representing break-up of the slab within the asthenosphere. This dissertation has explored these structures through seismic imaging using traveltimes of teleseismic earthquakes and ambient noise. The combination of body waves and surface waves increases the overall resolution of the model and therefore produces a more complete picture of the subduction process.

The PNW10-S velocity model contains a low velocity anomaly between the Gorda and Juan de Fuca plates. This anomaly is coincident with segmentation in tremor, topography, volcanic geochemistry, and accreted terrane boundaries. This segmentation reflects the on-going separation of the Gorda and Juan de Fuca plates. This process is being reinforced by mantle upwellings around the edges of the slab (Fig. 5.1). Eventually, the Gorda plate will fully separate from the Juan de Fuca plate and, based on the relative strength of the bouyancy forces versus the viscous drag forces, the Gorda will either accrete to North America or subduct beneath the continent. Based on the young age of the Gorda slab, its likely a significant portion of the plate will founder in a similar manner as the Monterey microplate.

The DNA13 model provides a view of the deeper eastern Farallon slab. The inclusion of Rayleigh wave phase velocities in the SV-Joint model allows resolution of the separation of the thick craton root from the subducting slab. This model shows a shallowed portion of the slab under the Ozark Plateau (Fig 5.2). This shallow portion of the slab is likely due to a subducted oceanic plateau. This thickened plateau would have less negative bouyancy than typical oceanic lithosphere and thus may be unable to penetrate the mantle transition zone due to the high viscosity. This may also help account for the flat slab period as the less negatively bouyant slab would resist vertical sinking.

Shallow high velocity anomalies in the western U.S. pose a quandry. Models of plate motion forces suggest the negative bouyancy force of oceanic slabs prohibits slabs to become stagnant [Burkett and Gurnis, 2013]. However, other models, which pose a negligible density

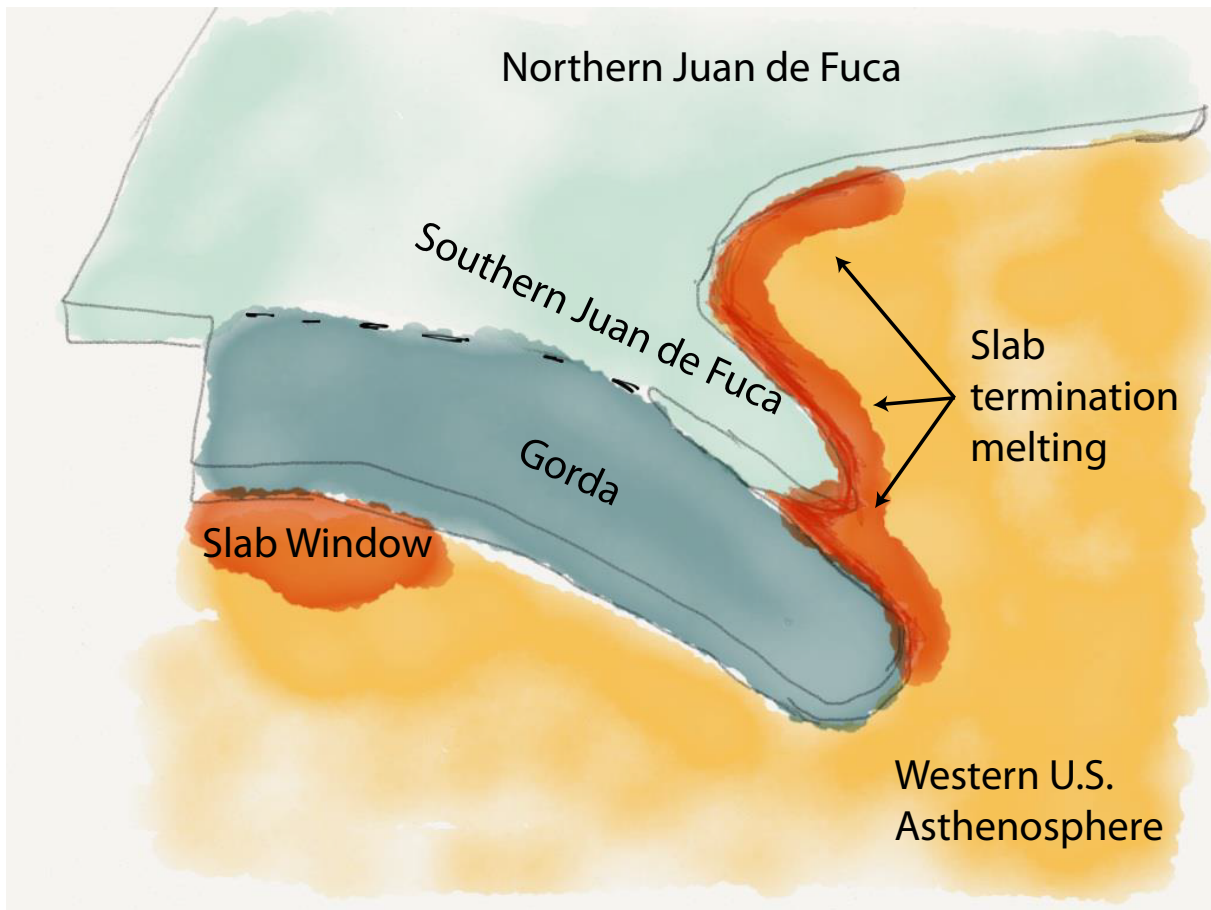


Figure 5.1: Interpretation of PNW subduction. The three slab segments are shown in blue. A tear-fault separates the Gorda and southern Juan de Fuca plates. Melting occurs at the edges of the slab as evidenced by the low velocity anomalies in the PNW10-S model.

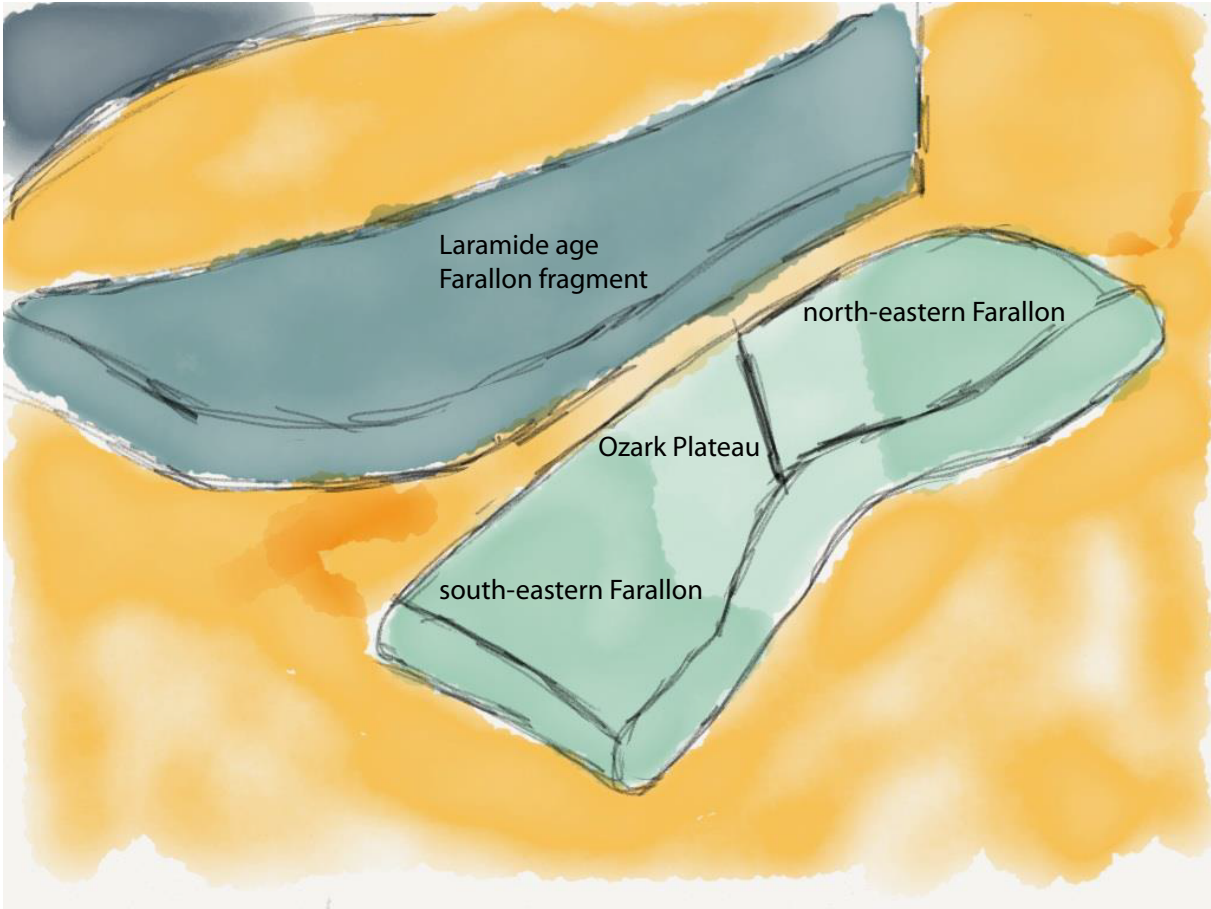


Figure 5.2: Illustration of the Farallon plate under the eastern U.S. The plate shallows under the Ozark Plateau and the Laramide age Farallon plate is separated from the deeper plate.

contrast, show that along strike translation of stalled slabs is possible indefinitely for young slabs [Pikser et al., 2012]. The seismologic evidence is largely ambiguous between lithospheric instabilities and stalled slabs, and therefore the best evidence to distinguish them is integration into the broader tectonic context. The fragmented subduction of the Farallon plate system, as documented above, provides an excellent source for all these anomalies. The western U.S. Farallon fragments are illustrated in figure 5.3 to provide an overall picture of this piece-meal subduction.

The debate of slabs versus drips is fundamental to the understanding of Plate Tectonics. If lithospheric dripping is as prominent as it is argued to be in the western U.S., then it becomes possible to destroy cratonic lithosphere in the span of a few million years. However, the slab fragmentation hypothesis requires mechanisms to break apart and support the strong and dense oceanic plates. Ultimately, the similarity of the observations of the features results in an unsatisfying conundrum. Therefore, this dissertation has argued the null hypothesis when viewing these anomalies should be a subduction origin as it is more consistent with the overall plate tectonic cycle.

The Farallon plate represents a marked departure from the simplistic model of an infinitely viscous sheet. While heterogeneities such as tear faults and oceanic plateaus may be rare, their occurrence is non-negligible in the case of the Farallon plate which has been subducting for over 150 million years. In this dissertation I've provided evidence of such slab complexities and argued that they are responsible for slab fragmentation leading to the many remnant slab anomalies seen today. On a regional scale, this implies the Gorda/Juan de Fuca system will continue to break up as it subducts and pieces of it will accrete to North America. Looking more broadly, this suggests complex subduction histories are quite common and may provide the necessary mechanisms for creation of continental lithosphere.

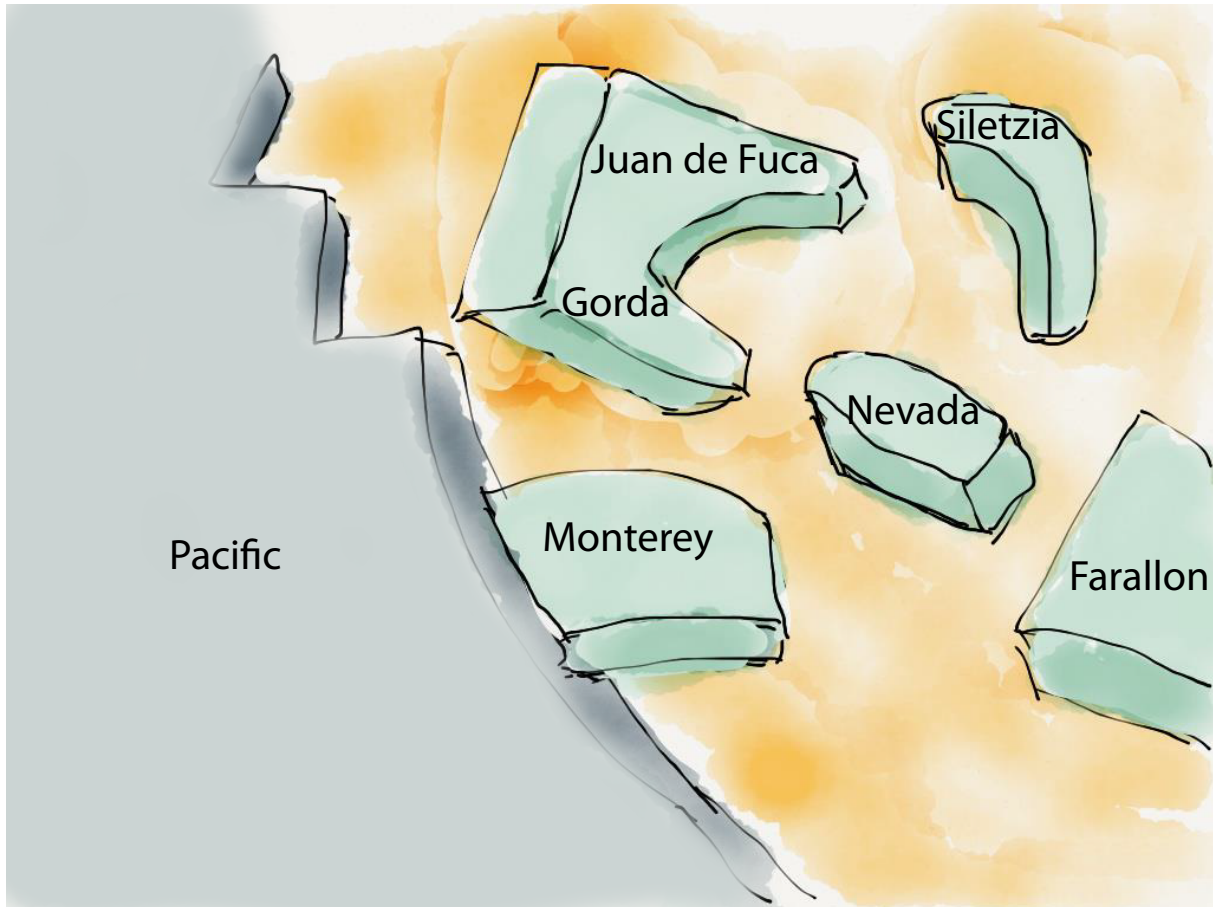


Figure 5.3: Interpretation of plate fragments in the western U.S. Blue bodies represent the pieces of the Farallon plate at various stages of subduction.

Bibliography

- Abt, D. L., Fischer, K. M., French, S. W., Ford, H. A., Yuan, H., and Romanowicz, B. (2010). North american lithospheric discontinuity structure imaged by ps and sp receiver functions. *Journal of Geophysical Research: Solid Earth (1978–2012)*, 115(B9).
- Atwater, T. and Stock, J. (1998). Pacific-north america plate tectonics of the neogene southwestern united states: an update. *International Geology Review*, 40(5):375–402.
- Audet, P., Bostock, M. G., Boyarko, D. C., Brudzinski, M. R., and Allen, R. M. (2010). Slab morphology in the cascadia fore arc and its relation to episodic tremor and slip. *Journal of Geophysical Research: Solid Earth (1978–2012)*, 115(B4).
- Babcock, R., Burmester, R., Engebretson, D., Warnock, A., and Clark, K. (1992). A rifted margin origin for the crescent basalts and related rocks in the northern coast range volcanic province, washington and british columbia. *Journal of Geophysical Research: Solid Earth (1978–2012)*, 97(B5):6799–6821.
- Bailey, I. W., Miller, M. S., Liu, K., and Levander, A. (2012). Vs and density structure beneath the colorado plateau constrained by gravity anomalies and joint inversions of receiver function and phase velocity data. *Journal of Geophysical Research: Solid Earth (1978–2012)*, 117(B2).
- Barmin, M., Ritzwoller, M., and Levshin, A. (2001). A fast and reliable method for surface wave tomography. In *Monitoring the Comprehensive Nuclear-Test-Ban Treaty: Surface Waves*, pages 1351–1375. Springer.
- Bates, R. G., Beck, M. E., and Burmester, R. F. (1981). Tectonic rotations in the cascade range of southern washington. *Geology*, 9(4):184–189.
- Becker, T. (2012). On recent seismic tomography for the western united states. *Geochemistry, Geophysics, Geosystems*, 13(1).
- Bensen, G., Ritzwoller, M., Barmin, M., Levshin, A., Lin, F., Moschetti, M., Shapiro, N., and Yang, Y. (2007). Processing seismic ambient noise data to obtain reliable broad-band surface wave dispersion measurements. *Geophysical Journal International*, 169(3):1239–1260.
- Bostock, M., Hyndman, R., Rondenay, S., and Peacock, S. (2002). An inverted continental moho and serpentinization of the forearc mantle. *Nature*, 417(6888):536–538.

- Bostock, M., Rondenay, S., and Shragge, J. (2001). Multiparameter two-dimensional inversion of scattered teleseismic body waves 1. theory for oblique incidence. *Journal of Geophysical Research: Solid Earth (1978–2012)*, 106(B12):30771–30782.
- Boyarko, D. C. and Brudzinski, M. R. (2010). Spatial and temporal patterns of nonvolcanic tremor along the southern cascadia subduction zone. *Journal of Geophysical Research*, 115.
- Boyd, O., Jones, C., and Sheehan, A. F. (2004). Foundering lithosphere imaged beneath the southern sierra nevada, california, usa. *Science*, 305:660–662.
- Braile, L. W., Hinze, W. J., Keller, G. R., Lidiak, E. G., and Sexton, J. L. (1986). Tectonic development of the new madrid rift complex, mississippi embayment, north america. *Tectonophysics*, 131(1):1–21.
- Brandon, M. T., Roden-Tice, M. K., and Garver, J. I. (1998). Late cenozoic exhumation of the cascadia accretionary wedge in the olympic mountains, northwest washington state. *Geological Society of America Bulletin*, 110(8):985–1009.
- Bromirski, P. D., Duennebieer, F. K., and Stephen, R. A. (2005). Mid-ocean microseisms. *Geochemistry Geophysics Geosystems*, 6(4):Q04009.
- Brown, J. R., Beroza, G. C., Ide, S., Ohta, K., Shelly, D. R., Schwartz, S. Y., Rabbel, W., Thorwart, M., and Kao, H. (2009). Deep low-frequency earthquakes in tremor localize to the plate interface in multiple subduction zones. *Geophysical Research Letters*, 36(19):L19306.
- Brudzinski, M. R. and Allen, R. M. (2007). Segmentation in episodic tremor and slip all along cascadia. *Geology*, 35(10):907–910.
- Burdick, S., Li, C., Martynov, V., Cox, T., Eakins, J., Mulder, T., Astiz, L., Vernon, F. L., Pavlis, G. L., and van der Hilst, R. D. (2008). Upper mantle heterogeneity beneath north america from travel time tomography with global and usarray transportable array data. *Seismological Research Letters*, 79(3):384–392.
- Burdick, S., van der Hilst, R. D., Vernon, F. L., Martynov, V., Cox, T., Eakins, J., Karasu, G. H., Tylell, J., Astiz, L., and Pavlis, G. L. (2012). Model update march 2011: Upper mantle heterogeneity beneath north america from travelttime tomography with global and usarray transportable array data. *Seismological Research Letters*, 83(1):23–28.
- Burkett, E. and Gurnis, M. (2013). Stalled slab dynamics. *Lithosphere*, 5(1):92–97.
- Calkins, J. A., Abers, G. A., Ekström, G., Creager, K. C., and Rondenay, S. (2011). Shallow structure of the cascadia subduction zone beneath western washington from spectral

- ambient noise correlation. *Journal of Geophysical Research: Solid Earth (1978–2012)*, 116(B7).
- Cessaro, R. K. (1994). Sources of primary and secondary microseisms. *Bulletin of the Seismological Society of America*, 84(1):142–148.
- Christensen, N. I. (1966). Elasticity of ultrabasic rocks. *Journal of Geophysical Research*, 71(24):5921–5931.
- Chulick, G. S. and Mooney, W. D. (2002). Seismic structure of the crust and uppermost mantle of north america and adjacent oceanic basins: a synthesis. *Bulletin of the Seismological Society of America*, 92(6):2478–2492.
- Crotwell, H. P. and Owens, T. J. (2005). Automated receiver function processing. *Seismological Research Letters*, 76(6):702–709.
- Crotwell, H. P., Owens, T. J., and Ritsema, J. (1999). The taup toolkit: Flexible seismic travel-time and ray-path utilities. *Seismological Research Letters*, 70(2):154–160.
- Currie, C. A., Cassidy, J. F., Hyndman, R. D., and Bostock, M. G. (2004). Shear wave anisotropy beneath the cascadia subduction zone and western north american craton. *Geophysical Journal International*, 157(1):341–353.
- Darold, A. and Humphreys, E. (2013). Upper mantle seismic structure beneath the pacific northwest: A plume-triggered delamination origin for the columbia river flood basalt eruptions. *Earth and Planetary Science Letters*, 365:232–242.
- Dreger, D. S. and Romanowicz, B. A. (1995). *Source characteristics of events in the San Francisco Bay region*. University of California.
- Ducea, M. N. and Saleeby, J. B. (1998). The age and origin of a thick mafic–ultramafic keel from beneath the sierra nevada batholith. *Contributions to Mineralogy and Petrology*, 133(1-2):169–185.
- Dziewonski, A., Bloch, S., and Landisman, M. (1969). A technique for the analysis of transient seismic signals. *Bulletin of the Seismological Society of America*, 59(1):427–444.
- Dziewonski, A. M. and Anderson, D. L. (1981). Preliminary reference earth model. *Physics of the earth and planetary interiors*, 25(4):297–356.
- Eakin, C. M., Obrebski, M., Allen, R. M., Boyarko, D. C., Brudzinski, M. R., and Porritt, R. (2010). Seismic anisotropy beneath cascadia and the mendocino triple junction: Interaction of the subducting slab with mantle flow. *Earth and Planetary Science Letters*, 297(3):627–632.

- Faccenna, C., Becker, T. W., Lallemand, S., Lagabriele, Y., Funicello, F., and Piromallo, C. (2010). Subduction-triggered magmatic pulses: A new class of plumes? *Earth and Planetary Science Letters*, 299(1):54–68.
- Fenneman, N. M. and Johnson, D. W. (1946). Physiographic boundaries of the conterminous united states.
- Foster, D. A., Mueller, P. A., Mogk, D. W., Wooden, J. L., and Vogl, J. J. (2006). Proterozoic evolution of the western margin of the wyoming craton: Implications for the tectonic and magmatic evolution of the northern rocky mountains. *Canadian Journal of Earth Sciences*, 43(10):1601–1619.
- Frassetto, A. M., Zandt, G., Gilbert, H., Owens, T. J., and Jones, C. H. (2011). Structure of the sierra nevada from receiver functions and implications for lithospheric foundering. *Geosphere*, 7(4):898–921.
- Ghosh, A., Vidale, J. E., Sweet, J. R., Creager, K. C., and Wech, A. G. (2009). Tremor patches in cascadia revealed by seismic array analysis. *Geophysical Research Letters*, 36(17).
- Göğüş, O. H. and Pysklywec, R. N. (2008). Near-surface diagnostics of dripping or delaminating lithosphere. *Journal of Geophysical Research: Solid Earth (1978–2012)*, 113(B11).
- Goldfinger, C., Nelson, C. H., Morey, A., Johnson, J. E., Gutiérrez-Pastor, J., Eriksson, A., Karabanov, E., Patton, J., Gràcia, E., Enkin, R., et al. (2012). *Turbidite event history: Methods and implications for Holocene paleoseismicity of the Cascadia subduction zone*. US Department of the Interior, US Geological Survey.
- Grand, S. P. (1994). Mantle shear structure beneath the americas and surrounding oceans. *Journal of Geophysical Research: Solid Earth (1978–2012)*, 99(B6):11591–11621.
- Harden, D. (1998). *California Geology: Englewood Cliffs*. Prentice Hall.
- Harmon, N., Gerstoft, P., Rychert, C. A., Abers, G. A., Salas de La Cruz, M., and Fischer, K. M. (2008). Phase velocities from seismic noise using beamforming and cross correlation in costa rica and nicaragua. *Geophysical Research Letters*, 35(19).
- Huang, Y.-C., Yao, H., Huang, B.-S., van der Hilst, R. D., Wen, K.-L., Huang, W.-G., and Chen, C.-H. (2010). Phase velocity variation at periods of 0.5–3 seconds in the taipei basin of taiwan from correlation of ambient seismic noise. *Bulletin of the Seismological Society of America*, 100(5A):2250–2263.
- Humphreys, E., Hessler, E., Dueker, K., Farmer, G. L., Erslev, E., and Atwater, T. (2003). How laramide-age hydration of north american lithosphere by the farallon slab controlled

- subsequent activity in the western united states. *International Geology Review*, 45(7):575–595.
- Humphreys, E. D. and Coblenz, D. D. (2007). North american dynamics and western us tectonics. *Reviews of Geophysics*, 45(3).
- Hung, S.-H., Dahlen, F., and Nolet, G. (2000). Fréchet kernels for finite-frequency traveltimes—ii. examples. *Geophysical Journal International*, 141(1):175–203.
- Ingebritsen, S. E. and Mariner, R. (2010). Hydrothermal heat discharge in the cascade range, northwestern united states. *Journal of Volcanology and Geothermal Research*, 196(3):208–218.
- James, D. E., Fouch, M. J., Carlson, R. W., and Roth, J. B. (2011). Slab fragmentation, edge flow and the origin of the yellowstone hotspot track. *Earth and Planetary Science Letters*, 311(1):124–135.
- Jones, C. H., Kanamori, H., and Roecker, S. W. (1994). Missing roots and mantle “drips”: Regional pn and teleseismic arrival times in the southern sierra nevada and vicinity, california. *Journal of geophysical research*, 99(B3):4567–4601.
- Kao, H., Shan, S.-J., Dragert, H., Rogers, G., Cassidy, J. F., and Ramachandran, K. (2005). A wide depth distribution of seismic tremors along the northern cascadia margin. *Nature*, 436(7052):841–844.
- Karlstrom, L., Dufek, J., and Manga, M. (2009). Organization of volcanic plumbing through magmatic lensing by magma chambers and volcanic loads. *Journal of Geophysical Research: Solid Earth (1978–2012)*, 114(B10).
- Keller, G. R. and Stephenson, R. A. (2007). The southern oklahoma and dnier-donets aulacogens: A comparative analysis. *Geological Society of America Memoirs*, 200:127–143.
- Kennett, B. and Engdahl, E. (1991). Traveltimes for global earthquake location and phase identification. *Geophysical Journal International*, 105(2):429–465.
- Köhler, A., Weidle, C., and Maupin, V. (2011). Directionality analysis and rayleigh wave tomography of ambient seismic noise in southern norway. *Geophysical Journal International*, 184(1):287–300.
- Kumar, P., Kind, R., Yuan, X., and Mechie, J. (2012). Usarray receiver function images of the lithosphere-asthenosphere boundary. *Seismological Research Letters*, 83(3):486–491.

- Kustowski, B., Ekström, G., and Dziewoński, A. (2008). Anisotropic shear-wave velocity structure of the earth's mantle: A global model. *Journal of Geophysical Research: Solid Earth (1978–2012)*, 113(B6).
- Landès, M., Hubans, F., Shapiro, N. M., Paul, A., and Campillo, M. (2010). Origin of deep ocean microseisms by using teleseismic body waves. *Journal of Geophysical Research: Solid Earth (1978–2012)*, 115(B5).
- Lay, T., Berger, J., Buland, R., Butler, R., Ekstrom, G., Hutt, B., and Romanowicz, B. (2002). Global seismic network design goals update 2002. *IRIS, August*, 26.
- Lebedev, S. and Van Der Hilst, R. D. (2008). Global upper-mantle tomography with the automated multimode inversion of surface and s-wave forms. *Geophysical Journal International*, 173(2):505–518.
- Lee, C. (2006). Geochemical/petrologic constraints on the origin of cratonic mantle. *GEO-PHYSICAL MONOGRAPH-AMERICAN GEOPHYSICAL UNION*, 164:89.
- Lecic, V., Cottaar, S., Dziewonski, A., and Romanowicz, B. (2012). Cluster analysis of global lower mantle tomography: A new class of structure and implications for chemical heterogeneity. *Earth and Planetary Science Letters*, 357:68–77.
- Levander, A. and Miller, M. S. (2012). Evolutionary aspects of lithosphere discontinuity structure in the western us. *Geochemistry, Geophysics, Geosystems*, 13(7).
- Levander, A., Niu, F., Miller, M., Zhai, Y., and Liu, K. (2007). Usarray receiver function images of the lithosphere in the western us. In *AGU Fall Meeting Abstracts*, volume 1, page 01.
- Levshin, A. L., Yanovskaia, T., Lander, A. V., Bukchin, B. G., Barmin, M. P., and Ramikova, L. (1989). Surface waves in vertically inhomogeneous media. *Surface waves in a laterally inhomogeneous earth*, pages 131–182.
- Li, C., van der Hilst, R. D., Engdahl, E. R., and Burdick, S. (2008). A new global model for p wave speed variations in earth's mantle. *Geochemistry, Geophysics, Geosystems*, 9(5).
- Liang, C. and Langston, C. A. (2008). Ambient seismic noise tomography and structure of eastern north america. *Journal of Geophysical Research*, 113(B3):B03309.
- Lin, F.-C., Moschetti, M. P., and Ritzwoller, M. H. (2008). Surface wave tomography of the western united states from ambient seismic noise: Rayleigh and love wave phase velocity maps. *Geophysical Journal International*, 173(1):281–298.

- Liu, K., Levander, A., Niu, F., and Miller, M. S. (2011). Imaging crustal and upper mantle structure beneath the colorado plateau using finite frequency rayleigh wave tomography. *Geochemistry, Geophysics, Geosystems*, 12(7).
- Liu, K., Levander, A., Zhai, Y., Porritt, R. W., and Allen, R. M. (2012). Asthenospheric flow and lithospheric evolution near the mendocino triple junction. *Earth and Planetary Science Letters*, 323:60–71.
- Liu, L., Gurnis, M., Seton, M., Saleeby, J., Müller, R. D., and Jackson, J. M. (2010). The role of oceanic plateau subduction in the laramide orogeny. *Nature Geoscience*, 3(5):353–357.
- Liu, L. and Stegman, D. R. (2011). Segmentation of the farallon slab. *Earth and Planetary Science Letters*, 311(1):1–10.
- Liu, L. and Stegman, D. R. (2012). Origin of columbia river flood basalt controlled by propagating rupture of the farallon slab. *Nature*, 482(7385):386–389.
- Long, M. D. and Silver, P. G. (2008). The subduction zone flow field from seismic anisotropy: A global view. *Science*, 319(5861):315–318.
- McCaffrey, R., Long, M. D., Goldfinger, C., Zwick, P. C., Nabelek, J. L., Johnson, C. K., and Smith, C. (2000). Rotation and plate locking at the southern cascadia subduction zone. *Geophysical Research Letters*, 27(19):3117–3120.
- McCaffrey, R., Qamar, A. I., King, R. W., Wells, R., Khazaradze, G., Williams, C. A., Stevens, C. W., Vollick, J. J., and Zwick, P. C. (2007). Fault locking, block rotation and crustal deformation in the pacific northwest. *Geophysical Journal International*, 169(3):1315–1340.
- McCrory, P. A., Blair, J. L., Oppenheimer, D. H., and Walter, S. R. (2004). *Depth to the Juan de Fuca slab beneath the Cascadia subduction margin: A 3-D model for sorting earthquakes*. US Department of the Interior, US Geological Survey.
- McNeill, L. C., Goldfinger, C., Kulm, L. D., and Yeats, R. S. (2000). Tectonics of the neogene cascadia forearc basin: Investigations of a deformed late miocene unconformity. *Geological Society of America Bulletin*, 112(8):1209–1224.
- Moschetti, M., Ritzwoller, M., and Shapiro, N. (2007). Surface wave tomography of the western united states from ambient seismic noise: Rayleigh wave group velocity maps. *Geochemistry, Geophysics, Geosystems*, 8(8).
- Mosher, S. (1998). Tectonic evolution of the southern laurentian grenville orogenic belt. *Geological Society of America Bulletin*, 110(11):1357–1375.
- NAMAD (2011). North american magnetic anomaly database.

- Nettles, M. and Dziewoński, A. M. (2008). Radially anisotropic shear velocity structure of the upper mantle globally and beneath north america. *Journal of Geophysical Research: Solid Earth (1978–2012)*, 113(B2).
- Obrebski, M., Allen, R. M., Pollitz, F., and Hung, S.-H. (2011). Lithosphere–asthenosphere interaction beneath the western united states from the joint inversion of body-wave travel-times and surface-wave phase velocities. *Geophysical Journal International*, 185(2):1003–1021.
- Obrebski, M., Allen, R. M., Xue, M., and Hung, S.-H. (2010). Slab-plume interaction beneath the pacific northwest. *Geophysical Research Letters*, 37(14).
- Panning, M., Lekić, V., and Romanowicz, B. (2010). Importance of crustal corrections in the development of a new global model of radial anisotropy. *Journal of Geophysical Research: Solid Earth (1978–2012)*, 115(B12).
- Panning, M. and Romanowicz, B. (2006). A three-dimensional radially anisotropic model of shear velocity in the whole mantle. *Geophysical Journal International*, 167(1):361–379.
- Pavlis, G. L. (2011). Three-dimensional wavefield imaging of data from the usarray: New constraints on the geometry of the farallon slab. *Geosphere*, 7(3):785–801.
- Peterson, J. (1993). Observations and modeling of seismic background noise.
- Pikser, J. E., Forsyth, D. W., and Hirth, G. (2012). Along-strike translation of a fossil slab. *Earth and Planetary Science Letters*, 331:315–321.
- Pollitz, F. and Snoke, J. A. (2010). Rayleigh-wave phase-velocity maps and three-dimensional shear velocity structure of the western us from local non-plane surface wave tomography. *Geophysical Journal International*, 180(3):1153–1169.
- Pollitz, F. F. (2008). Observations and interpretation of fundamental mode rayleigh wavefields recorded by the transportable array (usarray). *Journal of Geophysical Research: Solid Earth (1978–2012)*, 113(B10).
- Porritt, R. W., Allen, R. M., Boyarko, D. C., and Brudzinski, M. R. (2011). Investigation of cascadia segmentation with ambient noise tomography. *Earth and Planetary Science Letters*, 309(1):67–76.
- Rhie, J. and Romanowicz, B. (2004). Excitation of earth’s continuous free oscillations by atmosphere–ocean–seafloor coupling. *Nature*, 431(7008):552–556.
- Rogers, G. and Dragert, H. (2003). Episodic tremor and slip on the cascadia subduction zone: The chatter of silent slip. *Science*, 300(5627):1942–1943.

- Romanowicz, B., Cara, M., Fel, J. F., and Rouland, D. (1984). Geoscope: A french initiative in long-period three-component global seismic networks. *Eos, Transactions American Geophysical Union*, 65(42):753–753.
- Roscoe, S. and Card, K. (1993). The reappearance of the huronian in wyoming: rifting and drifting of ancient continents. *Canadian Journal of Earth Sciences*, 30(12):2475–2480.
- Ross, G. M. (2002). Evolution of precambrian continental lithosphere in western canada: results from lithoprobe studies in alberta and beyond. *Canadian Journal of Earth Sciences*, 39(3):413–437.
- Saar, M. and Manga, M. (2004). Depth dependence of permeability in the oregon cascades inferred from hydrogeologic, thermal, seismic, and magmatic modeling constraints. *Journal of Geophysical Research: Solid Earth (1978–2012)*, 109(B4).
- Saygin, E. and Kennett, B. L. (2010). Ambient seismic noise tomography of australian continent. *Tectonophysics*, 481(1):116–125.
- Schellart, W., Stegman, D., Farrington, R., Freeman, J., and Moresi, L. (2010). Cenozoic tectonics of western north america controlled by evolving width of farallon slab. *Science*, 329(5989):316–319.
- Schmandt, B. and Humphreys, E. (2010). Complex subduction and small-scale convection revealed by body-wave tomography of the western united states upper mantle. *Earth and Planetary Science Letters*, 297(3):435–445.
- Schmandt, B. and Humphreys, E. (2011). Seismically imaged relict slab from the 55 ma siletzia accretion to the northwest united states. *Geology*, 39(2):175–178.
- Schmidt, M. E., Grunder, A. L., and Rowe, M. C. (2008). Segmentation of the cascade arc as indicated by sr and nd isotopic variation among diverse primitive basalts. *Earth and Planetary Science Letters*, 266(1):166–181.
- Shapiro, N. and Ritzwoller, M. (2002). Monte-carlo inversion for a global shear-velocity model of the crust and upper mantle. *Geophysical Journal International*, 151(1):88–105.
- Shelly, D. R., Beroza, G. C., and Ide, S. (2007). Non-volcanic tremor and low-frequency earthquake swarms. *Nature*, 446(7133):305–307.
- Sigloch, K. (2011). Mantle provinces under north america from multifrequency p wave tomography. *Geochemistry, Geophysics, Geosystems*, 12(2).
- Sigloch, K. and Mihalynuk, M. G. (2013). Intra-oceanic subduction shaped the assembly of cordilleran north america. *Nature*, 496(7443):50–56.

- Silver, P. G. (1996). Seismic anisotropy beneath the continents: Probing the depths of geology. *Annual Review of Earth and Planetary Sciences*, 24:385–432.
- Simmons, N. A., Forte, A. M., Boschi, L., and Grand, S. P. (2010). Gypsum: A joint tomographic model of mantle density and seismic wave speeds. *Journal of Geophysical Research: Solid Earth (1978–2012)*, 115(B12).
- Snavely, P. D., Wagner, H. C., and Lander, D. L. (1980). Interpretation of the cenozoic geologic history, central oregon continental margin: Cross-section summary. *Geological Society of America Bulletin*, 91(3):143–146.
- Soreghan, G. S., Keller, G. R., Gilbert, M. C., Chase, C. G., and Sweet, D. E. (2012). Load-induced subsidence of the ancestral rocky mountains recorded by preservation of permian landscapes. *Geosphere*, 8(3):654–668.
- Trabant, C., Hutko, A. R., Bahavar, M., Karstens, R., Ahern, T., and Aster, R. (2012). Data products at the iris dmc: Stepping stones for research and other applications. *Seismological Research Letters*, 83(5):846–854.
- Trehu, A., Asudeh, I., Brocher, T., Luetgert, J., Mooney, W., Nabelek, J., and Nakamura, Y. (1994). Crustal architecture of the cascadia forearc. *Science*, pages 237–237.
- Tromp, J., Komatitsch, D., Hjörleifsdóttir, V., Liu, Q., Zhu, H., Peter, D., Bozdog, E., McRitchie, D., Friberg, P., Trabant, C., et al. (2010). Near real-time simulations of global cmt earthquakes. *Geophysical Journal International*, 183(1):381–389.
- van der Hilst, R. D., Widiyantoro, S., and Engdahl, E. R. (1997). Evidence for deep mantle circulation from global tomography. *Nature*, 386:578–584.
- van der Lee, S. and Nolet, G. (1997). Seismic image of the subducted trailing fragments of the farallon plate. *Nature*, 386(6622):266–269.
- Van Schmus, W. and Hinze, W. (1985). The midcontinent rift system. *Annual Review of Earth and Planetary Sciences*, 13:345.
- VanDecar, J. and Crosson, R. (1990). Determination of teleseismic relative phase arrival times using multi-channel cross-correlation and least squares. *Bulletin of the Seismological Society of America*, 80(1):150–169.
- Waite, G. P., Smith, R. B., and Allen, R. M. (2006). Vp and vs structure of the yellowstone hot spot from teleseismic tomography: Evidence for an upper mantle plume. *Journal of Geophysical Research: Solid Earth (1978–2012)*, 111(B4).

- Wang, Y., Forsyth, D. W., Rau, C. J., Carriero, N., Schmandt, B., Gaherty, J. B., and Savage, B. (2013). Fossil slabs attached to unsubducted fragments of the farallon plate. *Proceedings of the National Academy of Sciences*, 110(14):5342–5346.
- Wessel, P. and Smith, W. H. (1998). New, improved version of generic mapping tools released. *Eos, Transactions American Geophysical Union*, 79(47):579–579.
- West, J. D., Fouch, M. J., Roth, J. B., and Elkins-Tanton, L. T. (2009). Vertical mantle flow associated with a lithospheric drip beneath the great basin. *Nature Geoscience*, 2(6):439–444.
- Whitmeyer, S. J. and Karlstrom, K. E. (2007). Tectonic model for the proterozoic growth of north america. *Geosphere*, 3(4):220–259.
- Wüstefeld, A., Bokelmann, G., Barruol, G., and Montagner, J.-P. (2009). Identifying global seismic anisotropy patterns by correlating shear-wave splitting and surface-wave data. *Physics of the Earth and Planetary Interiors*, 176(3):198–212.
- Xue, M. and Allen, R. M. (2010). Mantle structure beneath the western united states and its implications for convection processes. *Journal of Geophysical Research: Solid Earth (1978–2012)*, 115(B7).
- Yang, Y., Ritzwoller, M., Lin, F., Moschetti, M., and Shapiro, N. (2008). The structure of the crust and uppermost mantle beneath the western us revealed by ambient noise and earthquake tomography. *J. Geophys. Res*, 113:B1231.
- Yang, Y., Ritzwoller, M. H., Levshin, A. L., and Shapiro, N. M. (2007). Ambient noise rayleigh wave tomography across europe. *Geophysical Journal International*, 168(1):259–274.
- You, S.-H., Gung, Y., Chiao, L.-Y., Chen, Y.-N., Lin, C.-H., Liang, W.-T., and Chen, Y.-L. (2010). Multiscale ambient noise tomography of short-period rayleigh waves across northern taiwan. *Bulletin of the Seismological Society of America*, 100(6):3165–3173.
- Yuan, H. and Dueker, K. (2005). Upper mantle tomographic vp and vs images of the rocky mountains in wyoming, colorado, and new mexico: Evidence for a thick heterogeneous chemical lithosphere. *Geophys. Monogr*, 154:329–345.
- Yuan, H. and Romanowicz, B. (2010). Depth dependent azimuthal anisotropy in the western us upper mantle. *Earth and Planetary Science Letters*, 300(3):385–394.
- Yuan, H., Romanowicz, B., Fischer, K. M., and Abt, D. (2011). 3-d shear wave radially and azimuthally anisotropic velocity model of the north american upper mantle. *Geophysical Journal International*, 184(3):1237–1260.

- Zandt, G., Gilbert, H., Owens, T. J., Ducea, M., Saleeby, J., and Jones, C. H. (2004). Active foundering of a continental arc root beneath the southern sierra nevada in california. *Nature*, 431(7004):41–46.